INFORMATION TO USERS

This dissertation was produced from a microfilm copy of the original document. While the most advanced technological means to photograph and reproduce this document have been used, the quality is heavily dependent upon the quality of the original submitted.

The following explanation of techniques is provided to help you understand markings or patterns which may appear on this reproduction.

1. The sign or "target" for pages apparently lacking from the document photographed is "Missing Page(s)". If it was possible to obtain the missing page(s) or section, they are spliced into the film along with adjacent pages. This may have necessitated cutting thru an image and duplicating adjacent pages to insure you complete continuity.

2. When an image on the film is obliterated with a large round black mark, it is an indication that the photographer suspected that the copy may have moved during exposure and thus cause a blurred image. You will find a good image of the page in the adjacent frame.

3. When a map, drawing or chart, etc., was part of the material being photographed the photographer followed a definite method in "sectioning" the material. It is customary to begin photoing at the upper left hand corner of a large sheet and to continue photoing from left to right in equal sections with a small overlap. If necessary, sectioning is continued again — beginning below the first row and continuing on until complete.

4. The majority of users indicate that the textual content is of greatest value, however, a somewhat higher quality reproduction could be made from "photographs" if essential to the understanding of the dissertation. Silver prints of "photographs" may be ordered at additional charge by writing the Order Department, giving the catalog number, title, author and specific pages you wish reproduced.

University Microfilms

300 North Zeeb Road
Ann Arbor, Michigan 48106

A Xerox Education Company

73-6865

LEUNG, Kang-Ming, 1939-
SOME RESONANT PROCESSES IN NONLINEAR OPTICS.

The University of Michigan, Ph.D., 1972
Physics, optics

University Microfilms, A XEROX Company, Ann Arbor, Michigan

THIS DISSERTATION HAS BEEN MICROFILMED EXACTLY AS RECEIVED.

SOME RESONANT PROCESSES IN NONLINEAR OPTICS

by

Kang-Ming Leung

A dissertation submitted in partial fulfillment
of the requirements for the degree of
Doctor of Philosophy
(Physics)
in The University of Michigan
1972

Doctoral Committee:

Associate Professor John F. Ward, Chairman
Professor David R. Bach
Professor Peter A. Franken
Professor Karl T. Hecht
Professor Richard H. Sands

PLEASE NOTE:

Some pages may have

indistinct print.

Filmed as received.

University Microfilms, A Xerox Education Company

"And God said, Let there be light:
and there was light." (Genesis 1:3)

ACKNOWLEDGEMENTS

It is a pleasure to express my gratitude and respect to Professor John F. Ward for suggesting this research problem and giving so generously his time and knowledge for its progress. During the entire course of this work, his physical intuition, intelligent guidance as well as criticisms have made significant contributions to my education.

I wish to thank the other members of my committee for their time and interest in my work. I am indebted to Dr. Brian J. Orr and Dr. Michael F. Koskinen for their valuable discussions.

My wife, Lillian, has prepared the final form of this manuscript; her encouragement and assistance are invaluable. Many thanks to Mr. Rudy Wolf of the Physics Student Shop for his contributions to my knowledge in machine work.

Finally, I also wish to acknowledge the financial support of this work furnished in part by the United States Atomic Energy Commission and in part by the United States Air Force Office of Scientific Research.

TABLE OF CONTENTS

		Page
ACKNOWLEDGEMENTS		iii
LIST OF TABLES		vi
LIST OF FIGURES		vii
CHAPTER 1.	INTRODUCTION	1
CHAPTER 2.	EXPERIMENTAL APPARATUS AND BASIC THIRD-HARMONIC EXPERIMENT	9
	2.1 Experimental Apparatus	9
	2.2 Observation of Third-Harmonic Generation in Cesium Vapor	17
CHAPTER 3.	THEORY AND EXPERIMENTS OF THIRD-HARMONIC GENERATION IN AN INHOMOGENEOUS MEDIUM	19
	3.1 The Propagation Problem	19
	3.2 The plane Wave Fundamental	25
	3.3 The Focused Fundamental	30
	3.4 Vibration Curves	39
	3.5 Comparison With Experiments	45

		Page
CHAPTER 4.	RESONANT THIRD-HARMONIC GENERATION IN CESIUM VAPOR	59
	4.1 Experiments of Resonant Third-Harmonic Generation and Correlated Two-Photon Absorption in Atomic Cesium Vapor	60
	4.2 Measurement of the Resonant Third-Harmonic Coefficient for Cesium	67
	4.3 Longitudinal Multimode Structure of the Laser Beam	72
	4.4 Theoretical Value of the Resonant Third-Harmonic Coefficient for Cesium	76
CHAPTER 5.	FOUR-PHOTON PARAMETRIC AMPLIFICATION IN CESIUM VAPOR	91
	5.1 Exponential Gain of the Signal Wave	92
	5.2 Experimental	96
	5.3 Theoretical Value of Gain Coefficient	102
CHAPTER 6.	SUMMARY AND CONCLUSIONS	109
APPENDIX 1.	QUANTUM MECHANICAL CALCULATION OF χ_{Cs}	113
REFERENCES		118

LIST OF TABLES

TABLE		Page
1.	Some Special Cases of I^{THG}	38
2.	List of Symbols	58
3.	Transition Probabilities of Cesium Atom with $9D_{3/2}$ as the Excited State	66
4.	Beating of Three Modes	84
5.	Summary of Third-Harmonic Coefficients	90
6.	Expected Signal Waves	97

LIST OF FIGURES

FIGURE		Page
1.	Cesium Energy Level Diagram	4
2.	Resonant Processes in Cesium	5
3.	Schematic Diagram of Experimental Apparatus	10
4.	Variation of Ruby Laser Wavelength with Temperature	11
5.	A Sketch of the Cesium Vapor Cell	14
6.	Cesium Vapor Cell	15
7.	Notation for Third-Harmonic Generation by a Lowest-order Gaussian Beam in an Inhomogeneous, Nonlinear Medium	32
8.	Vibration Curves for Third-Harmonic Generation by a Plane Wave Fundamental Beam	40
9.	Vibration Curves for Third-Harmonic Generation by a Focused Fundamental Beam in an Inhomogeneous Medium	42
10.	Vibration Curves of Optimizing Parameters ℓ and Ω at $\xi_0 = 0$	43
11.	Theoretical Prediction of Signal Dependence on Focal Position with respect to Cs Density ...	44

FIGURE Page

12. Cesium Density vs Cell Length 47

13. Number of Coherence Lengths vs Cesium Side Arm Temperature 48

14. Signal Dependence on Number of Coherence Lengths 50

15. Operational Ranges of Confocal Parameter for Cesium Experiments 51

16. Signal Dependence on Confocal Parameter 53

17. Signal Dependence on Focal Position with respect to Cesium Density Distribution 56

18. Typical Oscilloscope Traces 61

19. A Pair of Resonance Curves 63

20. Simultaneous Power Outputs of $P^{3\omega}$ and P^{ω_f} with respect to Fundamental Power P^{ω} Plotted on Log-Log Scales for 35 Shots in a Given Experimental Situation 65

21. Schematic Diagram for Comparison of Two Experimental Setup 70

22. Interferogram of Ruby Laser Taken with a Plane Fabry-Perot Etalon Having a Spacing of 25 mm 73

FIGURE Page

23. Schematics for Dependence of Linewidth and Mode Number of Our Ruby Laser on Ruby Output Frequency 74

24. Number of Modes vs Ruby Laser Output Frequency 75

25. Idealized Situation of Longitudinal Multimode Structure of the Ruby Laser 77

26. Doppler Averaging of χ_{Cs} for Single Mode Case 82

27. Model of Three Modes Case for Averaging Process 83

28. Results of Averaging on Doppler Width for Longitudinal Multimode Case 88

29. Simultaneous Measurement of Head-on Detector Signal and Sideways Detector Signal as a Function of Cesium Density and Fundamental Power 99

30. $\ell n\ V_s$ vs Cesium Density and Pump Intensity ... 101

31. Simulated Doppler Averaging of $\hat{\chi}$ for Four-Photon Parametric Amplification 105

CHAPTER 1

INTRODUCTION

Some interesting aspects of the interaction of light with matter may be described in terms of an array of dipole moments induced in the matter by the applied optical field. As long as the applied fields are much weaker than the binding field acting on the electron of the microscopic system, this polarization may be assumed to be linearly proportional to the applied field. However, in general, the polarization is nonlinearly related to the field and this will manifest itself whenever the applied fields are sufficiently strong (for example, many materials break down completely at optical fields of 10^7 volts per cm). Since the invention of the first laser in 1960 by T. H. Maiman, this nonlinearity has been demonstrated in many experiments making use of the intense optical field of the laser. The first such experiment was performed by P. A. Franken and coworkers[1] at the University of Michigan in 1961. They found that optical second harmonic of 6943 $\mathring{A}$ ruby laser light could be generated by focusing the laser beam in a quartz crystal. This harmonic is radiated by the induced polarization component quadratic in the applied optical electric field. As a result, an entirely new field of study, nonlinear optics, has bloomed since then.

A phenomenological description of nonlinear optics can start with a series expansion of the induced polarization

P in the matter due to the presence of the applied electric fields:

$$P_i = X_{ij}E_j + K'X_{ijk}E_jE_k + K''X_{ijkl}E_jE_kE_l + \ldots \quad (1.1)$$

where the K's are constants; X_{ij} is a second rank tensor representing the linear polarizability of the atom or molecule; X_{ijk} and X_{ijkl} denote respectively third and fourth rank tensor susceptibilities associated with second and third order nonlinear optical effects. Such effects as harmonic generation; multiphoton absorption and emission; three- and four- wave parametric interactions; stimulated light scattering (Raman, Brillouin, Rayleigh, Rayleigh wing); photon echoes, optical nutation and self-induced transparency; optical bleaching; and others (not to be mentioned here) are included in this field of nonlinear optics. A review on this subject may be found in reference 2.

Many fields of study in physics are often devoted to the resonant processes for their fundamental interest and importance. An investigation of resonant nonlinear optical effects, likewise, is of considerable fundamental interest and may also have practical engineering importance. Resonant processes such as single or two photon absorption and stimulated Raman scattering have already been studied in many materials[3]. They can best be studied in free atomic systems in a gaseous medium because the narrowness of the discrete energy levels provides dramatic resonant effects which

can be tuned through with a light source of limited tuning range. Moreover, such systems offer the best opportunity for comparison between theory and experiment. A gaseous system also allows smooth variation of the density which we have found convenient.

The present work is largely devoted to one such system: the cesium atom interacting with a ruby laser beam. It is noted that in cesium atom (refer to cesium energy level diagram of Figure 1), the $9D_{3/2}$ level lying 28828.90 cm^{-1} above the ground state is just equal to twice the ruby-photon energy 14414.45 cm^{-1} when the ruby rod is operated at a suitable temperature (near liquid nitrogen temperature). In addition, the parity of this state coincides with the parity of the ground state. This scheme provides dramatic resonant effects.

Three resonant processes in atomic cesium vapor have been studied in this work. We concentrate largely in the observation of third-harmonic generation with resonant enhancement in which linear absorption in either the fundamental or the third-harmonic is negligible. This resonant process is illustrated in Figure 2(a). Three fundamental photons are absorbed and one third-harmonic photon is emitted. The coincidence between the energy of the $9D_{3/2}$ level and that of two fundamental photons leads to a resonant enhancement of this process. At the same time, a second resonant process, two-photon absorption can be observed sideways since some of the population of $9D_{3/2}$ state

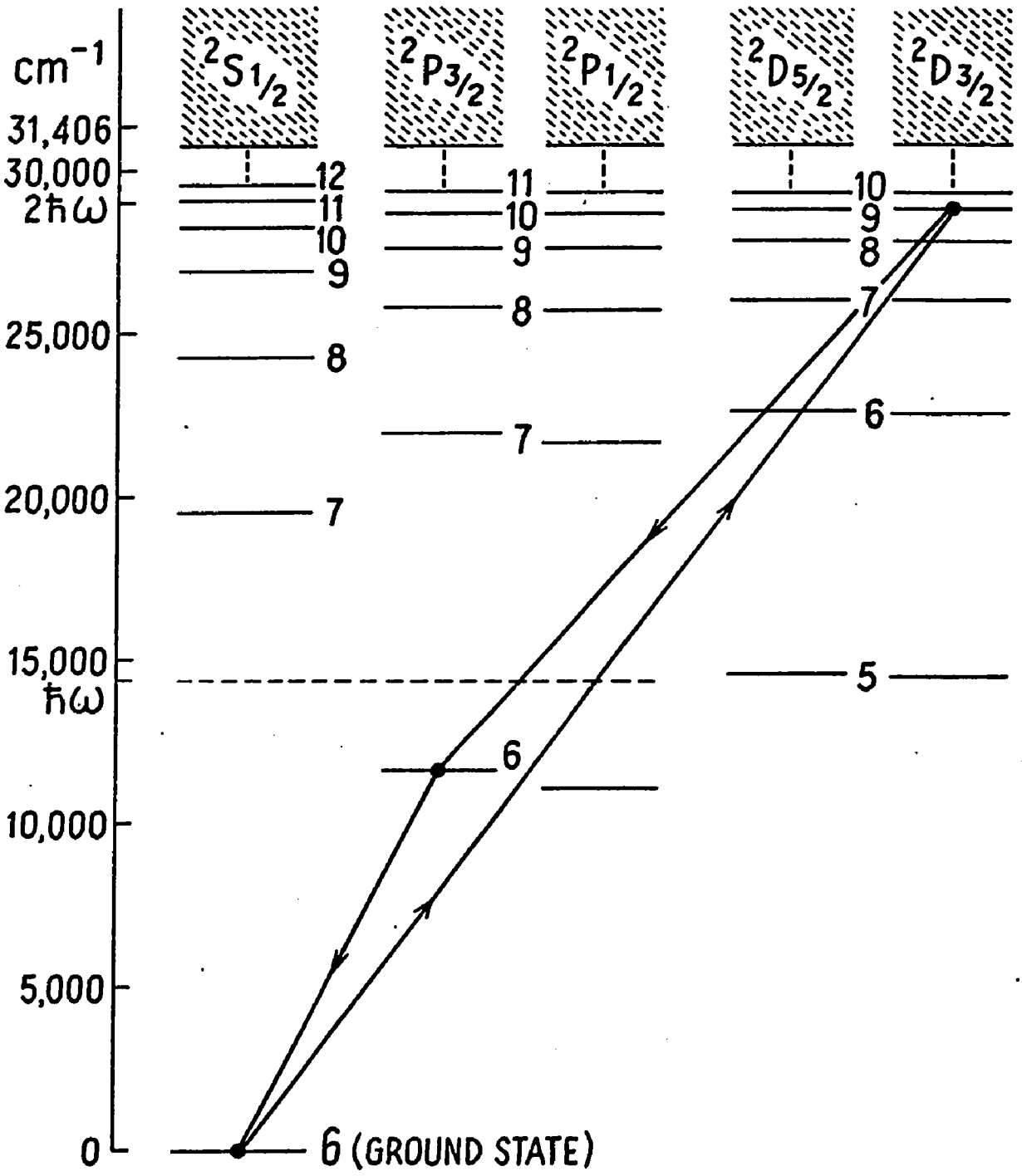


Figure 1. Cesium Energy Level Diagram

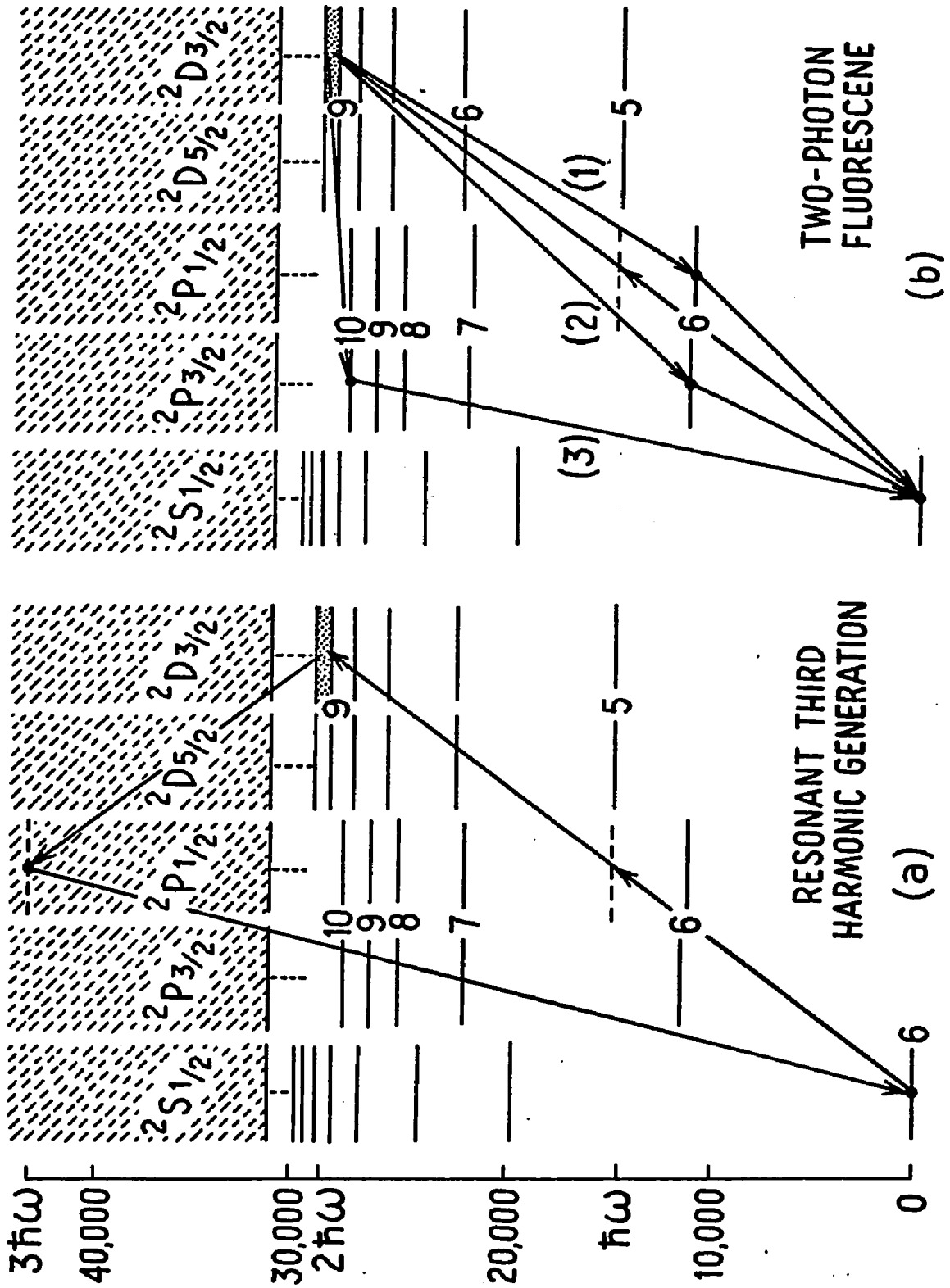


Figure 2. Resonant Processes in Cesium

must return to the ground state in two steps by means of fluorescent decay. We have observed two dominent fluorescent components in atomic cesium vapor, namely, radiation corresponding to spontaneous transitions $9D_{3/2} \rightarrow 6P_{1/2}$ (at 5666 Å) and $9D_{3/2} \rightarrow 6P_{3/2}$ (at 5847 Å) as indicated by (1) and (2) respectively in Figure 2(b). In fact, it is noted that in 1962, Abella[4] has observed optical two-photon absorption in this system by passing a ruby laser beam through the medium. Fluorescent radiation at 5847 Å was detected depending on the output wavelength of the ruby laser in the presence of cesium vapor and hence proves the presence of the two-photon absorption. Figure 2(b) also illustrates a third resonant process in this system which is even more interesting and may be described as the stimulated analog of the second process or referred to as doubly resonant, four-photon, parametric amplification. This resonant phenomenon is like that of the stimulated Raman emission which is an enhanced form of the classical Raman effect in many organic liquids[5], since a chain reaction occurs when sufficient number of Raman photons in turn stimulate further Raman emission in the material. The experimental apparatus used in this work will be described in detail in Chapter 2 as well as the basic third-harmonic experiment.

In order to interpret experiments on cesium, theoretical aspects of third-harmonic generation in the medium must be studied. Maxwell's equations are applied to the

third-harmonic generation with the nonlinear polarization as the additional source term. The problem of solving these equations with suitable boundary conditions may be referred to as the propagation problem. Several authors[8-13] have studied this problem extensively. However, due to the complication of the problem, general analytical solutions are usually not available and in some cases only numerical results are obtained. We wish to make an extension to the case of inhomogeneous media in which the problem becomes more involved but of considerable interest and relevance to our experiment. In Chapter 3, we formulate a theory in seeking the solution of the propagation problem, in which the results for the plane wave case and the focused beam case in inhomogeneous media are compared with their counterparts in homogeneous media. Experimental verification of these solutions is presented together with the theoretical result exhibited by vibration curves. This theory is used to derive the nonlinear coefficient of resonant third-harmonic for cesium from the experimental data.

In Chapter 4, we describe the experiments on cesium. The observation of the resonant third-harmonic generation in cesium vapor by a tunable ruby laser is correlated to the observation of two-photon fluorescence. From the experimental data and the theory of the propagation problem, the absolute value of the resonant third-harmonic coefficient for cesium is determined. This value will be in turn compared with the quantum mechanical calculation

which was performed by B. Orr (see Appendix 1), with an additional averaging over the fundamental laser spectrum and the velocity distribution of the microscopic systems.

In Chapter 5, we report a preliminary study of four-photon parametric amplification in cesium together with the estimation of the gain coefficient by means of the experimental result and quantum mechanical treatment. Further work is needed here.

Finally, in Chapter 6, a brief summary and conclusion of the overall view of this work will be presented.

CHAPTER 2

EXPERIMENTAL APPARATUS AND BASIC THIRD-HARMONIC EXPERIMENT

The basic experimental setup used in this work consisted of a tunable ruby laser light source, beam optics, a sample cell, and two optical detectors. A schematic diagram of the apparatus is shown in Figure 3. In the following section, the apparatus will be described in greater detail. Then, in section 2.2, a basic third-harmonic generation experiment will be discussed as a prototype of other experiments performed in this investigation. More specific details of other experiments will be discussed in Chapters 3, 4, and 5.

2.1 Experimental Apparatus

The light source is a Pockels cell Q-switched tunable ruby laser (Spacerays Model 1010c). By controlling the temperature of the ruby rod in the cavity, the fundamental beam was tunable through a range of output wavelengths between 6943 Å at room temperature and 6934 Å near liquid nitrogen temperature. A graph of the ruby output wavelengths vs the temperature at a thermocouple near the ruby rod is displayed in Figure 4. Calibration of ruby output wavelengths is made by comparing with the cadmium doublet lines (4th order), 3466.20 Å and 3467.65 Å, using a grating monochromator (Spex Model 1400) with a Polaroid camera attachment. The

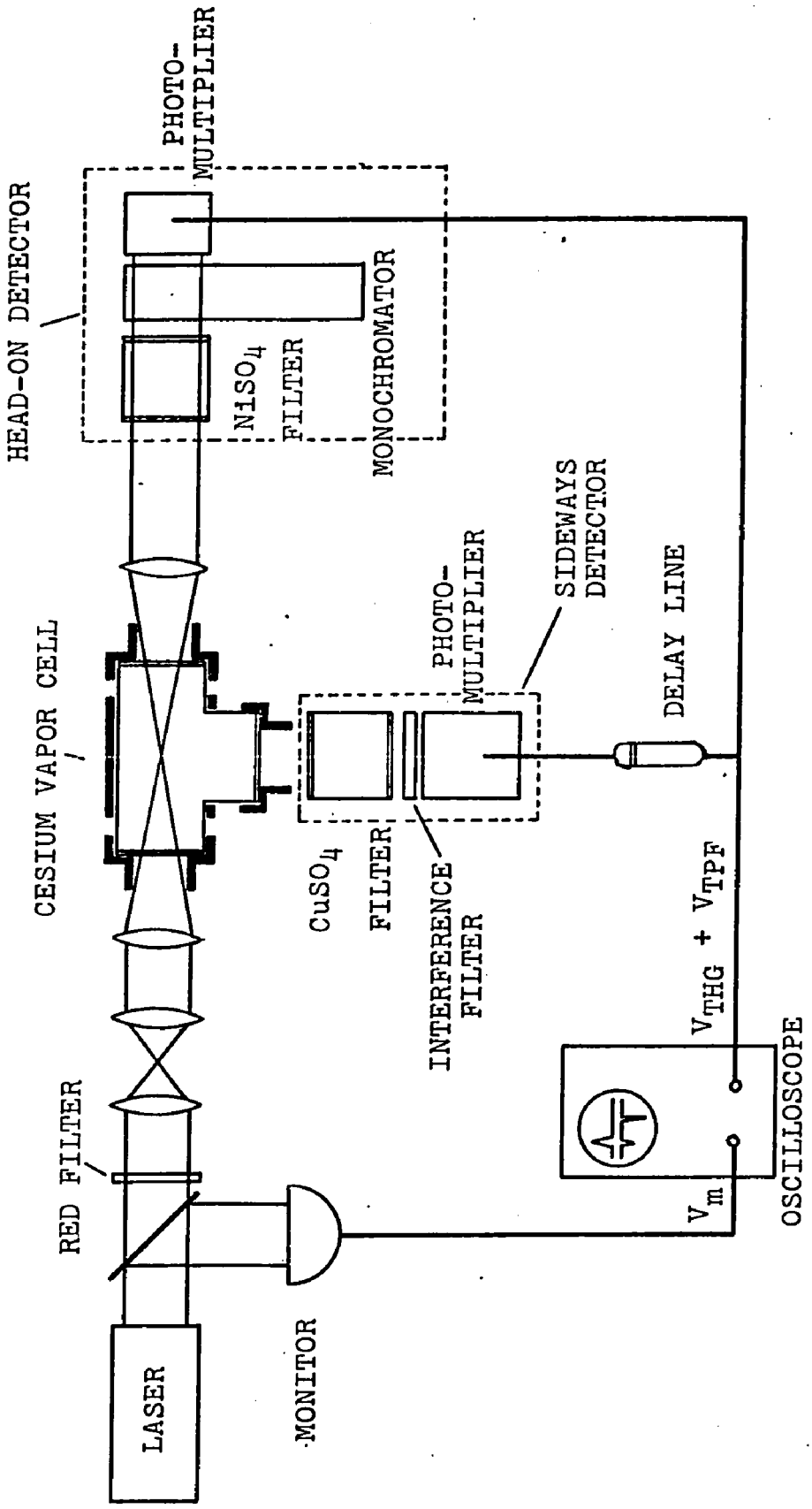


Figure 3. Schematic Diagram of Experimental Apparatus

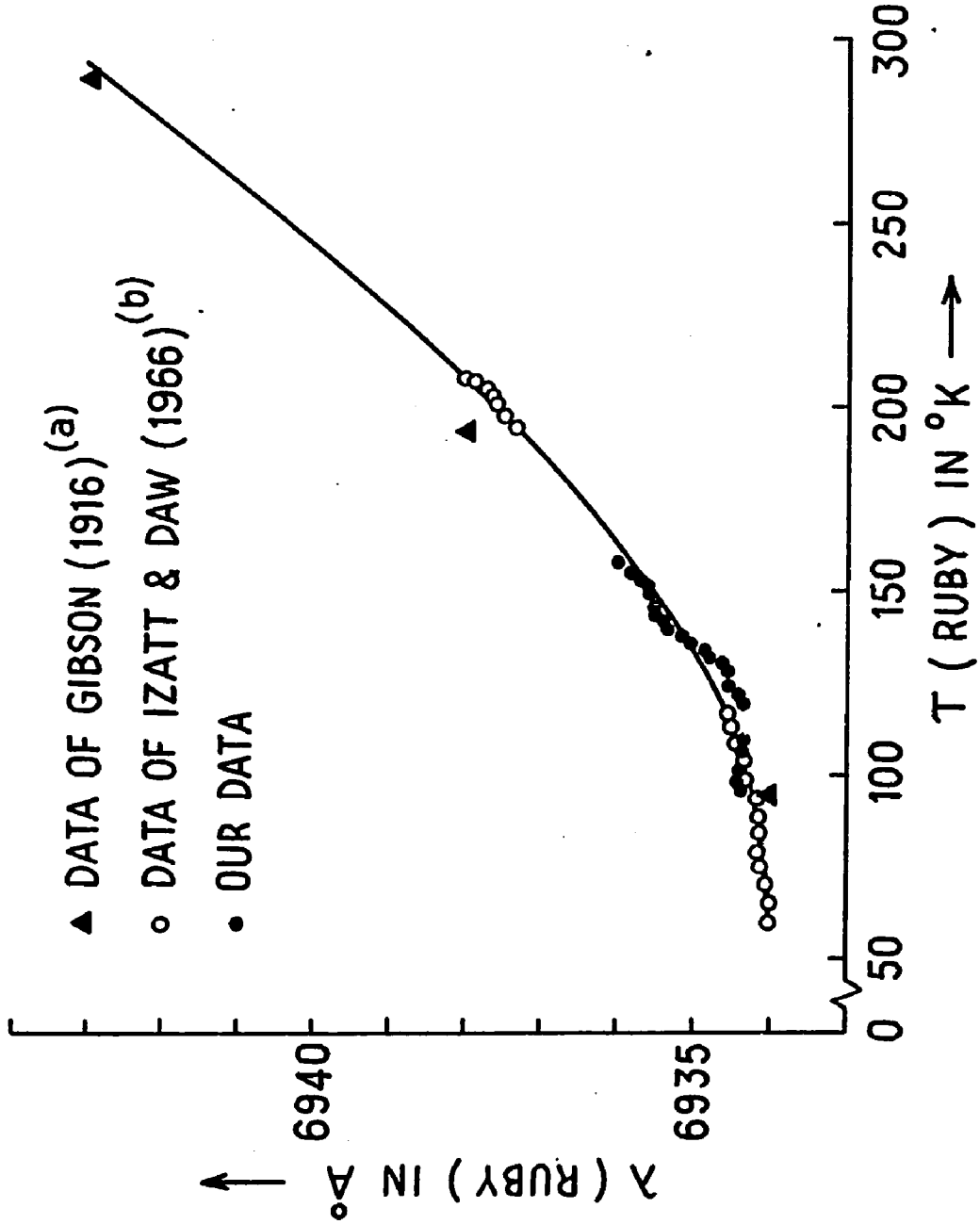


Figure 4. Variation of Ruby Laser Wavelength with Temperature. The graph includes (a) the absorption data of Gibson (see Ref. 6) and (b) data of Izatt et al., (see Ref. 7)

relative temperature of the rod was controlled by means of a temperature controller (Leads & Northrup 6260 Electromax on-off controller) within $1^{o}K$. The plane-parallel cut, 1/4" diameter x 4" length ruby rod produced a beam plane polarized in the vertical plane with a circular cross section of radius about 0.22 cm exhibiting multiple transverse modes. The linewidth and the longitudinal mode structure of the fundamental laser beam were studied by using a Fabry-Perot interferometer (Coherent Optics Model 380). The measured spectrum has an averaged linewidth of 0.10 cm^{-1} and the beam has a number of modes (one to eight) which increases with rod temperatures (see Figure 23). This multimode structure will be discussed in more detail in Chapter 4. The Q-switched laser output when operating at a repetition rate of one shot per 2 to 3 minutes at liquid nitrogen temperature is 0.025 joule (10^{17} photons) in energy and 25 nsec pulse full width at half maximum. The fundamental pulse, monitored with a photodiode (RCA 922), was displayed on one beam of a dual beam oscilloscope (Tektronix type 551 with 2 type L preamplifiers).

The laser beam passed first through a red filter (Chance OR1) to filter out uv light from the flash-lamps and then through a system of lenses. Typically two convex lenses were combined to collimate the beam since it was slightly divergent and to produce the required diameter. Another convex lens was used to focus the collimated beam into the sample cell.

For experiments on cesium vapor, a sample cell 18

cm long was constructed of stainless steel with three sapphire windows, of which one was located at 90^{o} with respect to the laser beam (see Figures 5 and 6). The cesium metal was distilled into a side arm which was maintained at a slightly lower temperature than the main cell. 1 Torr of neon buffer gas was placed in the cell before sealing. In order to avoid the condensation of cesium vapor on the surfaces of the windows, a length of 9 cm on the inner wall of tne central section of the cell was covered with a thick layer of copper-felt to absorb the condensed cesium liquid which was formed by a water cooling system between this section and the two sapphire windows. This arrangement and the neon buffer gas allowed the cesium vapor to circulate in the central portion of the cell and restrict condensation on the windows. In addition, three separate ovens, heating the three sapphire windows, were maintained at a slightly higher temperature than the main cell. An array of 12 copper-constantan thermocouples was spot-welded along the main body including the side arm of the cesium cell in order to estimate the relative temperature of the cesium vapor at different locations in the cell. This allows a crude estimate of the cesium vapor distribution and density. By controlling the side arm temperature from $90^{o}C$ to $300^{o}C$, the cesium vapor pressure could be continuously varied between $3x10^{-4}$ Torr and 1 Torr. Most of the experiments were performed at 0.1 Torr cesium vapor pressure (at $210^{o}C$). The failure of the side arm due to cesium corrosion limited the lifetime of a cesium

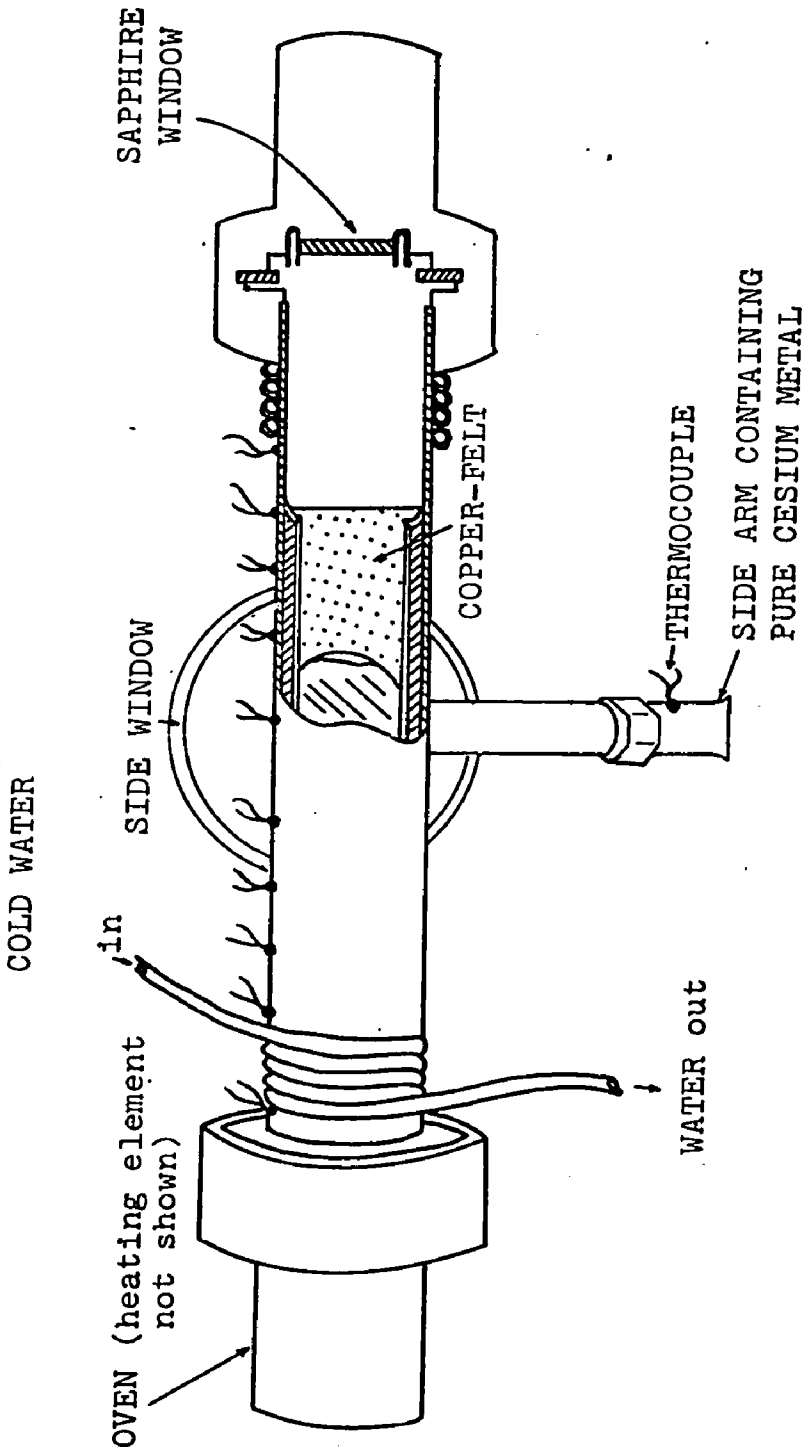
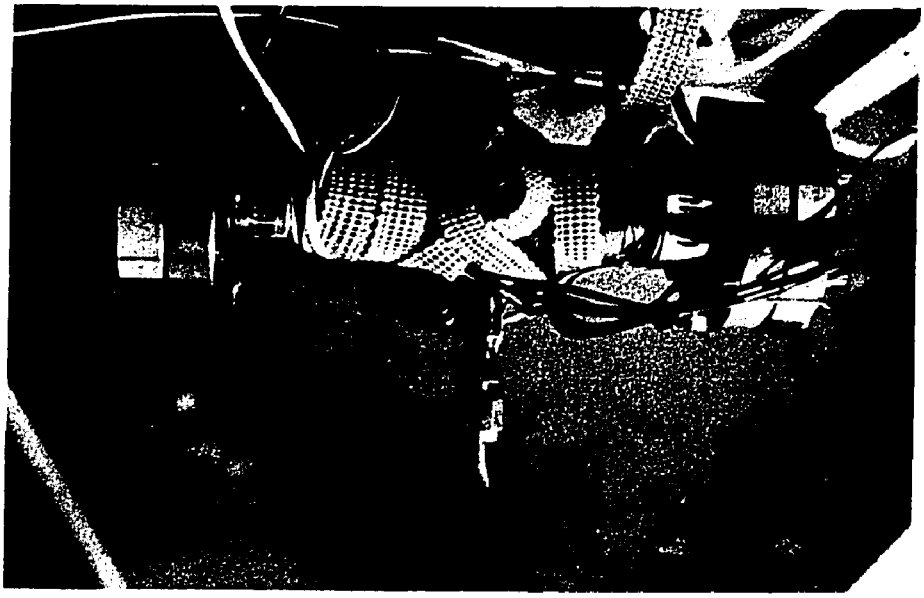
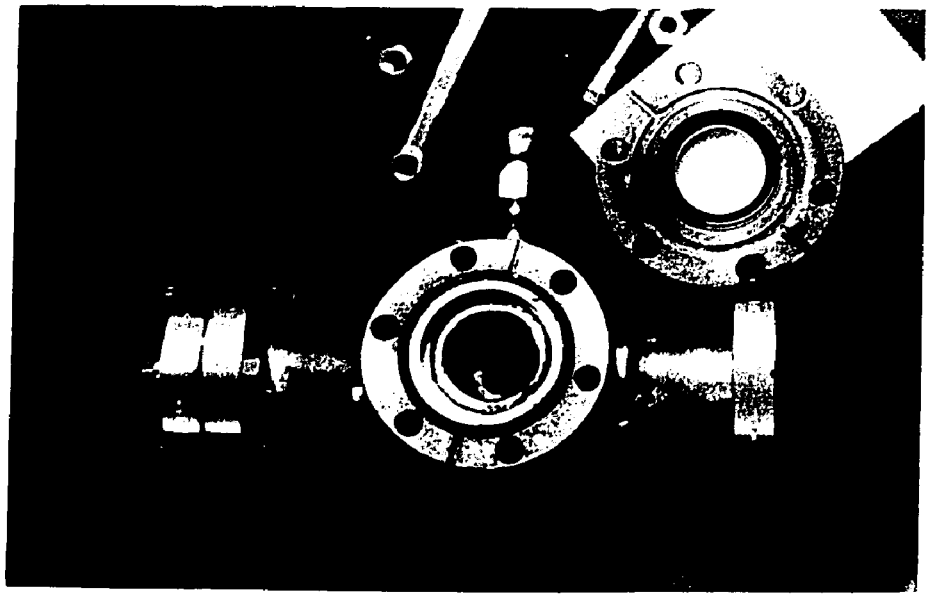


Figure 5. A Sketch of the Cesium Vapor Cell



(a) Assembly of the Cell



(b) Disassembly of the Cell

Figure 6. Cesium Vapor Cell

cell to about 100 hours of operation at 200°C.

Detection of third-harmonic light after the cell, hereafter referred to as the head-on detector, required optical components transparent to uv light. Collected by a 25 cm focal length quartz lens, the third-harmonic light was filtered from the fundamental beam by a quartz cell containing saturated aqueous $NiSO_4$ solution with 12% uv transmission and a quartz prism monochromator (Schoeffel QPM 305) having a resolution of 100 Å, and was detected with a photomultiplier (RCA 1P28) with quantum efficiency of 18% for third-harmonic radiation. The output signal from the photomultiplier, corresponding typically to 100 photoelectrons at the photocathode or about 2×10^4 third-harmonic photons originally generated, was displayed on the second beam of the dual beam oscilloscope.

Another detector, referred to hereafter as the sideways detector, was also set up to receive light radiation through the side window of the cell. This detector was used to observe fluorescent light following two photon absorption by the cesium. With a solid angle of 0.01 for detection, it consisted of a $CuSO_4$ filter cell with 0.5% transmission at sodium D lines, a narrow band-pass interference filter centered at 5850 ± 45 Å (or 5680 ± 35 Å) and a photomultiplier (RCA 1P21 or 931A) with 1.8% quantum efficiency at 5850 Å. The output signal from the photomultiplier, delayed for 800 nsec by a delay line, could be displayed on the oscilloscope together with the other two signals. Typical oscilloscope

traces are shown in Figure 18 of Chapter 4.

2.2 Observation of Third-Harmonic Generation in Cesium Vapor

A basic third-harmonic generation experiment consists of comparing the fundamental monitor output with the head-on detector output on the oscilloscope. Each comparison due to a single laser pulse yields the ratio

$$\mathbb{P}^{3\omega}/(\mathbb{P}^{\omega})^3 \equiv S^{THG} \propto V_{THG}/(V_m)^3 \qquad (2.1)$$

where V_{THG} and V_m are third-harmonic and laser monitor pulse heights respectively with $\mathbb{P}^{3\omega}$ and $\mathbb{P}^{\omega}$ as the corresponding peak powers. Here, we refer to S^{THG} as the third-harmonic signal at the detector and it depends on the nonlinear coefficient of the medium as well as geometrical and other parameters related to the dispersive properties of the medium.

It was observed that third-harmonic output was readily obtained from cesium vapor. There are a number of straight forward checks that third-harmonic is indeed being detected. The following checks were performed with a fixed experimental configuration. We noted that with negligible cesium vapor in the cell (at the room temperature), no third-harmonic signal was detected at any ruby output wavelength. With 0.1 Torr (or more) of cesium vapor in the cell (at 210°C of side arm), third-harmonic light was detected and S^{THG} was independent of $\mathbb{P}^{\omega}$ (cf Figure 20 of Chapter 4) at a fixed ruby output wavelength. It was also noticed that the third-

harmonic signal pulse was shorter in time duration than the fundamental pulse. To distinguish the harmonic signals from the breakdown signals, the monochromator was tuned away from the setting point for third-harmonic regularly to show the disappearance of the signals. Furthermore, since for an isotropic nonlinear medium, a plane-polarized fundamental generates a similarly polarized third-harmonic, a Glan prism was used to demonstrate this effect for third-harmonic signals detected from cesium vapor.

It was found that the third-harmonic signal from cesium vapor depended strongly on the ruby output wavelengths and beam optics, as well as the cesium vapor density distribution. Some of these experimental findings will be used to confirm the theoretical aspects of the propagation problem as will be described in Chapter 3, and to derive the nonlinear coefficient in Chapter 4.

CHAPTER 3

THEORY AND EXPERIMENTS OF THIRD-HARMONIC GENERATION IN AN INHOMOGENEOUS MEDIUM

In this chapter we derive an expression for the third-harmonic power reaching an optical detector when a medium with a given nonlinear coefficient is subjected to a specified strong fundamental field. An understanding of this propagation problem leads to a deeper insight of how to optimize the frequency conversion efficiency and to the determination of the nonlinear coefficient. This problem has been treated by several authors[8,9,10,11,12,13] for plane wave and focused fundamental fields. In particular, Ward and New[12] have presented an extensive analysis of harmonic generation of arbitrary order produced by focused fundamental fields in an homogeneous medium. We make the extension here to inhomogeneous media. After introducing the notation and stating the problem in more detail, the case of a plane wave fundamental in a homogeneous medium is reviewed and this is extended to the cases of inhomogeneous media and focused fundamental fields. The results are then explained by means of vibration curves and will be compared with experiments on atomic cesium vapor.

3.1 The Propagation Problem

In general, the applied electric field $\underline{E}(\underline{r},t)$ in

a medium is of the form

$$\underline{E}(\underline{r},t) = \frac{1}{2}\{\underline{E}^{\omega}(\underline{r})e^{-i\omega t} + \underline{E}^{\omega *}(\underline{r})e^{+i\omega t}\} \qquad (3.1)$$

where

$$\underline{E}^{\omega *}(\underline{r}) = \underline{E}^{-\omega}(\underline{r}) \qquad (3.2)$$

with

$$\underline{E}^{\omega}(\underline{r}) = \underline{E}_{o}^{\omega}(\underline{r})e^{ik_1 z} \qquad (3.3)$$

Here, $\hat{z}k_1$ is the fundamental wave vector propagating in the z-direction, and its magnitude is proportional to the refractive index n_1 at the fundamental frequency ω,

$$k_1 = n_1\omega/c \qquad (3.4)$$

The corresponding fundamental power can be written as

$$\mathbb{P}^{\omega} = \frac{c}{8\pi}\iint dxdy|\underline{E}^{\omega}(\underline{r})|^2 \qquad (3.5)$$

Since not more than one part in 10^{12} of this power gets converted into third-harmonic in a typical third-harmonic generation experiment on cesium, and the attenuation by other processes is found negligible, we make the assumption throughout our investigation that $\mathbb{P}^{\omega}$ is independent of z or

that there is negligible depletion of the fundamental in the medium.

The polarization of the medium may be written similarly as

$$\underline{P}^{3\omega}(\underline{r},t) = \frac{1}{2}\{\underline{P}^{3\omega}(\underline{r})e^{-i3\omega t} + \underline{P}^{3\omega*}(\underline{r})e^{+i3\omega t}\} \quad (3.6)$$

with

$$\underline{P}^{3\omega^*}(\underline{r}) = \underline{P}^{-3\omega}(\underline{r}) \quad (3.7)$$

Here, the polarization wave is propagating with a wave vector $\hat{2}k'$, which has a magnitude equal to

$$k' = 3k_1 = n_1(3\omega)/c \quad (3.8)$$

The atomic nonlinear coefficients, or the nonlinear tensor susceptibility for third-harmonic generation can be defined by the relation between the Fourier amplitudes of the harmonic polarization and the applied fields

$$P_i^{3\omega} = K(-3\omega;\omega,\omega,\omega)X_{ijkl}(-3\omega;\omega,\omega,\omega)E_j^{\omega}E_k^{\omega}E_l^{\omega} \quad (3.9)$$

where $X_{ijkl}(-3\omega;\omega,\omega,\omega)$ is the macroscopic third-harmonic tensor susceptibility and $X^*_{ijkl}(-3\omega;\omega,\omega,\omega)$ is defined by the complex-conjugate equation to equation 3.9. For nonresonant processes, $X_{ijkl}(-3\omega;\omega,\omega,\omega)$ is real but we are concerned

here with resonant processes where $X_{ijkl}(-3\omega;\omega,\omega,\omega)$ is complex. The symmetry of an isotropic medium restricts this tensor to have only one independent element, e.g. X_{zzzz}, where

$$X_{zzzz} = X_{iiii} = (X_{iijj} + X_{ijij} + X_{ijji}); \quad i,j=x,y,z;\ i\neq j. \tag{3.10}$$

Henceforward, unless specified otherwise, we abbreviate $X_{iiii}(-3\omega;\omega,\omega,\omega)$ to X for convenience. The constant K in equation 3.11 is given by[14].

$$K(-3\omega;\omega,\omega,\omega) = 1/4 \tag{3.11}$$

The average microscopic third-harmonic coefficient $\langle\chi\rangle$ can be related to the macroscopic third-harmonic coefficient

$$X = N\{L(3\omega)[L(\omega)]^3\}\langle\chi\rangle \tag{3.12}$$

where $L(\omega_i)$ is the ratio of local to applied field at ω_i and we may set it to unity for our case of low-pressure gaseous medium and hence

$$X = N\langle\chi\rangle \tag{3.13}$$

where N is the number density of microscopic systems in atoms per cm^3. For convenience, a parameter ρ' is introduced

as the ratio of number density N of a given system to a unit density, or

$$\rho = N/N_o \tag{3.14}$$

with N_o set at one atom per cm^3. Equation 3.9 becomes

$$P_i^{3\omega} = \frac{1}{4}\rho N_o \langle\chi\rangle E_j^{\omega} E_k^{\omega} E_l^{\omega} \tag{3.15}$$

Note that $\langle\chi\rangle$ here is an effective χ per atom. Since we consider a resonant process, it will depend critically on the spectrum of the fundamental wave and the velocity distribution of the atoms and also, possibly, collisional perturbations of the atoms. These features will be considered in more detail in Chapter 4. The nonlinear dipoles of this harmonic polarization generate third-harmonic radiation with intensity depending on their spatial distribution and the dispersive properties of the nonlinear medium. The resulting third-harmonic field of the form,

$$\underline{E}^{3\omega}(\underline{r},t) = \frac{1}{2}\{\underline{E}^{3\omega}(\underline{r})e^{-i3\omega t} + \underline{E}^{3\omega *}(\underline{r})e^{+i3\omega t}\} \tag{3.16}$$

where

$$\underline{E}^{3\omega *}(\underline{r}) = \underline{E}^{-3\omega}(\underline{r}) \tag{3.17}$$

is determined by the inhomogeneous wave equation

$$\underline{\nabla}\times\underline{\nabla}\times\underline{E}^{3\omega}(\underline{r}) - k^2\underline{E}^{3\omega}(\underline{r}) = 4\pi k_o^2\underline{P}^{3\omega}(\underline{r}) \qquad (3.18)$$

where $\hat{z}k$ is the third-harmonic free wave vector with a magnitude of

$$k = n_3(3\omega)/c \qquad (3.19)$$

with n_3 being the refractive index of the medium at 3ω; k_o is the harmonic free wave vector in vacuum. Note that in an isotropic medium, n_3 is usually greater than n_1 (normal color dispersion). Thus, the polarization wave and the third-harmonic wave have different k vectors and we define the mismatch wave vector, Δk given by

$$\Delta k = -|\Delta k| = k' - k = 3k_1 - k \qquad (3.20)$$

This mismatch parameter is usually small, i.e., $|\Delta k| << k', k$ (for cesium at 210°C, $|\Delta k| = 0.567\ cm^{-1}$, $3k_1 = 2.72\times10^5\ cm^{-1}$)(15).

The third-harmonic power can be written in a form analogous to equation 3.5,

$$\mathbb{P}^{3\omega} = \frac{c}{8\pi}\int\int dxdy\,|\underline{E}^{3\omega}(\underline{r})|^2 \qquad (3.21)$$

Hence, an observable quantity can be defined by

$$S^{THG} \equiv \frac{\mathbb{P}^{3\omega}}{(\mathbb{P}^{\omega})^3} \qquad (3.22)$$

which is the same as equation 2.1. The evaluation of this observable quantity in terms of the nonlinear coefficient is our primary objective in this analysis.

For the convenience of the reader, some of the most frequently used notations and parameters relating to the propagation problem introduced here and later on are tabulated with brief explanations in Table 2 at the end of this chapter.

3.2 The Plane Wave Fundamental

For a homogeneous medium, the number density of microscopic systems is constant and uniformly distributed in space. We consider first the simple case of plane wave fundamental. For a plane wave of infinite extent, we assume a fundamental beam propagated in the +z direction and polarized along the y direction:

$$\underline{E}^{\omega}(\underline{r}) = \hat{y}E_o^{\omega}e^{ik_1 z} \tag{3.23}$$

The generated polarization wave can be described according to equation 3.15 as

$$P^{3\omega}(z) = \tfrac{1}{4}N\langle\chi\rangle(E_o^{\omega})^3 e^{ik'z} \tag{3.24}$$

and the wave equation 3.18 is re-written as

$$\underline{\nabla}\times\underline{\nabla}\times E^{3\omega}(z) - k^2E^{3\omega}(z) = 4\pi k_o^2\{\tfrac{1}{4}N\langle\chi\rangle(E_o^{\omega})^3 e^{ik'z}\} \tag{3.25}$$

We try a solution of the form,

$$E^{3\omega}(z) = A(z)e^{ikz} \tag{3.26}$$

where A(z) is a slowly varying amplitude, i.e., the fractional change in A(z) per wavelength increment in z is small so that the second order derivatives of A with respect to z can be ignored as compared to terms involving $\partial A/\partial z$. With the boundary condition A(0) = 0, substitution of equation 3.26 into equation 3.25 leads to

$$\frac{dA(z)}{dz} = i\frac{\pi k_o^2}{2k} N\langle\chi\rangle (E_o^{\omega})^3 e^{i(\Delta k)z} \tag{3.27}$$

In integrating the last equation with respect to z, one immediately finds

$$A(z) = i\frac{\pi k_o}{2} N\langle\chi\rangle (E_o^{\omega})^3 \int_0^z dz' e^{i(\Delta k)z'} \tag{3.28}$$

Then the third-harmonic signal is derived by using equations 3.5, 3.21, 3.22, 3.26 and 3.28:

$$S^{THG} \equiv \frac{\mathbb{P}^{3\omega}}{(\mathbb{P}^{\omega})^3} = \left(\frac{8\pi}{c}\right)^2 N^2 \frac{\pi^2 k_o^2}{a^2} \sin^2\left(\Omega\frac{\pi}{2}\right) \left|\frac{\langle\chi\rangle}{\Delta k}\right|^2 \tag{3.29}$$

where the powers here refer to a portion of the beam with cross-sectional area a and we have introduced a parameter Ω

which is defined as the total number of coherence lengths in the medium,

$$\Omega = \int_0^z \frac{|\Delta k|}{\pi} dz' \qquad (3.30)$$

and is equal to z/ℓ_c here, with ℓ_c being the known coherence length defined by

$$\ell_c = \pi/|\Delta k| \qquad (3.31)$$

The maximum third-harmonic signal is achieved when $\Omega = 1, 3, 5, \ldots$ (an odd number of coherence lengths).

Now, we can proceed to modify the theory of a homogeneous medium to the situation where the plane wave fundamental is incident on an inhomogeneous medium. Two distinct complications must be considered here. First, the number density of a given microscopic system is not a constant anymore, instead it will be in a form of

$$\rho \rightarrow \rho(z) = \rho_{max} f(z) \qquad (3.32)$$

The dispersive properties of the nonlinear medium are z dependent, and as a result, the mismatch parameter Δk as well as other wave vectors are also function of z, e.g.,

$$\Delta k \rightarrow \Delta k(z) = \rho_{max} (\Delta k)_o f(z) \qquad (3.33)$$

where $(\Delta k)_o$ is a constant mismatch wave vector evaluated at N_o and is equal to -1.89×10^{-16} cm^{-1} for cesium[15]. Secondly, since the phase of each wave is changing in the medium, the reflected free wave will couple with the transmitted wave. This effect is negligible because

$$(1/k^2)(\partial k/\partial z) << 1 \qquad (3.34)$$

For our experiments on cesium, $(1/k^2)(\partial k/\partial z) \approx 10^{-7} << 1$. Under these circumstances, we can follow the same approach as for the homogeneous case by writing down a set of equations to lead to the final expression of the third-harmonic signal: The fundamental field analogous to expression 3.23 is

$$E^{\omega}(z) = E_o^{\omega} \exp\{i\int_0^z k(z')dz'\} \qquad (3.35)$$

The resulting polarization wave analogous to equation 3.24 is given by,

$$P^{3\omega}(z) = \frac{1}{4}[\rho_{max} N_o f(z)] \langle\chi\rangle (E_o^{\omega})^3 \exp\{i\int_0^z k'(z')dz'\} \qquad (3.36)$$

To look for a solution of the third-harmonic wave subject to the inhomogeneous wave equation similar to equation 3.25, we try a solution of the form,

$$E^{3\omega}(z) = A(z)\exp\{i\int_0^z k(z')dz'\} \qquad (3.37)$$

similar to equation 3.26. The slowly varying amplitude is then found immediately by writing an analog of equation 3.28,

$$A(z) = i\int_{-\infty}^{+\infty} dz' \frac{\pi k_o^2}{2k(z')}[\rho_{max}N_o f(z')] \langle\chi\rangle (E_o^{\omega})^3 \exp\{i\int_0^{z'}\Delta k(z'')dz''\} \qquad (3.38)$$

At this point, we approximate all wave vectors except the mismatch wave vector Δk to be constant with z in the active region of the medium. For experiments on cesium, the form of density distribution is found to be a bell-shaped function. The limits of the integral are set at $\pm\infty$ since at large distances from the center of the cell no third-harmonic is generated. Therefore, with all these considerations, after performing the algebra, we then obtain the third-harmonic signal as

$$S^{THG} = (\frac{8\pi}{c})^2 N_o^2 \frac{\pi^2 k_o^2}{a^2} \sin^2(\Omega\frac{\pi}{2}) \left|\frac{\langle\chi\rangle}{(\Delta k)_o}\right|^2 \qquad (3.39)$$

which is identical to equation 3.29, where Ω is still the total number of coherence lengths given by equation 3.30.

The results indicate that the plane wave fundamental incident in an inhomogeneous medium generates third-harmonic signal independent of the form of density distribution in the medium so long as reflection can be ignored.

3.3 The Focused Fundamental

To represent a focused laser beam in a homogeneous medium, we take the lowest-order Gaussian mode[16]:

$$E^{\omega}(r) = E_o^{\omega} \frac{e^{ik_1 z}}{1 + i\xi} \exp\left(- \frac{k_1(x^2 + y^2)}{b(1 + i\xi)} \right) \qquad (3.40)$$

It is noted that in reality, the laser beam used in the experiment has a complicated mode structure. However, the resulting solution is in useful qualitative agreement with experiment. The multimode beam problem is more complicated but can be solved in principle by introducing additional terms involving higher powers of $(1 + i\xi)$ in the denominator of equation 3.40. Here, b is the confocal parameter related to the far-field diffraction angle δ_1 and the beam waist radius w_o by

$$b = \frac{4}{k_1 \delta_1^2} = k_1 w_o^2 \qquad (3.42)$$

and ξ is a normalized z-coordinate related to the focal position at z = f by

$$\xi = \frac{2}{b}(z - f) \tag{3.42}$$

Figure 7(a) depicts the geometry of a Gaussian beam to clarify the meaning of the notation. An extensive analysis of this problem for harmonic generation of arbitrary order has been presented by Ward and New[12]. One can also solve this problem by previous prescription given in Section 3.2. Here, for brevity, we write down directly the solution of the third-harmonic field for comparison:

$$E^{3\omega}(r) = i\frac{\pi k_o^2 b (E_o^{\omega})^3}{4k} N\langle\chi\rangle \frac{e^{ik'z}}{(1 + i\xi)} \exp\left(-\frac{k'(x^2 + y^2)}{b(1 + i\xi)}\right) I^{THG} \tag{3.43}$$

where

$$I^{THG} \equiv \int_{-\zeta}^{\xi} d\xi' \frac{\exp\{\tfrac{1}{2}ib\Delta k(\xi' - \xi)\}}{(1 + i\xi')^2} \tag{3.44}$$

and $-\zeta$ is $-2f/b$ which is the location of the vacuum interface.

The fundamental wave propagating in an inhomogeneous medium with varying density, propagation wave vectors, and refractive index can be written as

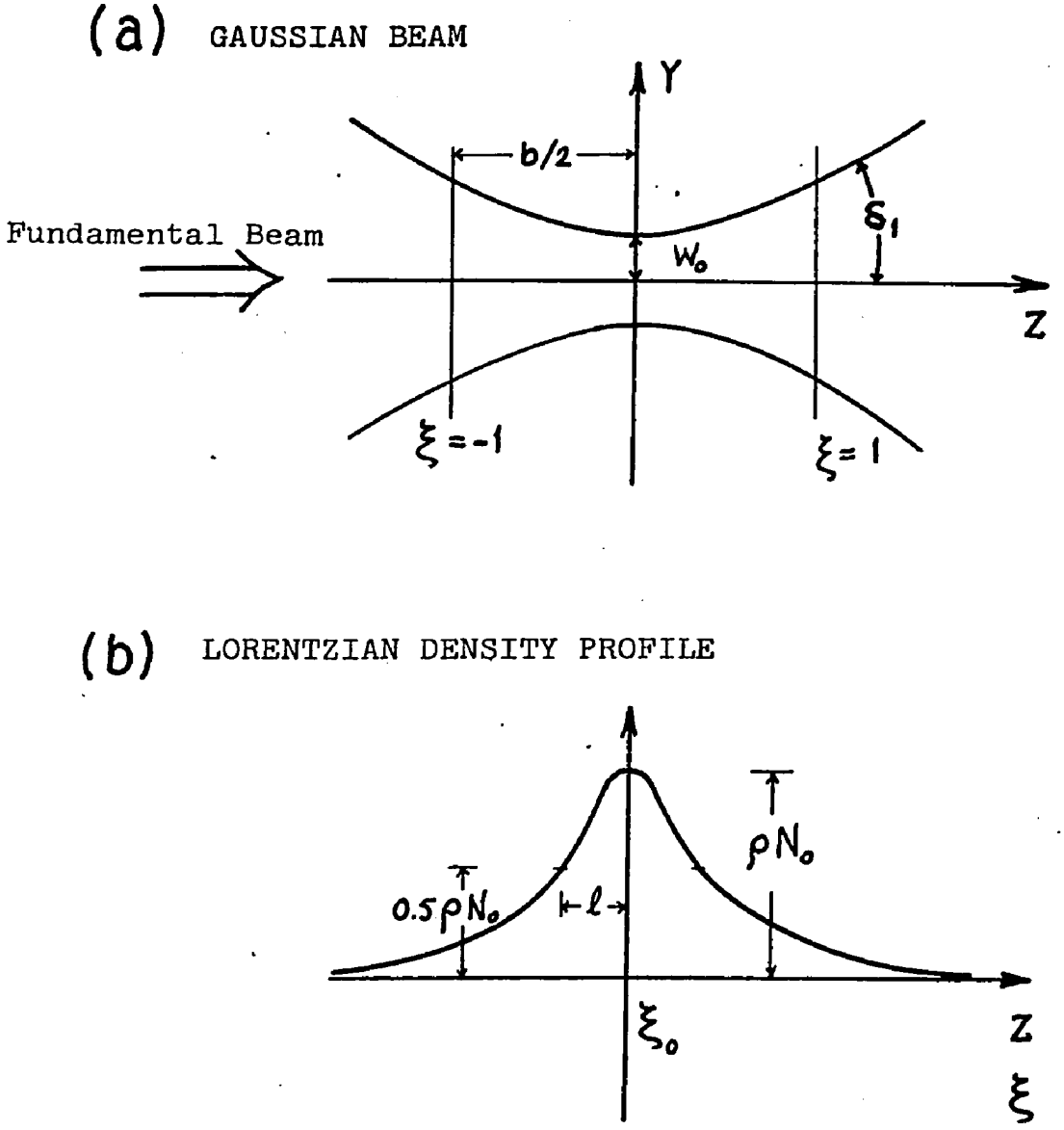


Figure 7. Notation for Third-Harmonic Generation by a Lowest-order Gaussian Beam in an Inhomogeneous, Nonlinear Medium

$$E^{\omega}(r) = E_o^{\omega} \frac{e^{i\int_0^z k_1(z')dz'}}{(1 + i\xi)} \exp\left(-\frac{k_1(z)(x^2+y^2)}{b\ (1 + i\xi)} \right) \quad (3.45)$$

As in the plane wave case an integral form for the phase is used and coupling to the reflected wave is ignored. An additional but unimportant effect arises here, of small refractive changes in the divergence angle and this is also ignored. The induced polarization wave has a form similar to that of equations 3.24 and 3.36,

$$P^{3\omega}(r) = \frac{1}{4} \rho_{max} N_o f(\xi) \langle\chi\rangle (E_o^{\omega})^3 \frac{e^{i\int_0^z k'(z')dz'}}{(1 + i\xi)^3}$$

$$\exp\left(-\frac{k'(z)(x^2+y^2)}{b\ (1 + i\xi)} \right) \quad (3.46)$$

The resulting inhomogeneous wave equation can be written as

$$\underline{\nabla} \times \underline{\nabla} \times \underline{E}^{3\omega}(r) - k^2(z)\ \underline{E}^{3\omega}(r) =$$

$$\vartheta\ 4\pi k_o^2 \{\frac{1}{4} \rho_{max} N_o f(\xi) \langle\chi\rangle (E_o^{\omega})^3$$

$$\frac{e^{i\int_0^z k'(z')dz'}}{(1 + i\xi)^3} \exp\left(-\frac{k'(z)(x^2+y^2)}{b\ (1 + i\xi)} \right) \} \quad (3.47)$$

In order to solve the above wave equation for the third-harmonic field, we again try a solution for the third-harmonic field similar in the form to the fundamental but with a slowly varying amplitude A(z),

$$E^{3\omega}(r) = A(z) \frac{e^{i\int_0^z k(z')dz'}}{(1 + i\xi)} \exp\left(- \frac{k(z)(x^2+y^2)}{b(1 + i\xi)} \right) \quad (3.48)$$

Substituting equation 3.48 into the wave equation 3.47 and after some manipulation of algebra, the third-harmonic field can be written as

$$E^{3\omega}(r) = i \frac{\pi k_o^2 b (E_o^{\omega})^3}{4k(z)} <\chi>$$

$$(1 + i\xi)^{-1} \exp\{i\int_0^z k'(z')dz'\}$$

$$\exp\left(- \frac{k'(z)(x^2+y^2)}{b\ (1 + i\xi)} \right) \ I^{THG} \quad (3.49)$$

where

$$I^{THG} \equiv \int_{-\infty}^{+\infty} d\xi' [\rho_{max} N_o f(\xi')\ (1 + i\xi)^{-2}$$

$$\exp\{i\frac{b}{2}\rho_{max}(\Delta k)_o \int_0^{\xi'} d\xi'' f(\xi'')\}] \quad (3.50)$$

The third-harmonic signal is obtained again in a similar manner to that of deriving equation 3.29,

$$S^{THG} = \frac{1}{3}\left(\frac{4\pi}{3c}\right)^2 k_o^4 \left| \langle \chi \rangle \right|^2 \left| I^{THG} \right|^2 \qquad (3.51)$$

The intensity of this signal is governed by the integral I^{THG} which must be evaluated for the individual experimental situation since general analytical solutions are not possible due to the essential singularities occuring in the integrand of I^{THG}. Nevertheless, we are interested only in a bell-shaped distribution of the effective nonlinear medium so that we now choose a Lorentzian profile for $f(\xi)$. This choice of $f(\xi)$ is crude but it will provide simple numerical evaluations and is as good as any other simple model since our experimental knowledge of $f(\xi)$ is also crude. Therefore, $f(\xi)$ takes the form of

$$f(\xi) = \frac{\ell^2}{(\xi-\xi_o)^2 + \ell^2} \qquad (3.52)$$

where ℓ is the half width at half maximum of the density in the normalized z-coordinate, and ξ_o is where the maximum density $\rho_{max}N_o$ is located (see Figure 7(b)).

The integral I^{THG} is then re-written in the form of

$$I^{THG} = \rho_{max} N_o \ell^2 \int_{-\infty}^{+\infty} d\xi' \frac{\exp\{-i\Omega \tan^{-1}(\frac{\xi'-\xi_o}{\ell})\}}{\{(\xi'-\xi_o)^2+\ell^2\}(1+i\xi')^2} \qquad (3.53)$$

For $\Delta k \neq 0$, sometimes it is convenient to write in the form of

$$|(\Delta k)_o| I^{THG} = \frac{N_o \ell^2}{d} \Omega \int_{-\infty}^{+\infty} d\xi' \frac{\exp\{-i\Omega \tan^{-1}(\frac{\xi'-\xi_o}{\ell})\}}{\{(\xi'-\xi_o)^2+\ell^2\}(1+i\xi')^2} \qquad (3.54)$$

where d is $b\ell/2$ which is the half width at half maximum of the density in the z-coordinate, and Ω is still the total number of coherence lengths and may be written

$$\Omega = \frac{1}{2} b\ell\rho_{max} |(\Delta k)_o| = d\ \rho_{max} |(\Delta k)_o| \qquad (3.55)$$

Since general solutions still cannot be obtained under these simplifications, we now examine the limiting cases for ℓ being very small and very large:

Case (1) Limit of ℓ is very small ($\ell \ll 1$)

In integrating the integral I^{THG} from -L to +L with $b \gg L \gg \ell$ (these limits of integration are justified since the region outside |L| is unimportant as the density is low there), the third-harmonic signal S^{THG} is obtained,

$$S^{THG} = \frac{2^8 \pi^2 k_o^2 N_o^2}{3c^2 w_o^4} \sin^2(\Omega \tfrac{\pi}{2}) \left| \frac{\langle \chi \rangle}{(\Delta k)_o} \right|^2 \qquad (3.56)$$

which is equivalent to that of the plane wave case with an effective area for the focused beam of $\sqrt{3/4}\,(\pi w_o^2)$.

Case (2) Limit of ℓ is very large ($\ell >> 1$)

In integrating the integral I^{THG} from -L to +L with $\ell >> L >> b$ (this is again justified since the region outside L is unimportant as the fundamental beam is weak there), the resulting signal is found to be the same as that for the homogeneous medium case (cf Ward and New[12]).

In addition, some specific cases have been evaluated and tabulated together with cases (1) and (2) in Table 1 for reference. Also, in the next section, we shall introduce a graphical method ("vibration curves") as a means of exhibiting I^{THG} and examining the optimum situation for third-harmonic output.

Table 1

SOME SPECIAL CASES OF I^{THG}

Case	ℓ and Ω (ξ_o=0)	I^{THG}	Remark
1	$\ell \ll 1$ Ω arbitrary	$\propto \sin(\Omega\frac{\pi}{2})$	Plane wave case
2	$\ell \gg 1$ $\Omega = 0$ or $\Delta k < 0$	0	Homogeneous medium
3	ℓ arbitrary $\Omega = 0$	$\pi\rho_{max}N_o\frac{\ell}{(\ell+1)^2}$	
4	$\ell = 1$ $\Omega = 0$	$\rho_{max}N_o\frac{\pi}{4}$	
5	ℓ arbitrary $\Omega = 2, 4, 6, \ldots$	0	
6	$\ell = 1$ $\Omega = -2$	$\rho_{max}N_o\frac{\pi}{2}$	

3.4 Vibration Curves

We discussed in Section 3.3 that the integral I^{THG} must be evaluated numerically and does not have a general solution. Ward and New[12] have pointed out that it would be helpful to consider a graphical interpretation such as the vibration curves which were commonly used in graphical treatments of diffraction in optics. A vibration curve is traced out by adding the infinitesimal vectors which represent in amplitudes and phases the contributions from different elements dz' (or $d\xi'$) of the integral I^{THG}. For our purpose, here, we shall first exhibit the integral I^{THG} by plotting out certain vibration curves corresponding to some specific cases of Table 2. Then, with the understanding of these curves and using data obtained by computer, we optimize three independent parameters relating to I^{THG}: Ω, ℓ (or b), ξ_0(or z_0) as defined in equations 3.52 to 54 to predict a more effective third-harmonic generation in an inhomogeneous medium and also to compare with experiments.

Vibration curves for the plane wave case correspond to an integral analogous to I^{THG} (cf equation 3.28). Figure 8 displays the case for Ω=0, 1, 1.5, and 2. Note that in the index-matched condition (Δk=0 or Ω=0) the curve is simply a straight line, but for arbitrary Ω, the mismatch parameter Δk winds up the curve in circular shape. In addition, maximum and minimum occur with Ω equal to 1 and 2 respectively. From this we learn that the circle is repeatedly retraced by the tail of the vibration curve as the nonlinear medium

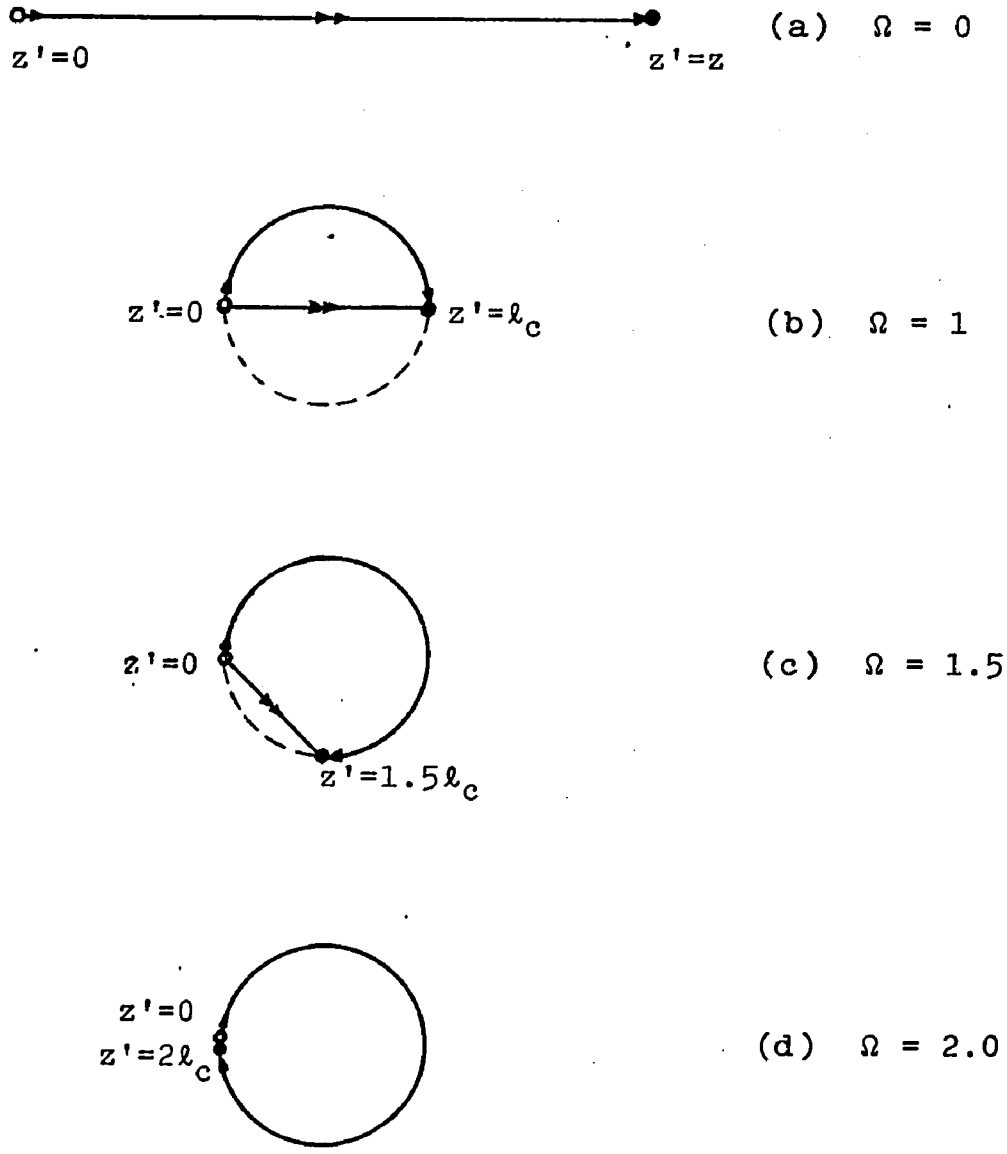
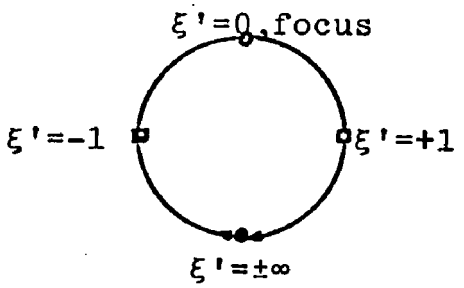


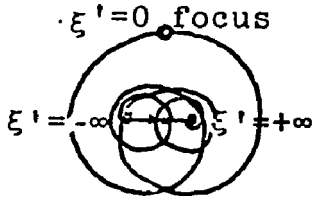
Figure 8. Vibration Curves for Third-Harmonic Generation by a Plane Wave Fundamental Beam

is lengthened, the harmonic field being a maximum whenever Ω is an odd integer and being a minimum for an even integer Ω as predicted from analytical expression of 3.29.

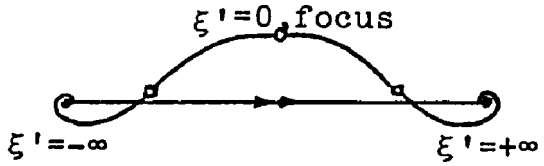
Figure 9 exhibits 6 vibration curves of the focused fundamental beam in an inhomogeneous medium corresponding to integral I^{THG} or $|(\Delta k)_o|I^{THG}$. For a focused beam, with $\Delta k=0$, the effect of focusing is to modulate the infinitesimal element or vector both in amplitude and in phase such that the curve is bent into a circle. If Ω is increased, the curve is wrapped up accordingly and is lengthened. The effect of the inhomogeneous density distribution is then to squeeze the curve. However, the ideal optimum condition is indicated by case (6) of Table 2, where Ω has a specific negative value which is not possible for us to verify experimentally with cesium vapor as the nonlinear medium. Hence, to optimize the third-harmonic field, we would like the curvature due to Ω or Δk for optimum output to be that due to focusing effect as indicated in Figure 9(c), i.e., $\Omega \sim 1$. Furthermore, we wish to choose the half-width ℓ of a given Lorentzian distribution to accentuate the first semi-circle due to effects of either focusing or Ω as indicated in Figure 9(e), i.e., $\ell \sim 1$. Thus, for $\Omega>0$, ℓ is chosen to be less than 1. With the above considerations, a series of vibration curves for the region of $\Omega \sim 1$, $\ell \sim 1$ at $\xi_o=0$ are plotted in Figure 10. Again it is thought that it will be best to put the dense medium in the strongest part of the beam, i.e., $\xi_o=0$. Figure 11 shows this is the case for



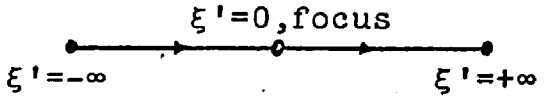
(a) $\ell >> 1$, $\Omega = 0$



(b) $\ell >> 1$, Ω = arbitrary

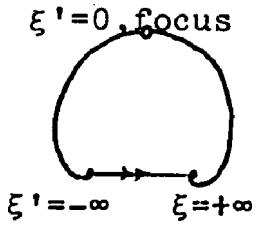


(c) $\ell >> 1$, $\Omega < 0$ (arbitrary)

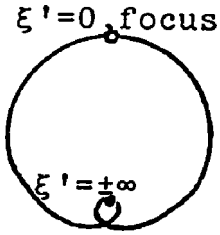


(d) $\ell = 1$, $\Omega = -2$

(note that $f(\xi)$ cancels the focused beam phase change)

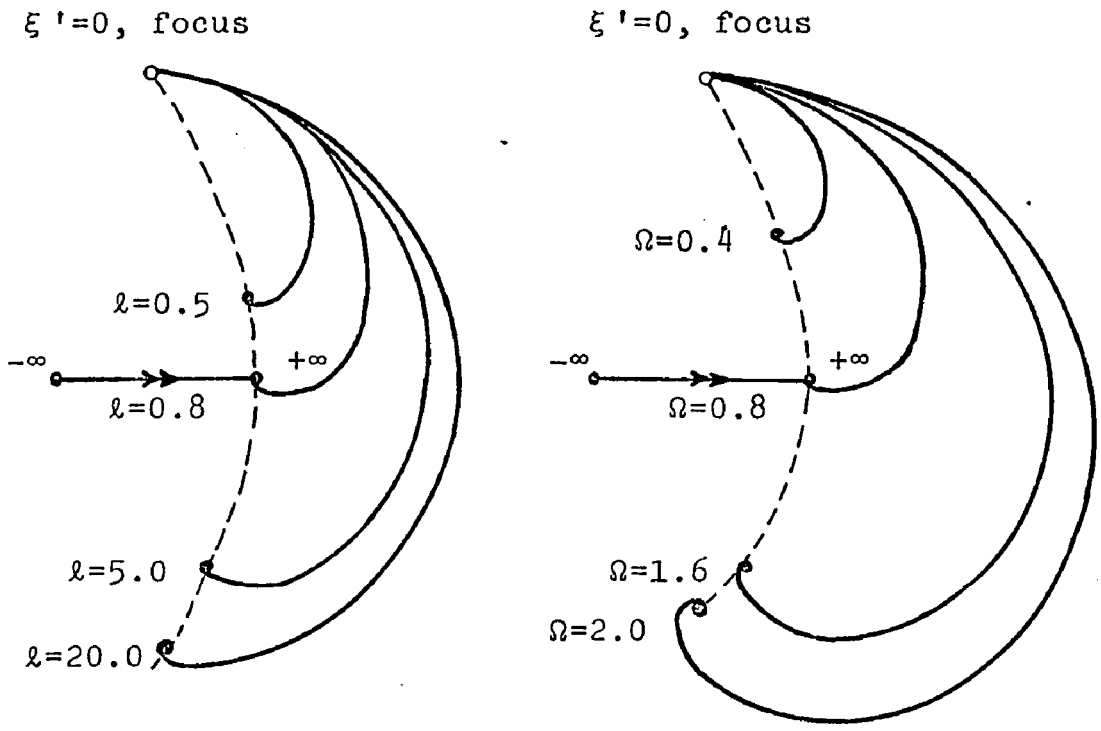


(e) $\ell = 1$, $\Omega = 0$



(f) $\ell = 1$, $\Omega = 2$

Figure 9. Vibration Curves for Third-Harmonic Generation by a Focused Fundamental Beam in an Inhomogeneous Medium



The resultant vectors represent the total third-harmonic field generated throughout the region from $-\infty$ to $+\infty$. Only the region $\xi' > 0$ is shown here, the other half-region can be obtained by reflection in the vertical line through $\xi' = 0$. For clarity, other resultant vectors are not shown.

(a) Optimize ℓ ($\ell > 0$) at $\Omega = 1$, $\xi_0 = 0$

(b) Optimize Ω ($0 < \Omega < 2$) at $\ell = 1$, $\xi_0 = 0$

Figure 10. Vibration Curves of Optimizing Parameters ℓ and Ω at $\xi_0 = 0$. (cf Figure 9(e) for a complete vibration curve shown).

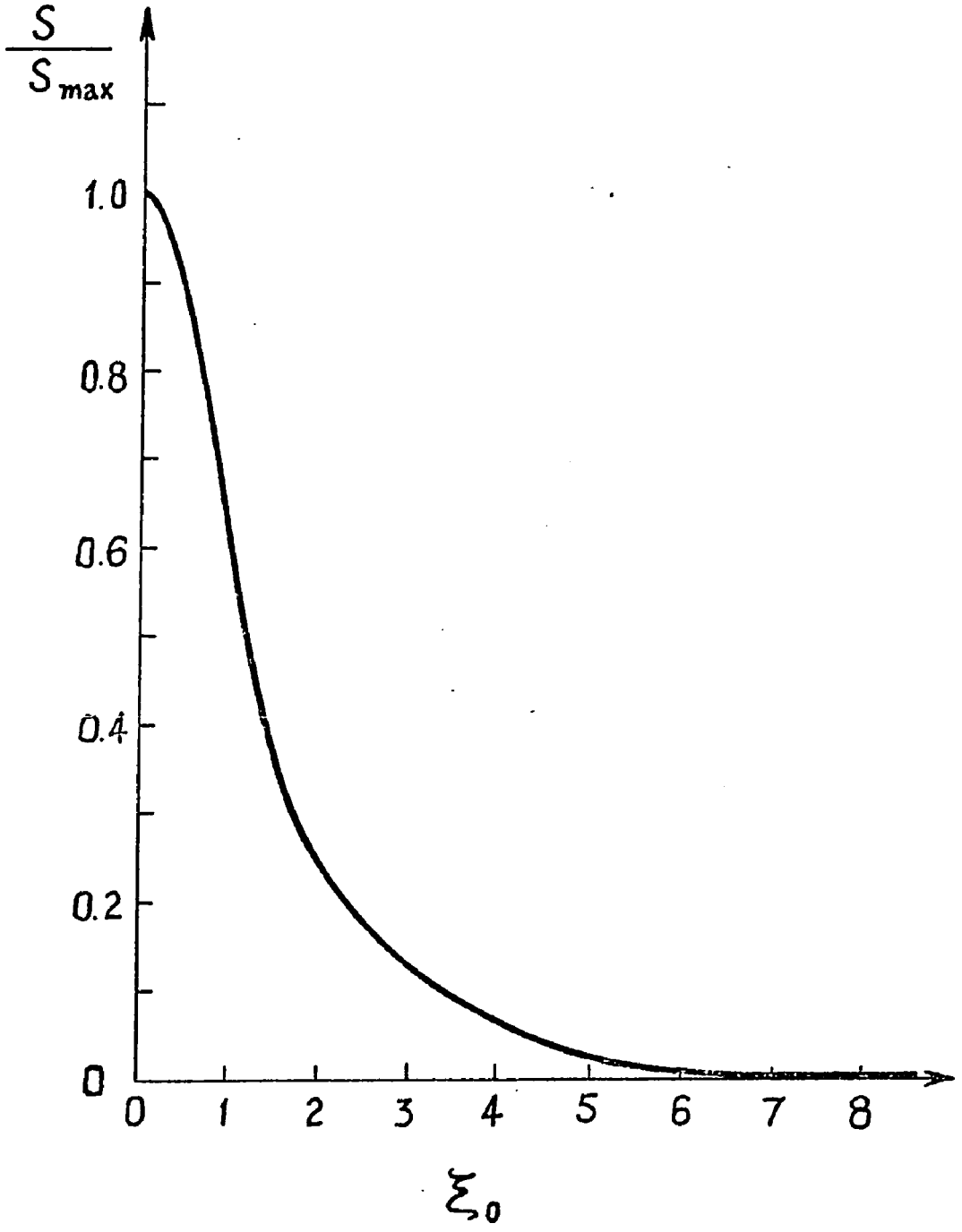


Figure 11. Theoretical Prediction of Signal Dependence on Focal Position with respect to Cesium Density. Other parameters are Ω=0.8 and ℓ=0.8, d is taken to be 3 cm.

Ω=0.8 and ℓ=0.8. Therefore, to obtain an optimum output of third-harmonic generation, it is best to set the three parameters in the situation of

$$\Omega = 0.8,\ \ell = 0.8, \text{ and } \xi_0 = 0.0 \qquad (3.57)$$

Some of the predictions of this section are confirmed experimentally and will be discussed in Section 3.5

3.5 Comparison With Experiments

In this section, we wish to verify the results of the previous section experimentally. For convenience and clarity, parameters relevant to the experimental measurements such as Ω, b, d, z_0 will be used in the following discussion superseding the corresponding normalized parameters used for theoretical discussion such as ℓ and ξ_0. The experimental conditions are specialized by keeping the ruby output wavelength fixed for peak response of the third-harmonic signal but varying the laser beam geometry and cesium vapor density in the cell. It is noted that a quantitative agreement between experiment and theory will be limited simply because the theory is for a single lowest-order Gaussian transverse mode whereas the laser beam is in fact multimode. However, such a theory has been shown to provide useful agreement with experiments in similar nonlinear optical processes, e.g., third-harmonic generation in gases[12], and dc-induced second-harmonic generation in gases[17].

It is interesting to give a crude estimate of the cesium vapor density distribution in the cell for comparison with experiments discussed in this section. However, the value obtained for the third-harmonic coefficient will not rely on this estimate. At a fixed side arm temperature, referred to as T_{Cs}, we measured the voltage at 12 thermocouples attached externally to the outside of the cell (cf Section 2.1) and take this as a measure of the cesium temperature on the axis of the cesium cell. Then from a thermocouple conversion table and a cesium vapor pressure table[18], we can plot the number density of cesium atom $N_{Cs}(z)$ as shown in Figure 12. This was done at various side arm temperatures. For each side arm temperature, we obtain a bell-shaped profile of the cesium density distribution. In the mathematical model of Section 3.3, this has been approximated by a Lorentzian function. Hence, the half-width d can be estimated from the plot $N_{Cs}(z)$ of Figure 12. It turns out that d is essentially independent of temperature in the range of interest and we have estimated d to be 3 cm (good to within 30%). By evaluating $\int N_{Cs}(z)dz$ and using Orr's calculated value of $(\Delta k)_o$, we can deduce the number of coherence lengths, $\Omega(T_{Cs})$ from equation 3.30. Figure 13 depicts $\Omega(T_{Cs})$ for the range of interest in our experiments.

Using the collimated laser beam, we now proceed to demonstrate the Ω dependence according to equation 3.39 which indicates the third-harmonic signal is proportional to $\sin^2(\Omega\frac{\pi}{2})$ for a given beam area. The harmonic signal was measured while

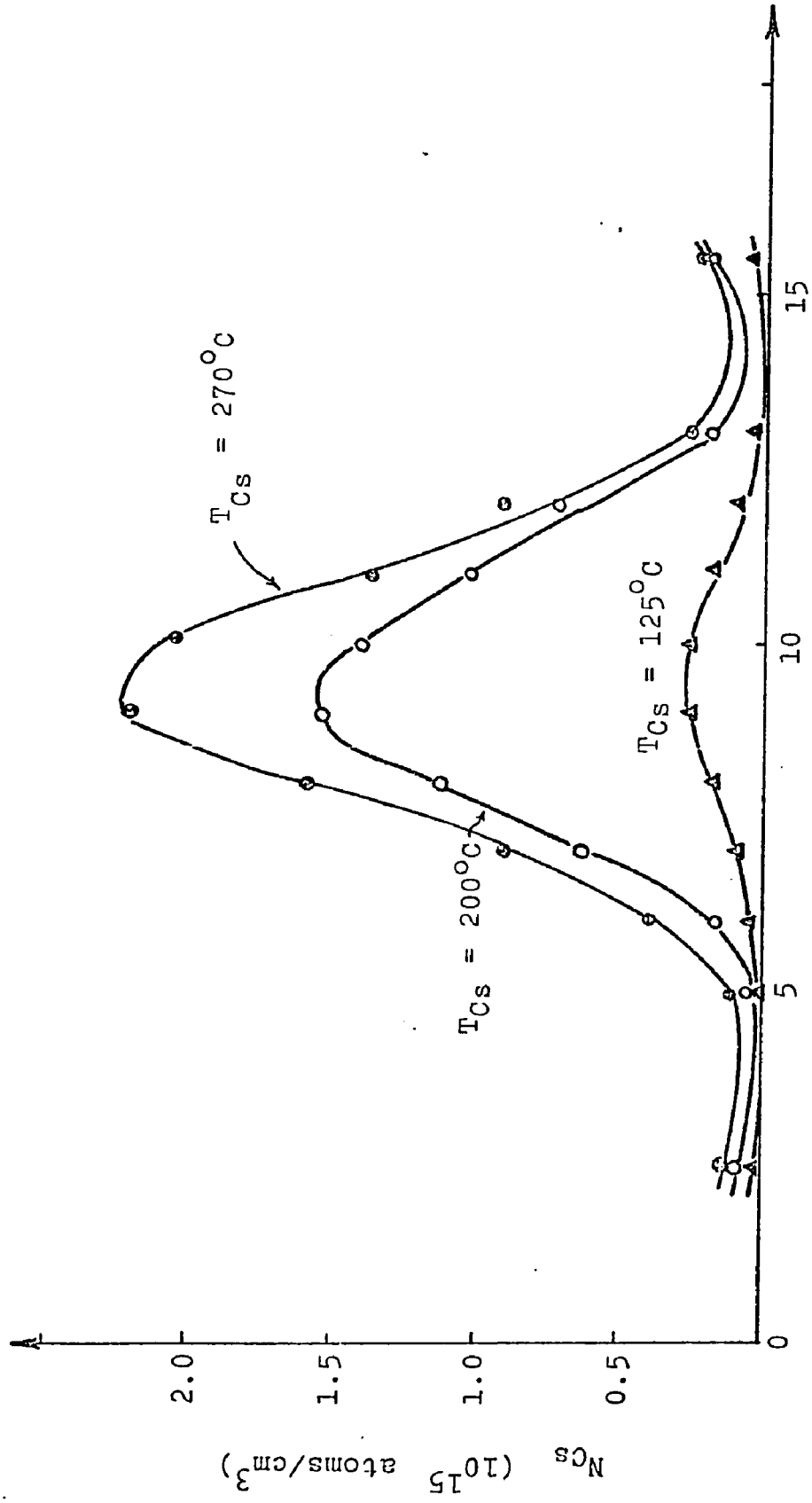


Figure 12. Cesium Density vs Cell Length

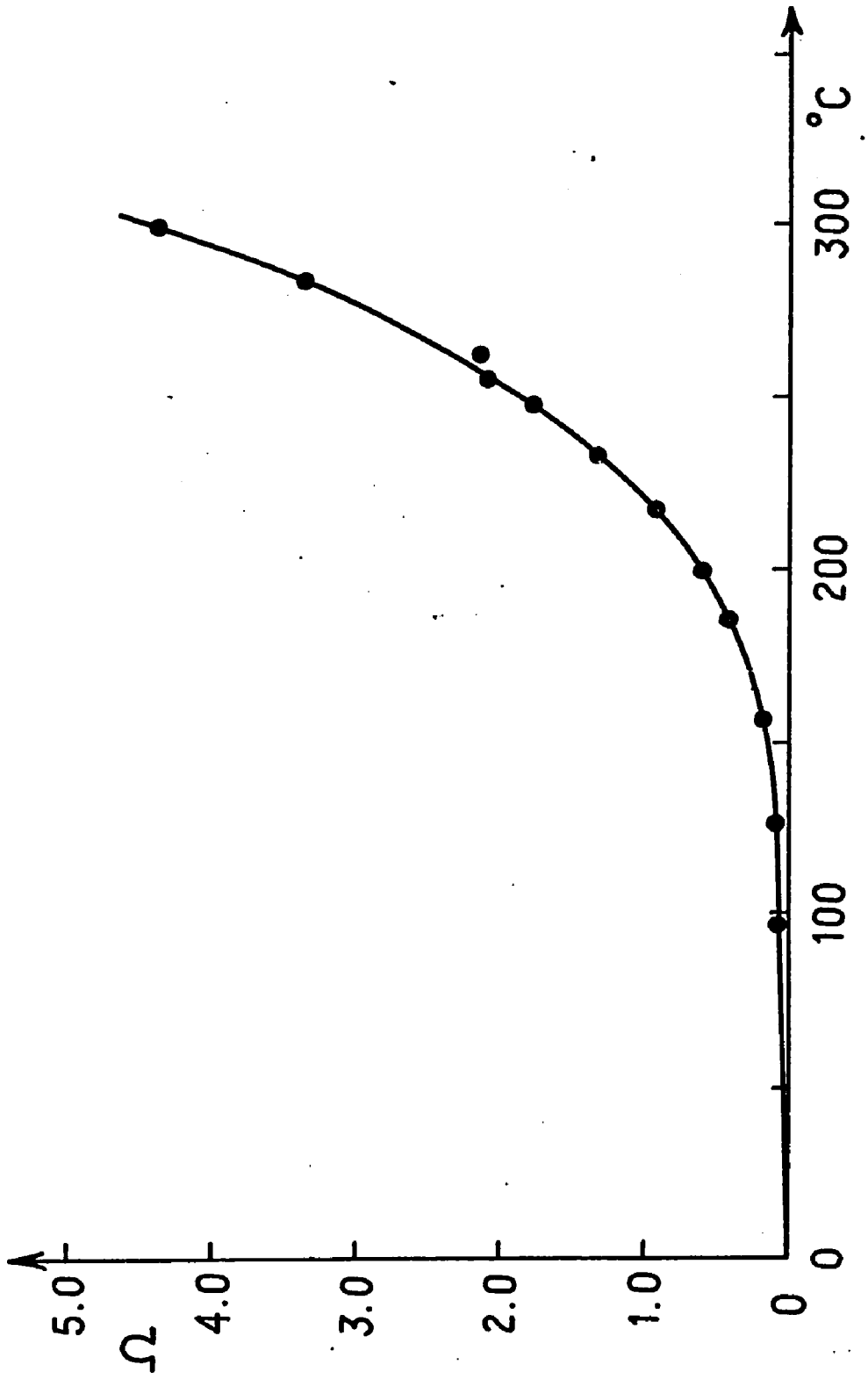


Figure 13. Number of Coherence Lengths vs Cesium Side Arm Temperature

varying T_{Cs}. Using previous data on $\Omega(T_{Cs})$ of Figure 13, the result is displayed in Figure 14, in which S^{THG} is normalized to unity at the maximum. It is interesting to note that S^{THG} has the qualitative feature predicted by equation 3.39 --- it is zero at the origin, increases to a maximum, comes down to zero and then increases again. This is independent of the details of our $\Omega(T_{Cs})$ calibration. In fact, it fits quantitatively the normalized theoretical curve $\sin^2(\Omega\frac{\pi}{2})$ rather well. This in turn gives us some confidence in estimating $\Omega(T_{Cs})$ (to within 10%) and in d (to within 30%) for use in the following experiments.

We now wish to examine the b dependence. In order to understand the experimental limitations on the range of b attainable, we digress briefly to examine the relationship between the beam radius w and the confocal parameter b, expressed in an equation derived by Boyd and Gordon[16],

$$kw^2 = b + \frac{(2z)^2}{b} \qquad (3.58)$$

where k is the wave vector at the fundamental frequency, and z is the distance measured along the axis from the focal plane. Figure 15 shows a plot of kw^2 in terms of b in which 2z is set to be the cell length. It is noticed that for w too large, the beam is apertured by the entrance cell window (for our case, 0.5 cm radius), and for w too small (for our case, 0.05 cm radius), breakdown occurs at the cell windows. Hence, this limitation on radius w allows us two distinct

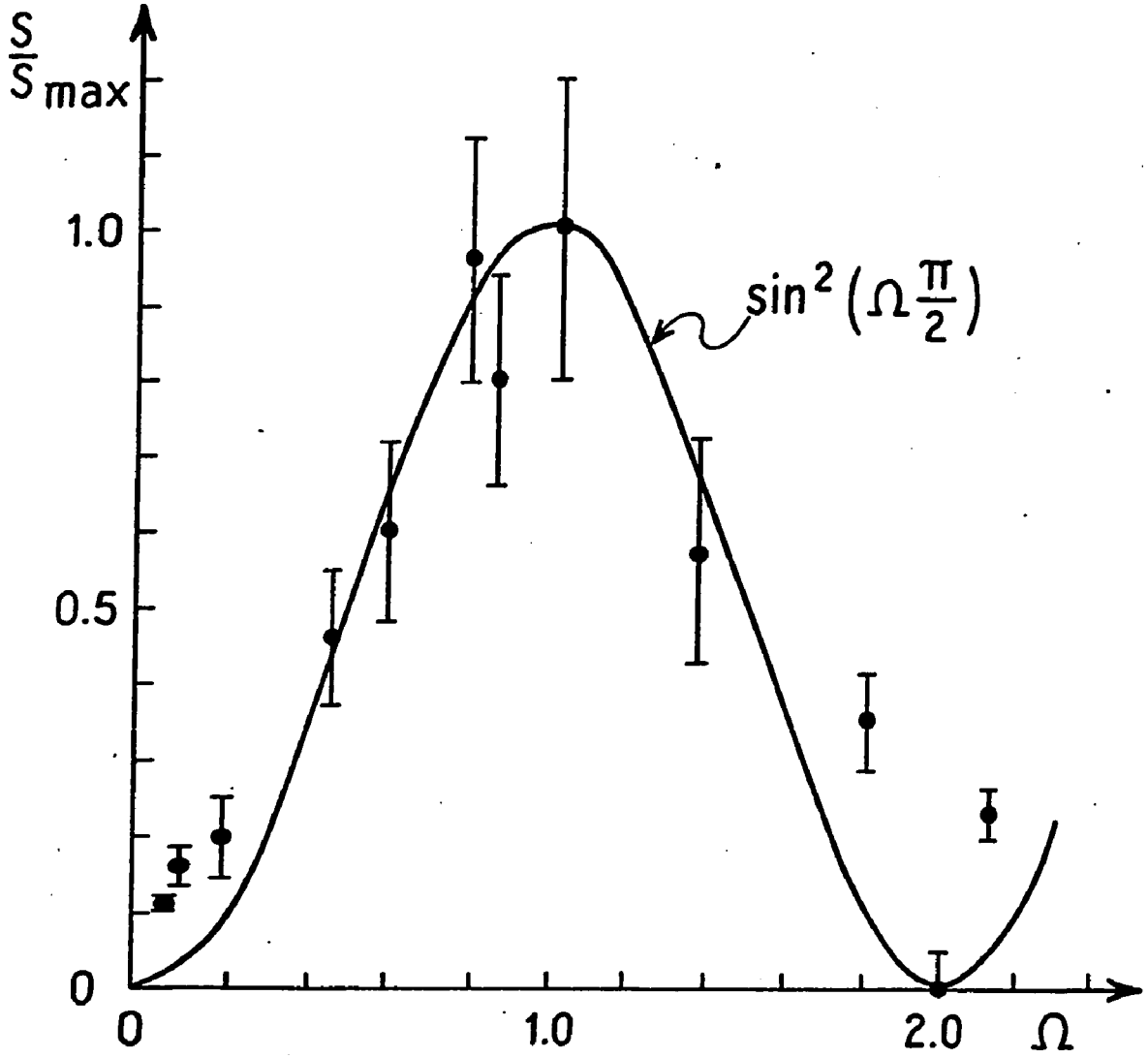


Figure 14. Signal Dependence on Number of Coherence Lengths

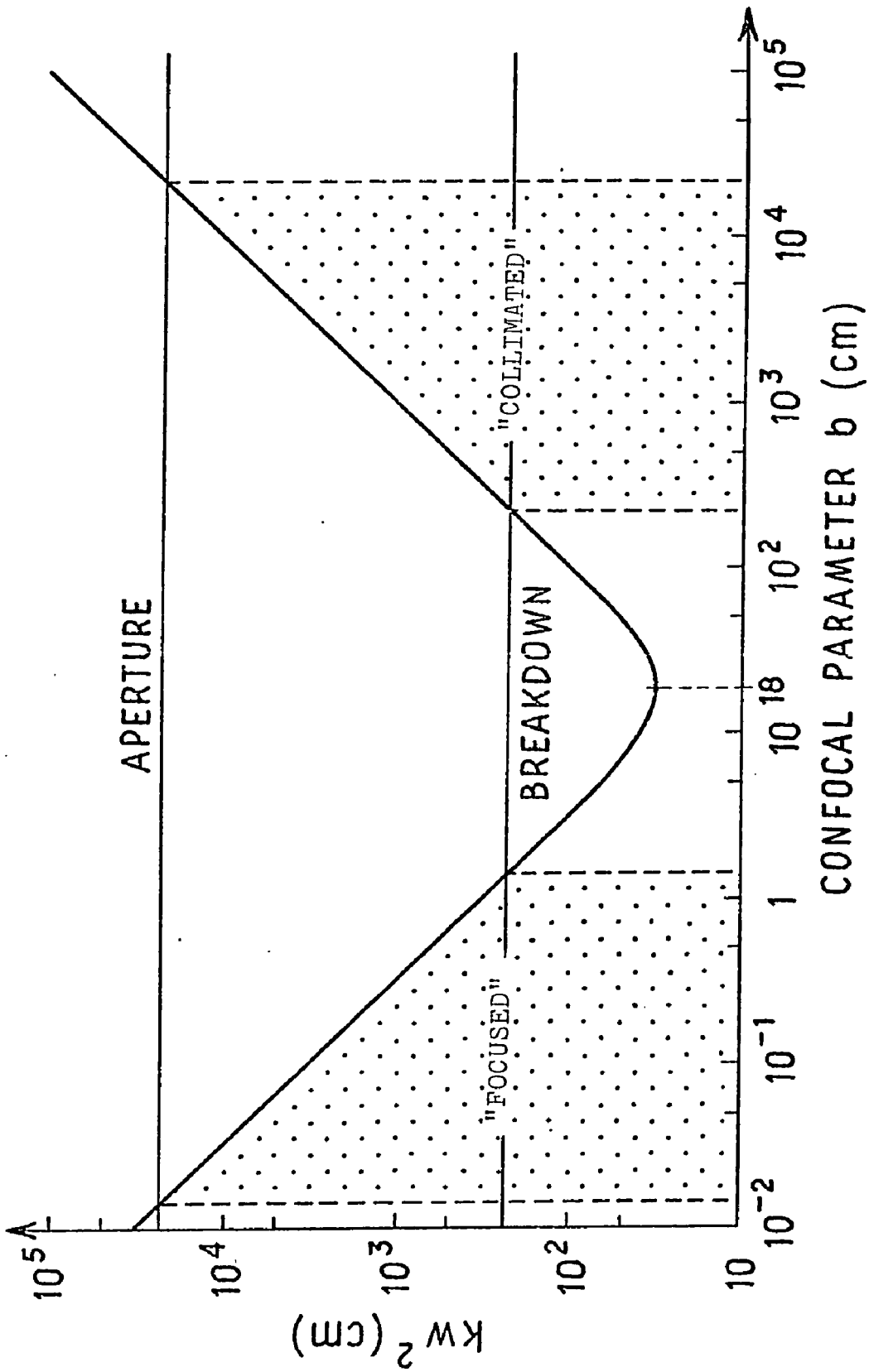


Figure 15. Operational Ranges of Confocal Parameter for Cesium Experiments

ranges of b values, namely, the "focused" and "collimated" beams (cf the dotted area in Figure 15). Although we stress the terms used here are just a matter of degree. We further specify the operational definition of b for the multimode laser beam and the relevant shortcomings will be discussed later. For a focused beam, we derive b from the focal length of the converging lens and the beam area at the lens (cf equation 3.41). For a collimated beam, b is obtained directly from the beam radius w_o.

With the above consideration, the b dependence was examined by using eight different b values corresponding to four focused beams and four collimated beams at a fixed experimental situation, i.e., $\Omega=0.72$, $z_o=0$, and d=3 cm. Figure 16 displays the third-harmonic signal as a function of b, where b as the abscissa and $\sqrt{S^{THG}}$ as the ordinate are in logarithmic scale. The error flags reflect the statistical fluctuation of the signals for a group of 15 shots at each b value. The same $\sqrt{S^{THG}}$ scale is used for both focused beam and collimated beam. It is noted that $\sqrt{S^{THG}}$ at maximum for the theoretical curve is arbitrary here in order to compromise between focused and collimated beams in fitting the experimental data.

From Figure 16, we note that a fair overall fit of multimode experiments with single mode theory over a wide range of b (6 orders of magnitude) and $\sqrt{S^{THG}}$ (2 orders of magnitude). There are deviations that can be explained qualitatively after we understand the shortcomings of the

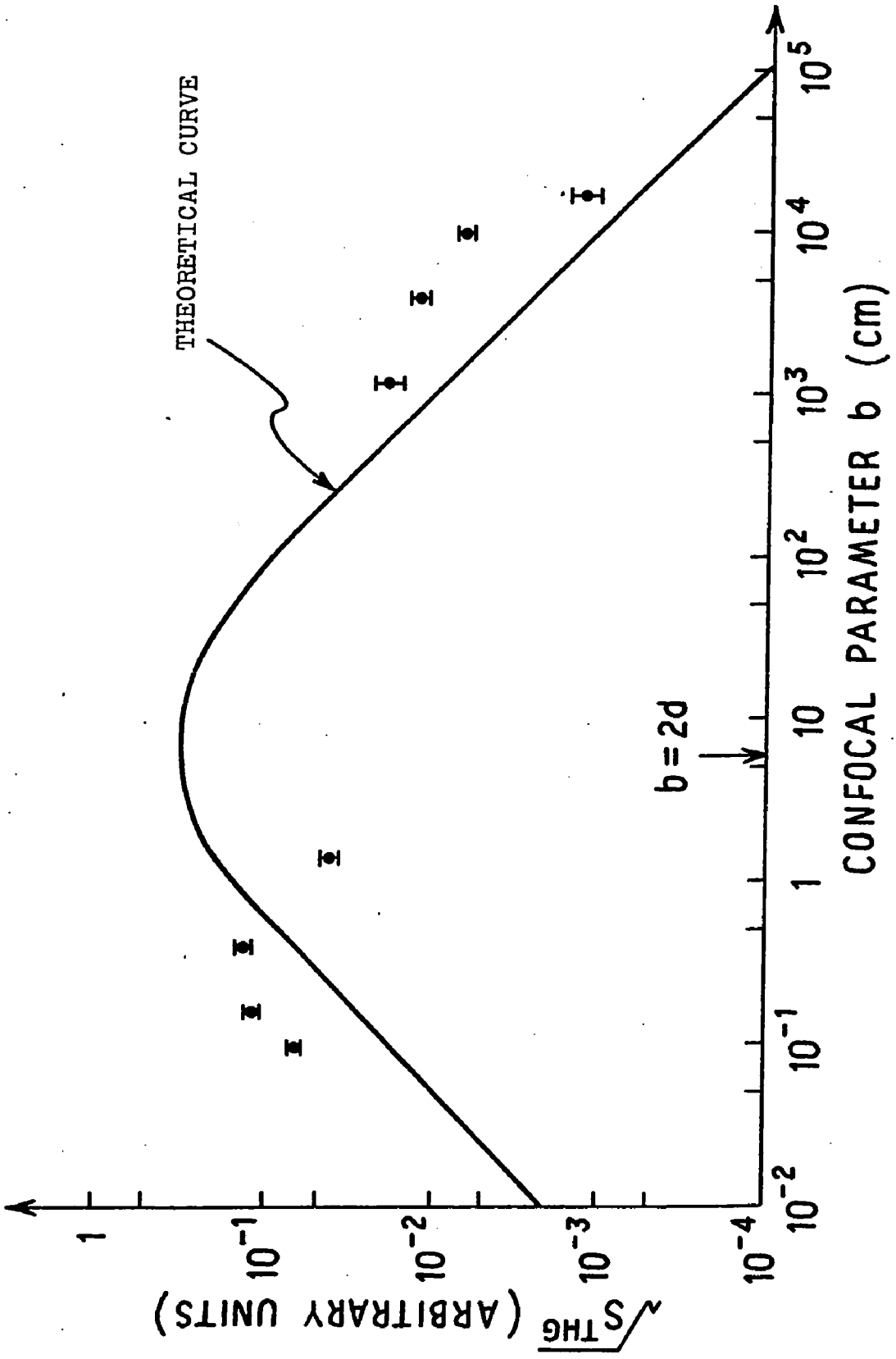


Figure 16. Signal Dependence on Confocal Parameter

operational definition of b. The shape of the $\sqrt{S(b)}$ curve can be understood as a compromise between two effects: Increasing b moves the phase changes in the fundamental beam further from the focus thus allowing more of the nonlinear medium to contribute constructively to the harmonic field. Reducing b reduces the focal area which increases the maximum electric field strength and tends to increase the signal. For a single mode beam, the b value implies a focal radius $w_o = \sqrt{b/k}$. For a multimode beam, however, the focal radius $(w_o)_{eff}$ will be much larger than w_o. Or writing $(w_o)_{eff} = \sqrt{b_{eff}/k}$, we have $b_{eff} > b$. In fact, Finn[17] has noticed that in his experiments on dc-induced second-harmonic generation in gases, good correspondence between multimode experiment and single mode theory is obtained by using an effective b value eight to eighteen times larger than that given by our operational definition for focused beams. Thus considering the details of Figure 16,

(i) The experimental maximum signal occurs at a b value twenty times smaller than that at which the single mode theoretical maximum occurs. This factor is comparable with that reported by Finn[17].

(ii) The experimental maximum signal falls below the single mode theoretical maximum. In going to smaller b to counteract the enlarged focal area of the multimode beam, some sacrifice in signal must result from reducing the distance from the focus at which a given phase change in the focused fundamental beam occurs.

(iii) For collimated beams, S^{THG} is above the theoretical curve. The reason is that we underestimate S^{THG} by assuming a smooth transverse distribution on the beam area. A non-ideal lumpy beam is expected to increase the third-harmonic signal.

Therefore, a single mode theory with qualitative modifications taking the multimode nature of the beam into account leads us to a theoretical picture consistent with the results of this experiment.

By keeping a constant side arm temperature, namely, at 230°C (corresponding to $\Omega = 1.25$) and constant beam optics (corresponding to b = 0.05 cm derived from equation 3.41), we next test the dependence of the signal on the axial position of the laser beam focus with respect to the center of the cesium distribution. In Section 3.4, we have argued that the third-harmonic signal will be a maximum for $z_o = 0$, and indeed this is the case as demonstrated by the experimental result. Figure 17 displays the result of S^{THG} on z_o dependence for six focal positions together with a set of theoretical curves with different b values. We again note here that the fit is good if $b_{eff} = 20$ b. In addition, if it had been possible to achieve a much smaller b_{eff} value, we should have been able to estimate d from the experimental result since in this limit the curve becomes independent of b.

We conclude here that the propagation problem for an inhomogeneous nonlinear medium has been demonstrated in

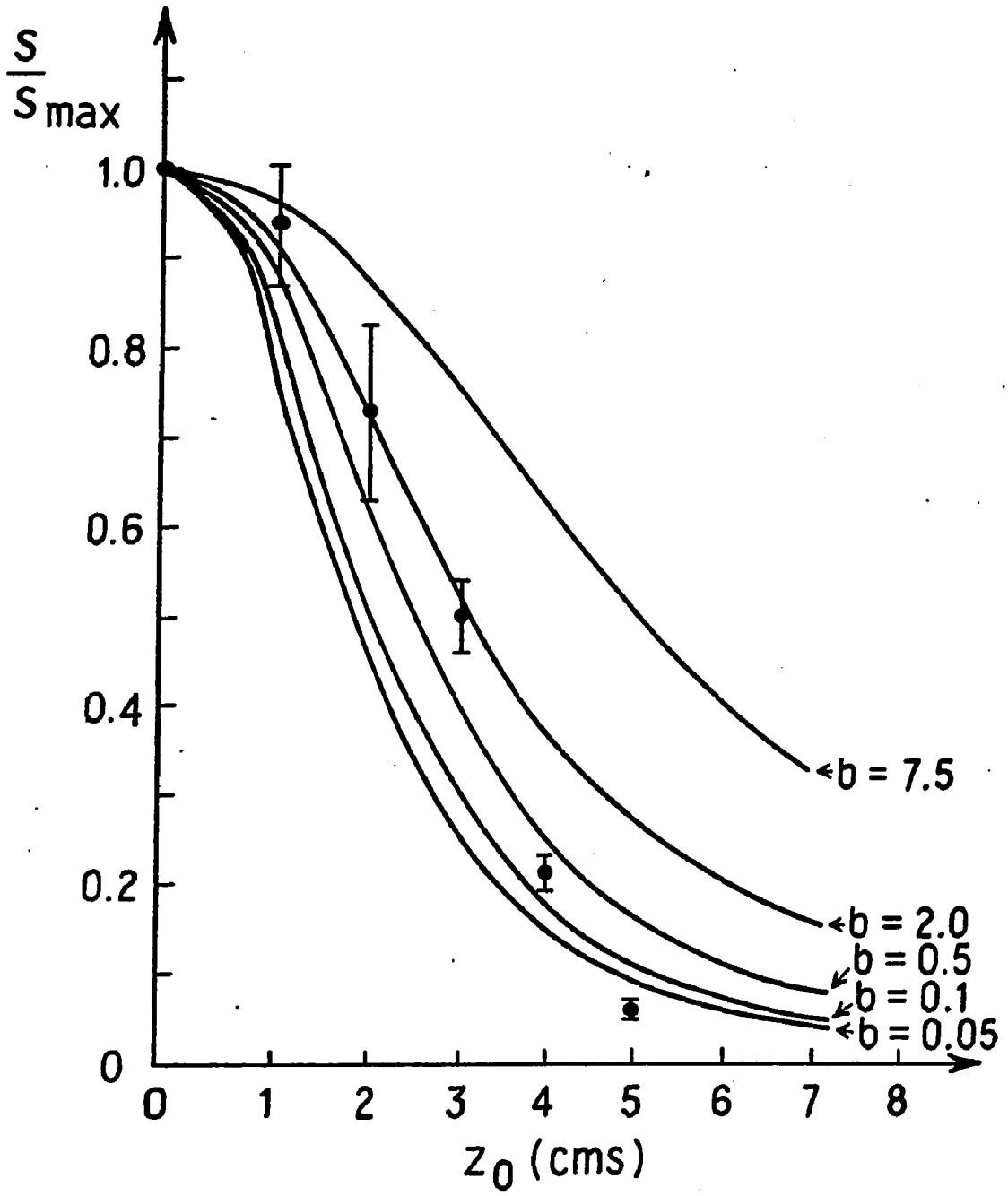


Figure 17. Signal Dependence on Focal Position with Respect to Cesium Density Distribution. Solid Curves Are Theoretical Calculations

a set of experiments on atomic cesium vapor. The dependences of the third-harmonic signal on three parameters of Ω, b (or ℓ), z_o (or ξ_o) were examined individually in order to compare with theory. A good fit over a wide range of b and $\sqrt{S^{THG}}$ has been obtained with a single mode theory modified by taking the multimode nature of the beam into account. We have predicted that the optimum harmonic signal S^{THG} could be obtained by focusing the beam (b = 2.5 d) into the dense medium (z_o = 0) at a fixed cesium side arm temperature (Ω = 0.8). But for our multimode beam, we found that in the experiment the b value should be twenty times smaller in order to achieve the optimum condition.

Table 2

LIST OF SYMBOLS

k_1	fundamental wave vector in the medium (equation 3.4)
$k' = 3k_1$	third-harmonic forced wave vector in the medium (equation 3.8)
k	third-harmonic free wave vector in the medium (equation 3.19)
k_o	third-harmonic free wave vector in the vacuum
$\Delta k = 3k_1 - k$	wave-vector mismatch (equation 3.20), at N_o of cesium vapor, it is $(\Delta k)_o$
Ω	total number of coherence lengths in the medium (equation 3.30)
N	number density in atoms per cm^3
N_o	unit number density in atom per cm^3
$\rho = N/N_o$	relative gas density (dimensionless)
$d = \frac{1}{2}b\ell$	half width at half meximum of the gas density distribution
ℓ	half width at half maximum of the Lorentzian density distribution in the normalized z-coordinate (equation 3.52)
b	confocal parameter of the fundamental Gaussian beam (equation 3.41)
δ_1	far field semiangular spread of the fundamental Gaussian beam (equation 3.41)
w_o	fundamental Gaussian beam waist radius (equation 3.41)
ξ	normalized z-coordinate (equation 3.42)
ξ_o	axial position of the fundamental Gaussian beam focus with respect to the center of the cesium distribution (equation 3.52)

CHAPTER 4

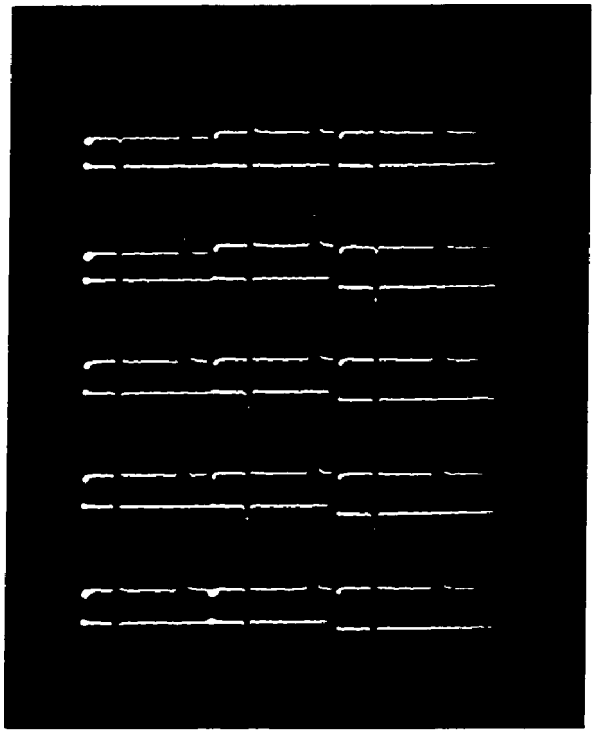
RESONANT THIRD-HARMONIC GENERATION IN CESIUM VAPOR

In Chapter 2, we have mentioned that the third-harmonic signal from cesium vapor was found strongly dependent on the ruby output wavelengths and beam optics, as well as the cesium vapor density distribution. The last two dependences have been demonstrated in Section 3.5. In this Chapter, we will describe the resonance aspect of experimental third-harmonic generation in cesium vapor. The correlation between third-harmonic generation and two-photon fluorescence in cesium will be given in Section 4.1. In Chapter 3, it was pointed out that in an isotropic nonlinear medium, the symmetry requirements reduce the third-harmonic tensor to only one independent element. Moreover, for a resonant process, the measured nonlinear coefficient involves an average over the fundamental spectrum and the velocity distribution of the microscopic systems. In Section 4.2, we shall make the determination of such a coefficient in atomic cesium vapor experimentally. In Section 4.3, the longitudinal multimode structure of the fundamental laser beam will be studied briefly. For a free atomic system like cesium vapor, the nonlinear coefficient in general can be calculated quantum mechanically. Such a calculation has been performed by Orr (see Appendix 1). In Section 4.4, we shall show how this quantum mechanical result for an isolated cesium atom

is to be averaged over the laser spectrum taking into account the velocity distribution of the cesium atom. Accordingly, we synthesize a theoretical result with relevant parameters for comparison with experiment.

4.1 Experiments on Resonant Third-Harmonic Generation and Correlated Two-Photon Absorption in Atomic Cesium Vapor

In this section, we wish to report the observed results of the first experiment on third-harmonic with resonant enhancement in atomic cesium vapor. The experimental setup has been explained in detail in Chapter 2. The ruby laser beam was focused into the center of the cesium cell and was tuned through a range of output wavelengths by regulating liquid nitrogen flow around the rod. The cesium vapor pressure in the cell was fixed at 0.1 Torr (or 210°C side arm temperature) while third-harmonic signal was readily observed in a range of ruby output wavelengths. The result is exhibiting as a resonance curve (cf Figure 19a). The peak value of the resonance curve is centered at about 14414.50 cm^{-1} (or 6935.55 Å) by comparison with a cadmium doublet. In order to understand the resonant processes in this system, it is necessary and advantageous to measure both third-harmonic and two-photon fluorescent signals simultaneously, using both the head-on and sideways detectors. Typical oscilloscope traces are shown in Figure 18. At a fixed ruby output wavelength, 15 shots were made. Each shot consists of three pulses with heights V_{THG}, V_{TPF}, and V_m (delayed by 800 nsec). These pulse heights are in turn proportional to the peak power at the third-harmonic wavelength ($P^{3\omega}$), at the fluorescent wavelength



500 nsec

3 x 5 = 15 shots, each shot consists of three pulses: for upper beam, two-photon fluorescent pulse and fundamental pulse (delayed 800 nsec); for lower beam, third-harmonic pulse.

Figure 18. Typical Oscilloscope Traces.

of 5847 $\mathring{A}$ ($\mathbb{P}^{\omega_f}$), and at the fundamental ($\mathbb{P}^{\omega}$), respectively. Hence, each laser pulse yielded a pair of correlated signals depending upon the ruby output wavelength of the laser beam.

A pair of correlated curves for resonant third-harmonic generation and two-photon fluorescence is shown in Figure 19. The vertical error flags reflect only the statistical fluctuation of the signals for a group of 15 shots at each ruby output frequency. It is obvious that there is resonance in each case. The arrow indicates the location of the $\frac{1}{2}\omega_{9D_{3/2}}$ (14414.45 cm^{-1}), while the horizontal error flag reflects an uncertainty ($\pm$ 0.05 cm^{-1}) in frequency calibration. It is noted that both curves peak at the same frequency which coincides with $\frac{1}{2}\omega_{9D_{3/2}}$ within experimental uncertainties. It is also noted that it is possible to draw a symmetric curve through the data points of two-photon fluorescence, but an asymmetric one must be drawn for third-harmonic generation case. We do not understand the cause of this asymmetry, but one may speculate that this may come from changes in laser beam mode structure with temperature. The width of the resonant third-harmonic curve is 0.30 cm^{-1}, while it is 0.20 cm^{-1} for the two-photon fluorescence curve. These widths are somewhat wider than that would be predicted from the Doppler width of the $9D_{3/2}$ level of the cesium atom and the laser linewidth.

Since the third-harmonic power is expected to vary as the cube of the fundamental power

$$\mathbb{P}^{3\omega} \propto (\mathbb{P}^{\omega})^3 \qquad (4.1)$$

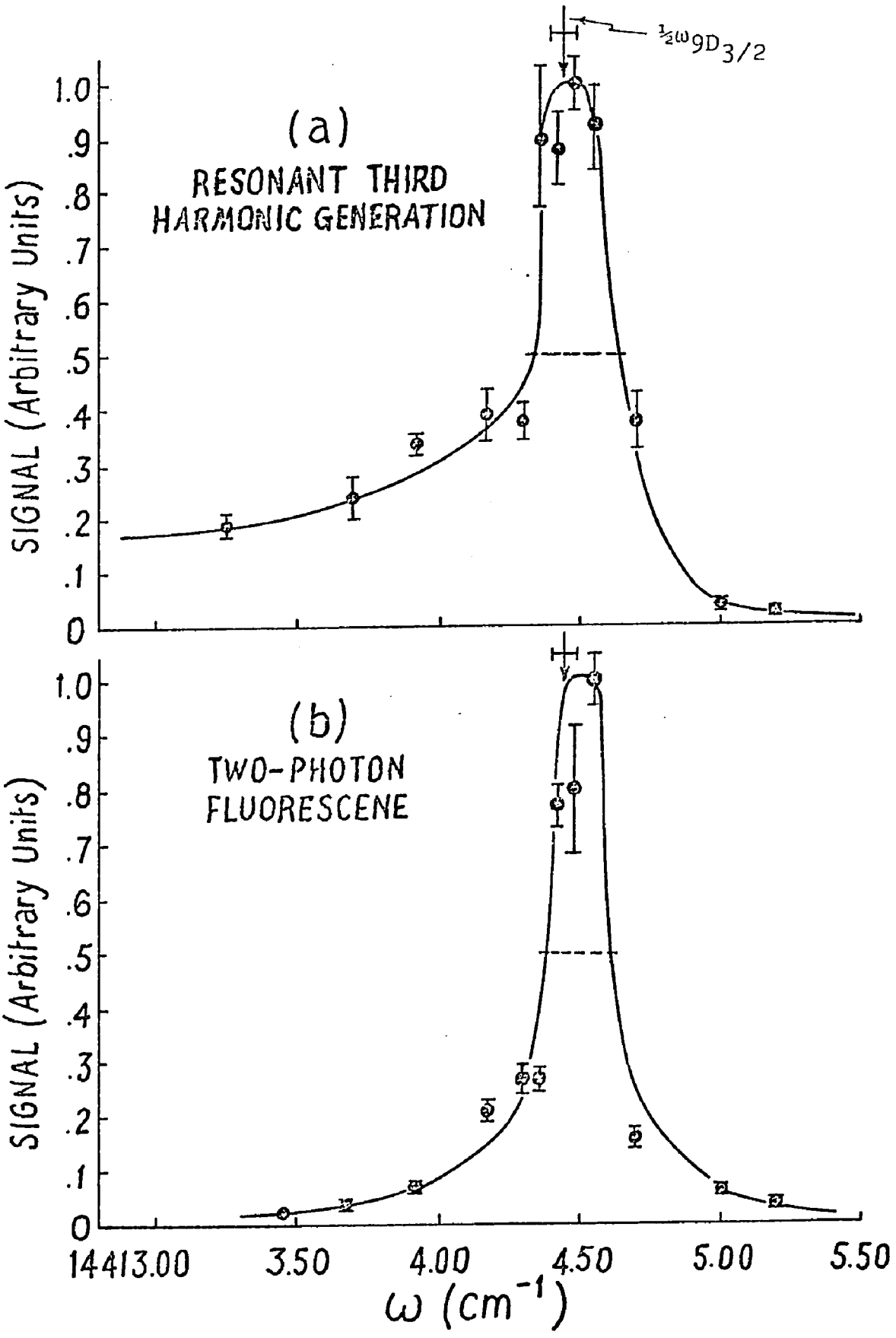


Figure 19. A Pair of Resonance Curves. The error flags reflect only the statistical fluctuation of the signal.

and the two-photon fluorescence power is proportional to the square of the fundamental power

$$\mathbb{P}^{\omega_f} \propto (\mathbb{P}^{\omega})^2 \qquad (4.2)$$

the square of the third-harmonic power is then expected to correlate to the cube of the two-photon fluorescence power by

$$(\mathbb{P}^{3\omega})^2 \propto (\mathbb{P}^{\omega_f})^3 \qquad (4.3)$$

Figure 20 depicts the corresponding results by the respective log-log plots of expressions 4.1, 4.2, and 4.3. The first two of these curves show some experimental evidences for slopes smaller than those predicted by equations 4.1 and 4.2. We believe this is due to an increase in laser linewidth and in beam area due to increasing beam divergence at higher power output. The relation of equation 4.3 is less dependent on laser linewidth and indeed a better agreement between experiment and theory is seen in this case (cf Figure 20(c)).

We have observed two different fluorescent signals at 5847 $\mathring{A}$ and 5666 $\mathring{A}$ from the sideways detector by using two different interference filters. The 5847 $\mathring{A}$ component, due to fluorescent decay of the $9D_{3/2}$ state to $6P_{3/2}$, was previously observed in detail by Abella. The 5666 $\mathring{A}$ component, corresponding to the fluorescent decay of the $9D_{3/2}$ state to $6P_{3/2}$, was measured to be five times bigger than the former component. A list of transition probabilities between $9D_{3/2}$ state and other subsequent states is tabulated in Table 3, which agrees

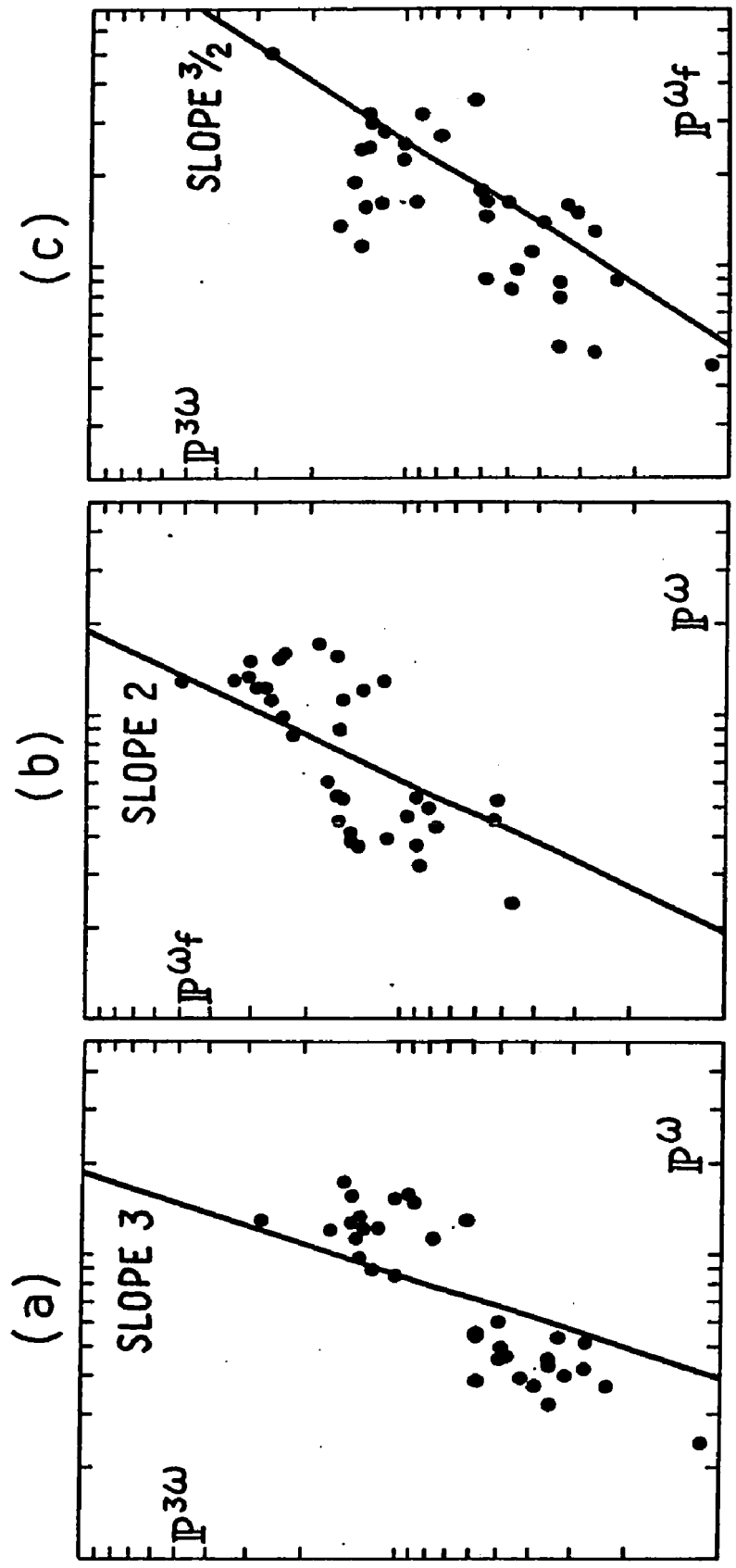


Figure 20. Simultaneous Power Outputs of $P^{3\omega}$ and P^{ω_f} with respect to Fundamental Power P^{ω} Plotted on Log-Log Scales for 35 Shots in a Given Experimental Situation

Table 3

TRANSITION PROBABILITIES OF CESIUM ATOM WITH $9D_{3/2}$ AS THE EXCITED STATE

Transition[a] (|m> - |n>)	$E_m - E_n$[b] (cm^{-1})	λ_{vac} (Å)	f_{mn}[c]	A_{mn} ($10^6 s^{-1}$)	Branching Ratio
$9D_{3/2} \rightarrow 6P_{1/2}$	17651	5666	0.0228	2.36	0.49
$6P_{3/2}$	17096	5847	0.0025	0.48	0.10
$7P_{1/2}$	7063	14160	0.0391	0.65	0.135
$7P_{3/2}$	6882	14500	0.0047	0.15	0.031
$4F_{5/2}$	4357	22900	0.0047	0.089	0.185
$8P_{1/2}$	3120	32000	0.09	0.29	0.060
$8P_{3/2}$	3037	32900	0.011	0.068	0.014
$5F_{5/2}$	2037	49100	0.035	0.12	0.025
$9P_{1/2}$	1192	83800	0.28	0.13	0.027
$9P_{3/2}$	1147	87100	0.35	0.30	0.062
$6F_{5/2}$	499	2.0×10^5	0.65	0.16	0.033
$10P_{1/2}$	102	9.8×10^5	0.70	0.0023	0.0005
$10P_{3/2}$	75	1.3×10^6	0.70	0.0023	0.0005

References for Table 3

(a) Subsequent transition from |n> state is not included here.

(b) C. E. Moore, Atomic Energy Levels, National Bureau of Standards Circular No. 467 (U. S. Government Printing Office, Washington, D. C., 1958).

(c) f-values are obtained from
(i) see Ref. (22)
(ii) E. M. Anderson and V. A. Zilitis, Opt. i Spektroskopiya 14, 382 (1963).

with the above result. Other fluorescent components on the list were not investigated because they were either too weak or outside the detecting range of the sideways detector. Another process closely related to these two-photon absorption in the form of stimulated emission was observed and will be discussed in Chapter 5.

4.2 Measurement of the Resonant Third-Harmonic Coefficient for Cesium

A direct measurement of the nonlinear coefficient involves data on $\mathbb{P}^{\omega}$ and $\mathbb{P}^{3\omega}$, study of mode structure of the laser beam, absolute value of beam area, transmission factor of optical components, and the efficiency of the head-on detector, which are all subject to large uncertainties. We can avoid some of these problems by the following procedure.

The absolute value of the average coefficient $\langle\chi_{Cs}\rangle$ is determined by comparing the experimental results of the third-harmonic generation in cesium vapor with that at a glass/air interface, and the use of a comparison of glass/air interface to glass/helium interface experiments[12] and a theoretical value for χ_{He}[19]. We emphasize that the observable quantity S is defined in terms of powers (cf equation 3.22) after the experiment but before any interface is passed. For the glass/air experiment of Ward and New, the signal can be expressed in terms of coefficients as

$$S_{GA} = \lambda\mu K_{GA} \left| n\frac{X}{\Delta k}\right|_{glass} - \frac{X}{\Delta k}\Big|_{air} \Big|^2 \qquad (4.4)$$

or in terms of the theoretical value for $(X/\Delta k)_{He}$:

$$S_{GA} = \lambda\mu K_{GA} R \left| \frac{X}{\Delta k} \right|_{He}^{2} \qquad (4.5)$$

where the factor η involves refractive indices of glass at the interface and is not relevant to our measurement here, λ is a factor representing the enhancement by lumpiness in energy distribution across the beam, i.e., the effect of multiple transverse modes, and μ is a factor (1 to 6) for the effect of multiple longitudinal modes. K_{GA} is a constant factor related to the beam radius w_I at the interface,

$$K_{GA} = \frac{2^6 \pi^2 k_o^2}{3c^2 w_I^4} \qquad (4.6)$$

R is a ratio of coefficients[12] written in the form

$$R = \left| \frac{1 - \left.\frac{X}{\Delta k}\right|_{air} \Big/ \eta \left.\frac{X}{\Delta k}\right|_{glass}}{\left.\frac{X}{\Delta k}\right|_{He} \Big/ \eta \left.\frac{X}{\Delta k}\right|_{glass}} \right|^2 = 1.72 \pm 0.65 \qquad (4.7)$$

For the cesium experiment, it is recalled that S_{Cs} is given by equation 3.39

$$S_{Cs} = \lambda K_{Cs} \sin^2(\Omega \tfrac{\pi}{2}) \left| \frac{X}{\Delta k} \right|_{Cs}^{2} \qquad (4.8)$$

where we have set K_{Cs} to be

$$K_{Cs} = \frac{2^8 \pi^2 k_o^2}{3c^2 w_o^4} \tag{4.9}$$

and add the transverse mode factor λ. The factor μ is included in $|(X/\Delta k)_{Cs}|$ since it has been specifically taken care of in the theoretical calculation (see Section 4.4). We have assumed equal enhancement by transverse mode structure for the two experiments. It is noted that areas of the beam for the two experiments measured in the same way (good to within a factor of 2) should give a ratio of areas better than an absolute area. Thus, by taking the ratio of equations 4.8 and 4.5, we obtain an expression for $|(X/\Delta k)_{Cs}|$:

$$\left|\left(\frac{X}{\Delta k}\right)_{Cs}\right| = \frac{\sqrt{\mu}}{2\sin(\Omega\frac{\pi}{2})}\left(\frac{w_o}{w_I}\right)^2\left(\frac{S_{Cs}}{S_{GA}}\right)^{\frac{1}{2}}\sqrt{R}\left|\left(\frac{X}{\Delta k}\right)_{He}\right| \tag{4.10}$$

A schematic for the two experimental setup is shown in Figure 21 with the emphasis on beam optics. The fundamental beam radius was varied in the range of 0.117 cm to 0.453 cm for four collimated beams in the cesium experiment, and set at 0.068 cm at the glass/air interface in that experiment. For the cesium experiment, the third-harmonic signal was detected with a fixed fundamental frequency of 14414.45 cm^{-1} (corresponding to the peak resonance of $9D_{3/2}$ level) and cesium side arm temperature at 230°C (or Ω=0.72) at equalibrium. For the glass/air interface experiment, a

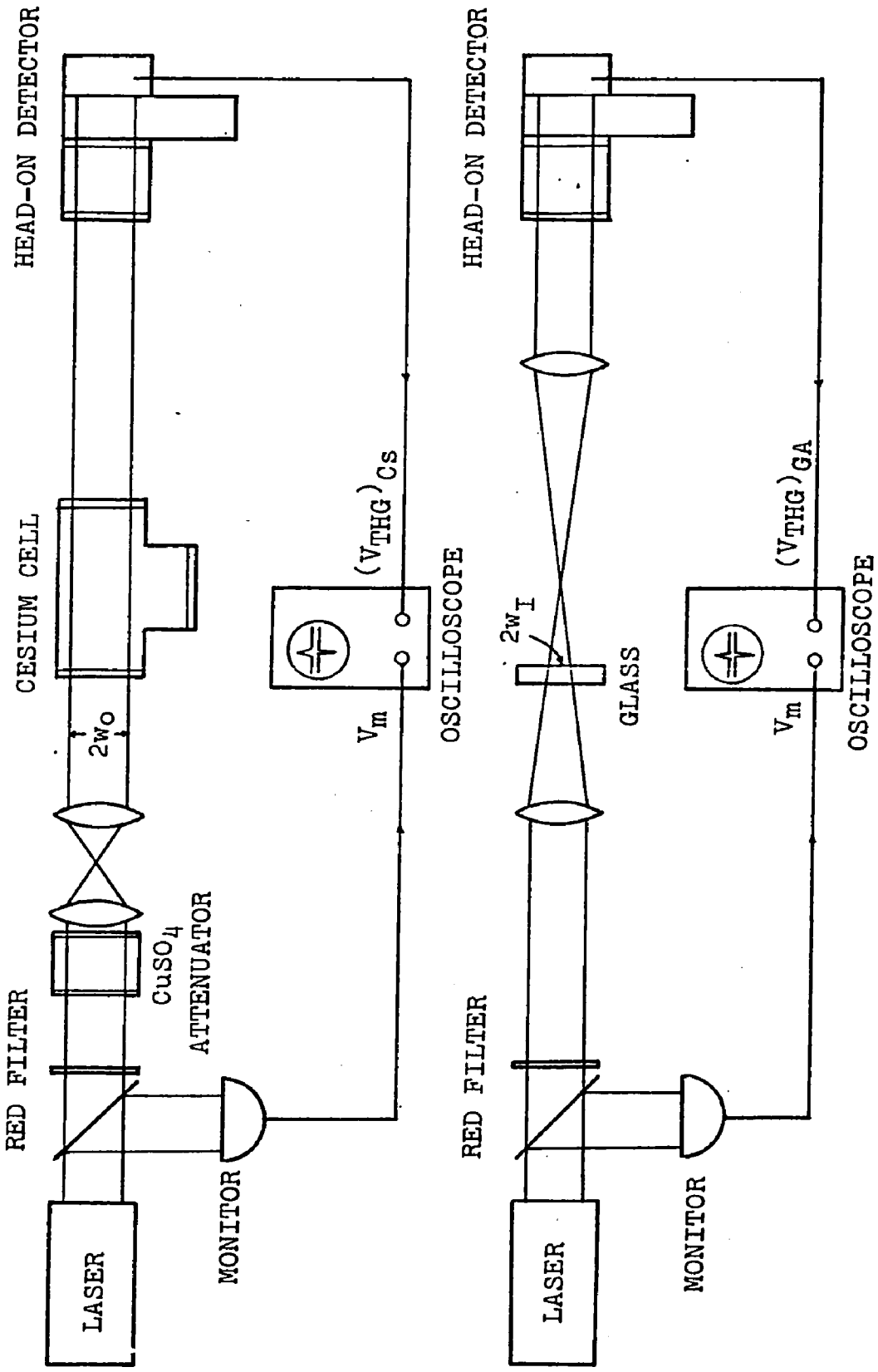


Figure 21. Schematic Diagram for Comparison of Two Experimental Setup

3 mm thickness Pyrex glass plate was placed about 5 cm in front of the focal position of the focused laser beam at the same output frequency. Using our multimode laser beam to obtain data from the two experiments with a Doppler width of $9D_{3/2}$ level, the absolute value of $\langle\chi_{Cs}\rangle$ was estimated to be $(1.0\pm0.47)\times10^{-30}$ esu/atom, where the deviation from the mean arises from four sets of data due to four collimated beams. However, uncertainties involved in the measurements of parameters must be considered in the determination of $\langle\chi_{Cs}\rangle$. The largest identifiable uncertainties are the statistical fluctuations in measuring the signals (±20%), the factor $\sqrt{R}$ derived from Ward and New's data on glass/air interface experiment (±20%), and the ratio of beam radius (±20%). The factor $\sqrt{\mu}$ is assigned to be 2±1 since μ increases to six if many confocal lowest-order modes are present. In addition, another significant source of error which was not shown explicitly in the measurements of the coefficient but produced the largest uncertainty of all. This arises from the combination of the birefringence of the sapphire windows of the cell and the polarization anisotropy of the monochromator of the head-on detector. We feel that there is 70% probability that $\langle\chi_{Cs}\rangle$ lies between 0.2×10^{-30} esu/atom and 5.0×10^{-30} esu/atom, or

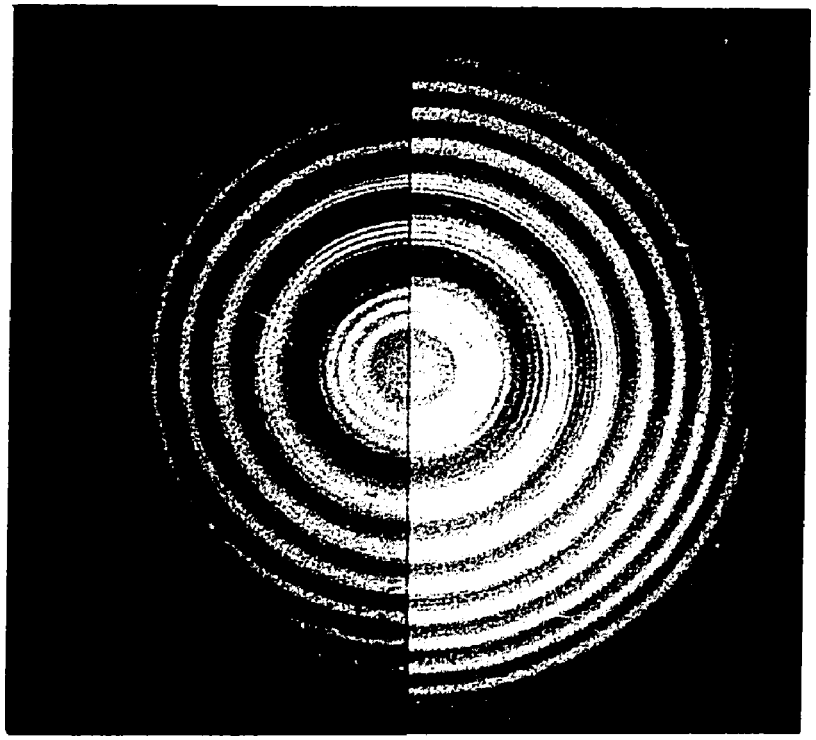
$$\langle\chi_{Cs}\rangle = (1.0\times10^{-30})\times5^{\pm1} \text{ esu/atom} \qquad (4.11)$$

for our multimode laser and Doppler broadening in the $9D_{3/2}$ level of cesium atom.

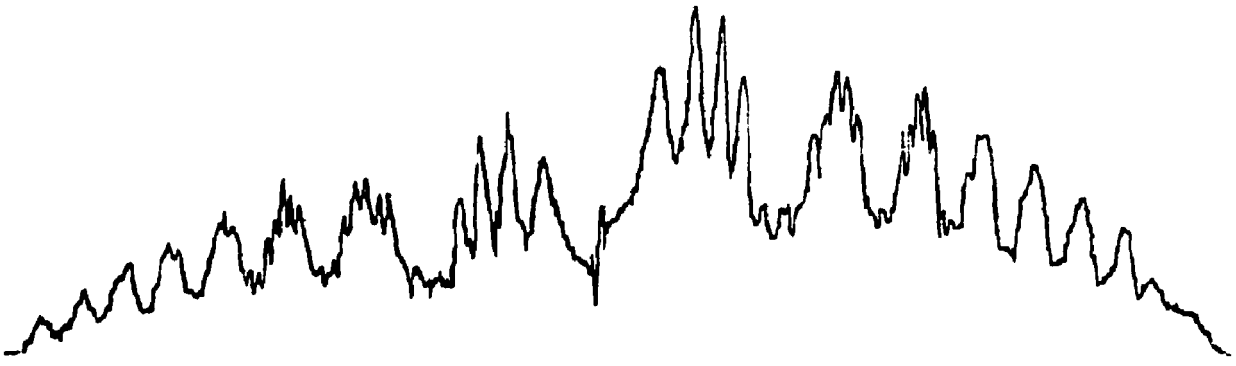
4.3 Longitudinal Multimode Structure of the Laser Beam

In order to synthesize a theoretical value of the nonlinear coefficient $\langle \chi_{Cs} \rangle$ taking into account the laser spectrum, a brief study of the laser linewidth and its multimode nature is necessary. It has already been shown in Section 2.1 that the wavelength of the ruby laser is strongly temperature dependent. We now examine the dependence of the linewidth and the longitudinal multimode structure on temperature by means of a plane Fabry-Perot etalon having a spacing of 25 mm and free spectral range of 0.20 cm^{-1}. This observation will then lead us to set up a model to perform an average over the laser spectrum in evaluating the nonlinear coefficient $\langle \chi_{Cs} \rangle$.

The interferogram of Figure 22 illustrates such dependence of multimode nature on ruby temperature. At 150°K the emission is in a group of 7 sharp lines (4 strong components and 3 weak ones) separated by approximately 0.025 cm^{-1}. Similar groups of several components were observed at various temperature down to 115°K. These results are displayed in Figure 23 schematically. Here it is seen that the dependence of linewidth and the number of longitudinal modes on temperature is obvious. The result of the multimode number dependence on the ruby output frequency is displayed in Figure 24. It is interesting to note that the observed cavity resonance spacing of this ruby laser corresponds to the length L of the ruby rod rather than the overall length of the optical cavity, i.e.,



(a) Emission in Several Longitudinal Modes with Ruby at 150°K



(b) Micro-densitometer Trace of the Same Interferogram

Figure 22. Interferogram of Ruby Laser Taken with a Plane Fabry-Perot Etalon Having a Spacing of 25 mm

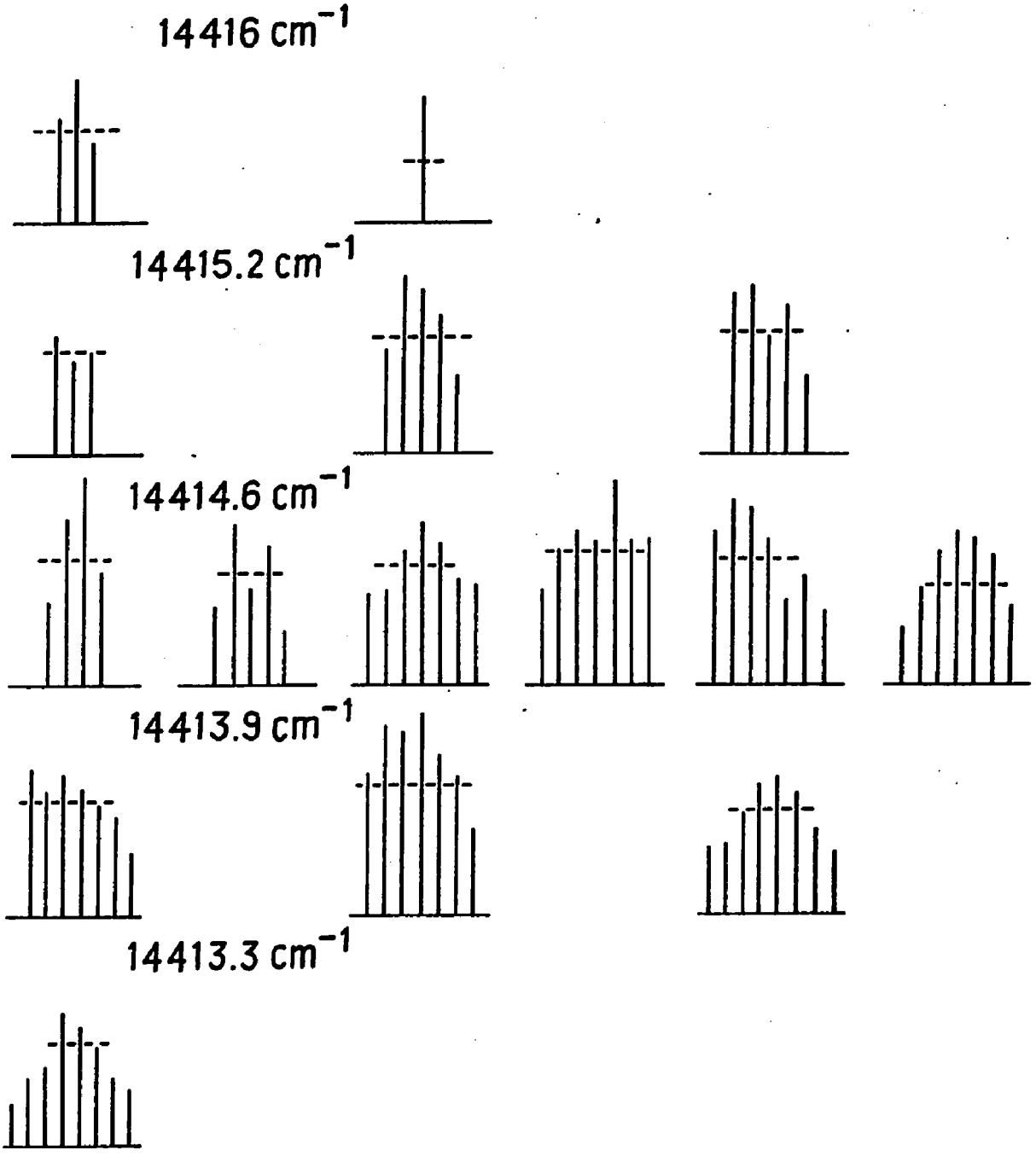


Figure 23. Schematics for Dependence of Linewidth and Mode Number of Our Ruby Laser on Ruby Output Frequency. Broken line represents linewidth (at half maximum) and vertical line represents relative intensity of individual mode separated by a mode spacing of about 0.025 cm^{-1}.

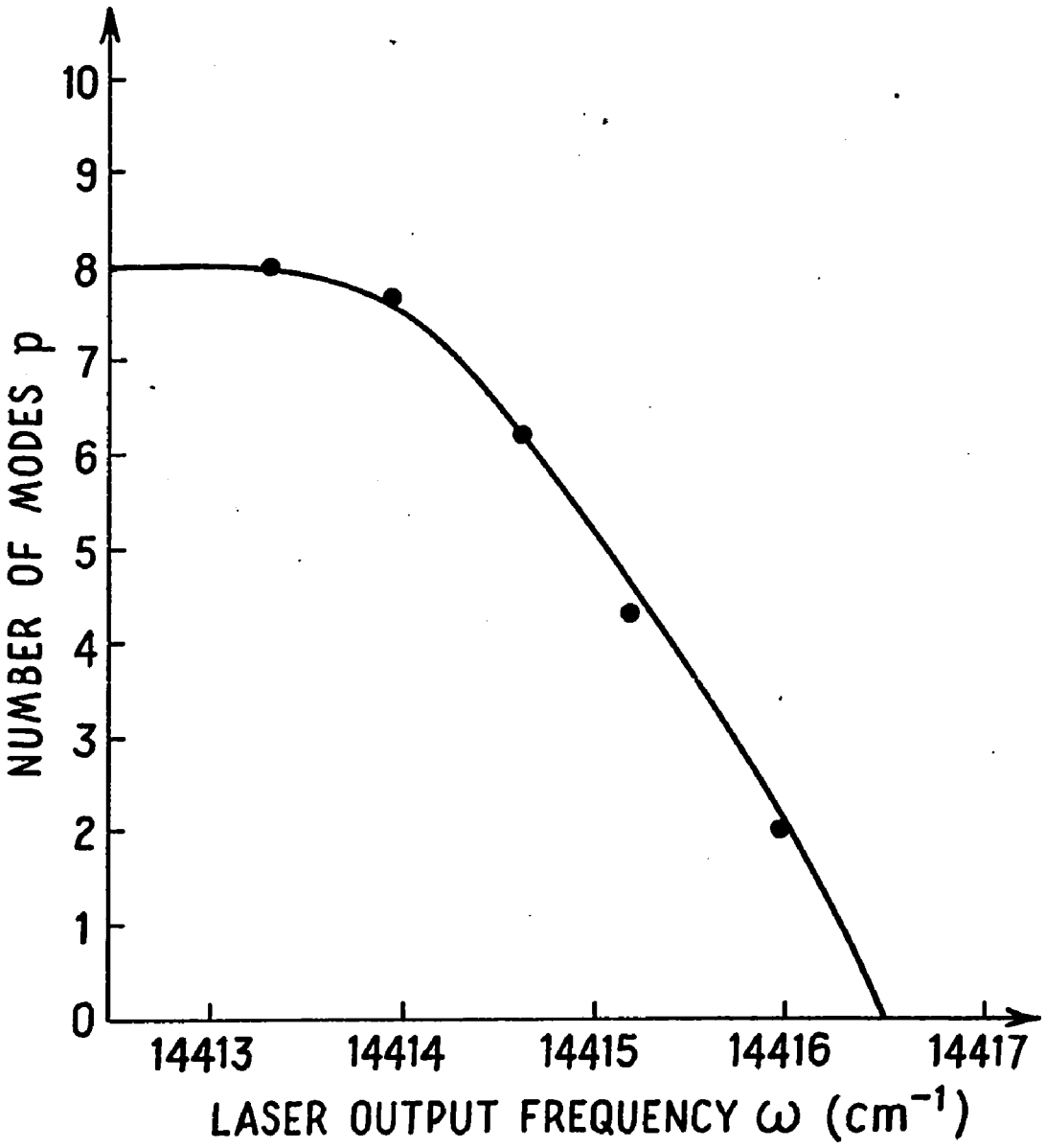


Figure 24. Number of Modes vs Ruby Laser Output Frequency

$$1/(2n_{ruby}L) = 0.025 \text{ cm}^{-1} \qquad (4.12)$$

We conclude that the linewidth of the laser spectrum is about 0.08 cm^{-1} at low temperature (corresponding to ruby output 14416.00 cm^{-1} or 6934 Å) and about 0.16 cm^{-1} at 40 K^{o} higher temperature (corresponding to ruby output 14413.00 cm^{-1} or 6936 Å) in the range of our resonance experiments. Figure 25 shows a schematic diagram to give an idealized situation for the longitudinal multimode nature of our laser beam, so that we are able to set up a model to perform the averaging problem over the laser spectrum. We assume in this model, that the laser power is equally divided between modes.

4.4 Theoretical Value of the Resonant Third-Harmonic Coefficient for Cesium

The nonlinear coefficient for resonant third-harmonic generation in cesium $\langle\chi_{Cs}\rangle$ unlike that of helium, is distinguished by the resonant effect due to the fact that the energy difference between the ground state and the $9D_{3/2}$ state is coincident with the energy of two ruby photons. The $9D_{5/2}$ level is outside the tuning range of the ruby laser and we consider only the contribution of the resonant effect due to $9D_{3/2} \leftarrow 6S_{1/2}$ in the evaluation of the nonlinear coefficient. In terms of Orr's calculated number, χ_o as given in Appendix 1, the coefficient is taken to be

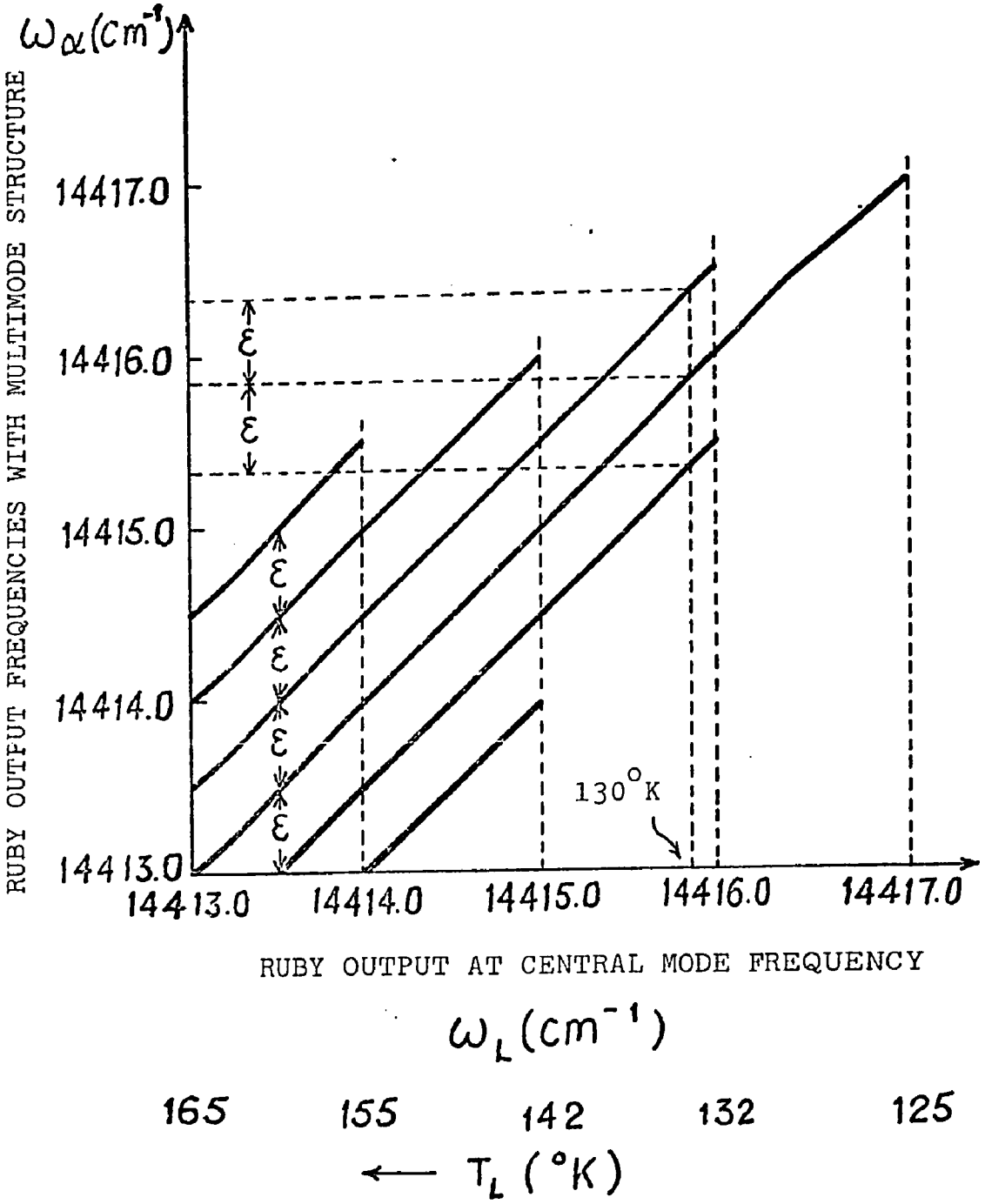


Figure 25. Idealized Situation of Longitudinal Multimode Structure of the Ruby Laser. (For clarity, the mode spacing ε is exaggerated here. An example is given to illustrate the usage of the graph at T_L = 130°K.)

$$\chi_{Cs} = \chi_o I_{1,2,3} \frac{\Gamma_{9D}/2}{\Omega_{9D}-\omega_1-\omega_2} \qquad (4.13)$$

where $I_{1,2,3}$ denotes the average of all possible terms generated by permuting ω_1, ω_2, ω_3 together with corresponding matrix elements. The natural frequency Ω_n (not to be confused with the number of coherence lengths, Ω) is allowed to be complex, i.e.,

$$\Omega_n = \omega_n - i\Gamma_n/2 \qquad (4.14)$$

with Γ_n as the inverse radiative lifetime of state $|n>$, and both Γ_n and ω_n are real. The natural width of the 9D doublet is evaluated to be 1.9×10^{-5} cm^{-1}.

It is noted that χ_o is real and that the maximum value of the nonlinear coefficient for an isolated cesium atom at rest and the case of monochromatic source is

$$\chi_{Cs} = i\chi_o = i\ (8.8\times10^{-27})\ \text{esu/atom} \qquad (4.15)$$

as compared to the helium case[20],

$$\chi_{He} = 4 \times 10^{-39}\ \text{esu/atom} \qquad (4.16)$$

which is 12 orders of magnitude smaller than that for the cesium atom.

It is evident from equations 4.13 and 4.14 that

χ (for convenience, we shall omit the subscript Cs in the following) is complex and we let

$$\chi = \chi' + i\chi'' \tag{4.17}$$

We recall that , in Chapter 3, the observable quantity S is proportional to the modulus squared of the coefficient,

$$S \propto |\langle\chi\rangle|^2 = \langle\chi'\rangle^2 + \langle\chi''\rangle^2 \tag{4.18}$$

Here, the notation < > is an appropriate average over velocity distribution and laser spectrum.

To average over velocity distribution, we consider the case of a single transverse mode laser at fundamental frequency ω and the process $\omega+\omega+\omega=3\omega$. The coefficient can then be written in the form

$$\chi(-3\omega;\omega,\omega,\omega) \equiv \chi(\omega) = \chi_o \frac{\Gamma_{9D}}{2}\left(\frac{1}{\Omega_{9D}-2\omega}\right) \tag{4.19}$$

Orr[15] also pointed out that the average coefficient in the laboratory frame of reference, accordingly is given by

$$\langle\chi(\omega)\rangle = \chi_o \frac{\Gamma_{9D}}{2} \left\langle \frac{1}{\Omega_{9D} - 2\omega} \right\rangle \tag{4.20}$$

or in detail

$$\langle\chi(\omega)\rangle = \chi_o \frac{\Gamma_{9D}}{2}$$

$$2\sqrt{\frac{\ell n 2}{\pi}}\,\Delta^{-1}\int_{-\infty}^{\infty} d(\omega'-\omega)\left(\frac{1}{\Omega_{9D}-2\omega}\right)e^{-4\ell n 2\left(\frac{\omega'-\omega}{\Delta}\right)^2} \qquad (4.21)$$

where ω' is a Doppler-shifted frequency (dummy label) and Δ is the Doppler width of the $9D_{3/2}$ level given by

$$\Delta = 2\omega\sqrt{\frac{kT}{mc^2}2\ell n 2} = 7.16 \times 10^{-7}\,\omega\sqrt{\frac{T}{M_{Cs}}} \qquad (4.22)$$

For cesium vapor at $T = 483^{o}K$ and $\omega = 28828.90\ cm^{-1}$, the Doppler width is evaluated to be $0.04\ cm^{-1}$. The integral of equation 4.21 can be expressed analytically in terms of the well known "Plasma Dispersion Function", which has been tabulated[20]. A general form of this function is

$$Z(x,y) = \pi^{-\frac{1}{2}} \int_{-\infty}^{\infty} dt\,\frac{e^{-t^2}}{t-x-iy} \qquad (4.23)$$

If we now let

$$\delta = \Delta/2\sqrt{\ell n 2} = 0.025\ cm^{-1}$$
$$x = (2\omega - \omega_{9D})/\delta \qquad (4.24)$$
$$y = \Gamma_{9D}/2\delta$$

Equation 4.21 can be re-written as

$$\langle\chi(\omega)\rangle = \chi_o \frac{\Gamma_{9D}}{2}\delta^{-1}\{Z(x,y)\} \qquad (4.25)$$

Since $y \sim 10^{-4} << 1$ in this case, we obtain the asymtotic value of $Z(x,y)$ as $y \to 0$ from the tabulated data. The result of this Doppler averaging is displayed in Figure 26 together with a graphical illustration of equation 4.19. The peak value of $|\langle\chi(\omega)\rangle|$ for the case of a single mode laser with a Doppler width of 0.04 cm^{-1} is evaluated to be

$$|\langle\chi\rangle| = 5.9 \times 10^{-30} \text{ esu/atom} \qquad (4.26)$$

We next consider ruby output with three modes, and assume equal power in each mode (see Figure 27 and compare with Figure 25). We note that the dependence of number of modes on temperature can be taken into account after the averaging process simply by examining the results as a whole. Figure 27 and Table 4 display the situation in greater detail to clarify such a process quantitatively. The three different fundamental frequencies corresponding to three modes of the laser spectrum are set to be ω, and $\omega \pm \varepsilon$, where ε is the mode separation. Ten different nonlinear third-order processes due to the mixing of these modes are listed in Table 4. The observable quantity S is now written in the form

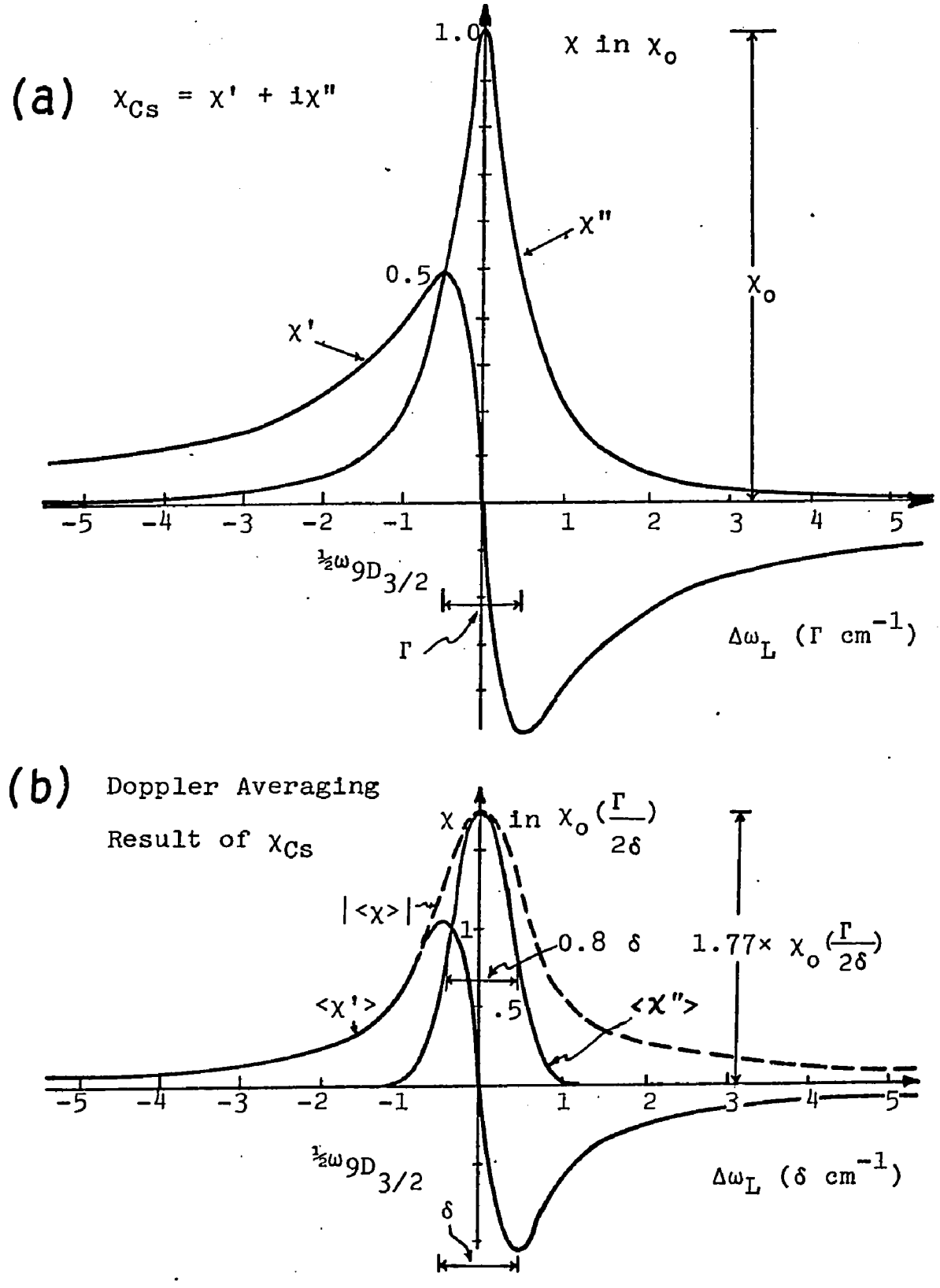


Figure 26. Doppler Averaging of χ_{Cs} for Single Mode Case

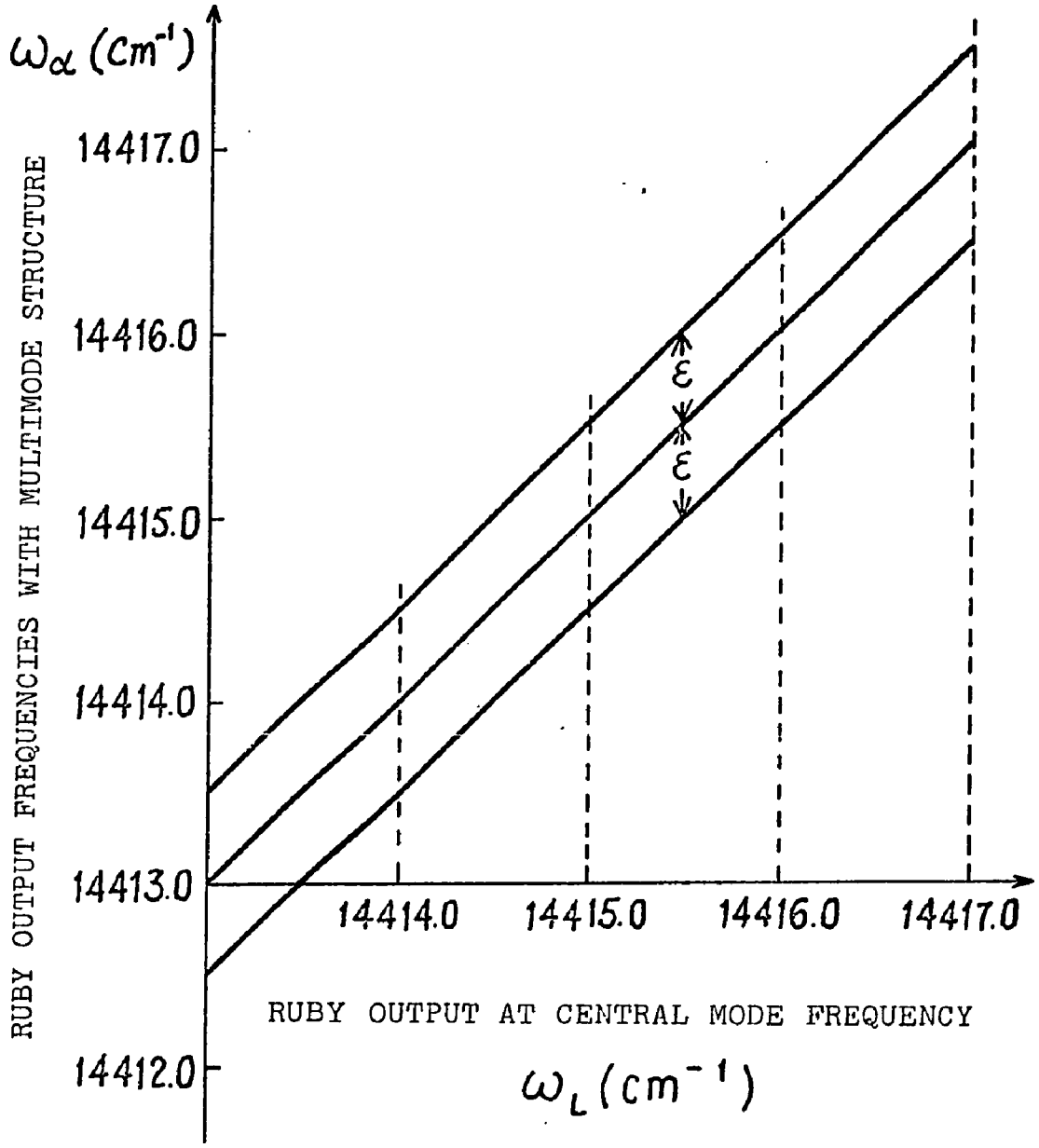


Figure 27. Model of Three Modes Case for Averaging Process

Table 4. BEATING OF THREE MODES

σ	Beating $\omega_1 + \omega_2 + \omega_3 = \omega_\sigma$	Resonances $(\omega_1)(\omega_2),(\omega_2)(\omega_3),(\omega_3)(\omega_1)$	K	Resonance peaking at frequency of (with weighting factor included constant K) $2\omega-2\varepsilon$	$2\omega-\varepsilon$	2ω	$2\omega+\varepsilon$	$2\omega+2\varepsilon$
1	$(\omega)+(\omega)+(\omega)=3\omega$	$(\omega)(\omega),(\omega)(\omega),(\omega)(\omega)$	$\frac{1}{4}$			$\frac{1}{4}$		
2	$(\omega+\varepsilon)+(\omega+\varepsilon)+(\omega+\varepsilon)=3\omega+\varepsilon$	$(\omega+\varepsilon)(\omega+\varepsilon),(\omega+\varepsilon)(\omega+\varepsilon),(\omega+\varepsilon)(\omega+\varepsilon)$	$\frac{1}{4}$					$\frac{1}{4}$
3	$(\omega-\varepsilon)+(\omega-\varepsilon)+(\omega-\varepsilon)=3\omega-\varepsilon$	$(\omega-\varepsilon)(\omega-\varepsilon),(\omega-\varepsilon)(\omega-\varepsilon),(\omega-\varepsilon)(\omega-\varepsilon)$	$\frac{1}{4}$	$\frac{1}{4}$				
4	$(\omega-\varepsilon)+(\omega)+(\omega+\varepsilon)=3\omega$	$(\omega-\varepsilon)(\omega),(\omega)(\omega+\varepsilon),(\omega+\varepsilon)(\omega-\varepsilon)$	$\frac{3}{2}$		$\frac{1}{2}$	$\frac{1}{2}$	$\frac{1}{2}$	
5	$(\omega-\varepsilon)+(\omega-\varepsilon)+(\omega)=3\omega-2\varepsilon$	$(\omega-\varepsilon)(\omega-\varepsilon),(\omega-\varepsilon)(\omega),(\omega)(\omega-\varepsilon)$	$\frac{3}{4}$	$\frac{1}{4}$	$\frac{1}{2}$			
6	$(\omega-\varepsilon)+(\omega-\varepsilon)+(\omega+\varepsilon)=3\omega-\varepsilon$	$(\omega-\varepsilon)(\omega-\varepsilon),(\omega-\varepsilon)(\omega+\varepsilon),(\omega+\varepsilon)(\omega-\varepsilon)$	$\frac{3}{4}$	$\frac{1}{4}$		$\frac{1}{2}$		
7	$(\omega)+(\omega)+(\omega-\varepsilon)=3\omega-\varepsilon$	$(\omega)(\omega),(\omega)(\omega-\varepsilon),(\omega-\varepsilon)(\omega)$	$\frac{3}{4}$		$\frac{1}{2}$	$\frac{1}{4}$		
8	$(\omega)+(\omega)+(\omega+\varepsilon)=3\omega+\varepsilon$	$(\omega)(\omega),(\omega)(\omega+\varepsilon),(\omega+\varepsilon)(\omega)$	$\frac{3}{4}$			$\frac{1}{4}$	$\frac{1}{2}$	
9	$(\omega+\varepsilon)+(\omega+\varepsilon)+(\omega-\varepsilon)=3\omega+\varepsilon$	$(\omega+\varepsilon)(\omega+\varepsilon),(\omega+\varepsilon)(\omega-\varepsilon),(\omega-\varepsilon)(\omega+\varepsilon)$	$\frac{3}{4}$			$\frac{1}{2}$		$\frac{1}{4}$
10	$(\omega+\varepsilon)+(\omega+\varepsilon)+(\omega)=3\omega+2\varepsilon$	$(\omega+\varepsilon)(\omega+\varepsilon),(\omega+\varepsilon)(\omega),(\omega)(\omega+\varepsilon)$	$\frac{3}{4}$				$\frac{1}{2}$	$\frac{1}{4}$

$$S \equiv \frac{\sum_{\text{process 1}}^{10} P^{\omega_\sigma}}{\sum_{\text{mode 1}}^{3} P^{\omega_\alpha}_{3}} \qquad (4.27)$$

where σ and α are just labels corresponding to various third-order processes and modes respectively. The resulting harmonic power is the sum of contributions from all ten processes.

Three quantitative features are to be noted in this averaging process. We first assume lack of phase coherence between modes, so that for example, one must add the harmonic powers for processes (1) and (4) (see Table 4) rather than the harmonic fields. Secondly, in process (4), permutations of ω_1, ω_2, and ω_3 corresponding to other processes similar to $\omega_1 + \omega_2 + \omega_3 = \omega_\sigma$, are not listed since we have included a weighting factor for each process by putting a constant K on both sides of equation 4.13 and then do the average, i.e.,

$$K(-\omega_\sigma;\omega_1,\omega_2,\omega_3)\langle\chi(\omega)\rangle = \chi_o(\Gamma_{9D}/2\delta)$$

$$K(-\omega_\sigma;\omega_1,\omega_2,\omega_3)I_{1,2,3}\{Z(x,y)\} \qquad (4.28)$$

where $K(-\omega_\sigma;\omega_1,\omega_2,\omega_3)$ is a numerical factor defined by[14]

$$K(-\omega_\sigma;\omega_1,\omega_2,\omega_3) = 2^m \times D \qquad (4.29)$$

with m as (the number of non-zero polarization frequencies) minus (the number of non-zero field frequency labels in the set ω_1,ω_2, ...) and D is the number of distinguishable arrangements of the set of field frequency labels where $+\omega$ and $-\omega$ are distinguishable except when $\omega = 0$. Thirdly, within each process, three pairs of fundamental frequencies $(\omega_1)(\omega_2)$, $(\omega_2)(\omega_3)$, and $(\omega_3)(\omega_1)$ will yield three resonances close to $\omega_{9D3/2}$ corresponding to three sets of curves with each similar to those solid curves for the single mode case shown in Figure 26(b). For example, within process (9) of Table 4, two sets of resonance curves centered at 2ω and one at $(2\omega + 2\varepsilon)$ are yielded by mixing the three modes. We then sum over all three contributions within each process and evaluate the modulus squared of the sum. Thus, the modulus squared of the resonant third-harmonic coefficient is obtained by summing over the contributions from all ten processes. This averaging process over the multimode nature of the laser beam can be summarized in the following notation for arbitrary number of modes:

$$|\langle\chi\rangle_\sigma|^2 = \left(\frac{K}{3}\sum_{\gamma=1}^{3}\langle\chi'\rangle_{\sigma\gamma}\right)^2 + \left(\frac{K}{3}\sum_{\gamma=1}^{3}\langle\chi''\rangle_{\sigma\gamma}\right)^2 \qquad (4.30)$$

$$|\langle\chi\rangle|^2 = \sum_{\sigma=1}^{\nu}|\langle\chi\rangle_\sigma|^2 \qquad (4.31)$$

with

$$\nu = p + {}_pC_3 + p(p-1) \qquad (4.32)$$

where γ is a label corresponding to resonances peaking at various frequencies; ν is the total number of third-order process due to various mode beating; p is the number of modes and ${}_pC_3$ is the number of combinations of p different modes taken three at a time.

These summing processes are performed by means of computer calculation using the Doppler average result for the single mode case as the input data for each set of curves. We have performed the averaging process for cases of 3, 5, and 7 modes of which the results are displayed in Figure 28. It is noted that the profiles of the resonance curves are similar in shape, and the area enclosed by each curve is the same except in the single mode case. A dotted curve is drawn in Figure 28 to represent the predicted resonance curve taking into account the mode number dependence on ruby output frequency and the Doppler broadening of $9D_{3/2}$ level in cesium atom. It is noted that the linewidth of this theoretical curve is about three times smaller than the experimental width. However, other inhomogeneous broadening effects such as collision between cesium-cesium or cesium-neon have not been taken into account in the above averaging processes. We then synthesize that the theoretical curve should be flatten out by a factor of three but keeping

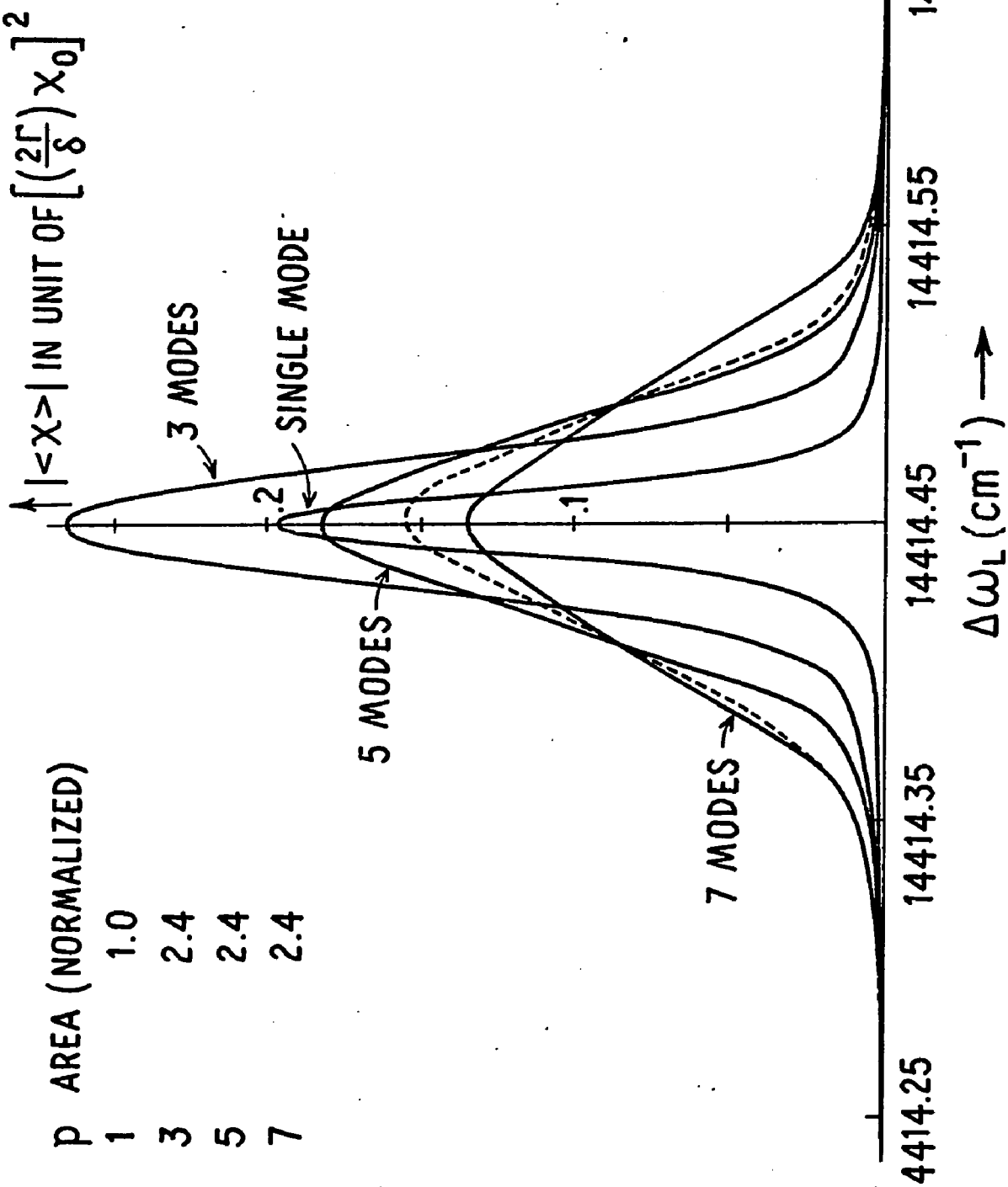


Figure 28. Results of Averaging on Doppler Width for Longitudinal Multimode Case

the same enclosed area. The final result of the peak value of the resonant third-harmonic coefficient near $9D_{3/2} \leftarrow 6S_{1/2}$ resonance is determined to be

$$|\langle\chi\rangle| = 2.8 \times 10^{-30} \text{ esu/atom} \qquad (4.33)$$

with considerations on effects of Doppler broadening of $9D_{3/2}$ level, finite linewidth and longitudinal multimode nature of our laser beam, as well as inhomogeneous broadening due to cesium-cesium and cesium-neon collisions in the cell.

Table 5 gives a summary of various values derived from theory and experiment together with that for helium. It is noted that these third-harmonic coefficients in cesium vapor is about 9 orders of magnitude greater than that in helium. This is essentially due to the resonant enhancement in the cesium atom. The coefficient derived from the Doppler averaging for a single mode laser beam is about three orders of magnitude smaller than χ_o which corresponds to the ratio of the natural width of the $9D_{3/2}$ level and the Doppler width of the $9D_{3/2}$ level in cesium atom. The finite linewidth and the multimode nature of our laser beam do not affect the value of the coefficient too much since the interference of mode beating cancels the broadening effect due to an increasing laser linewidth. The experimental value is smaller than the theoretical value from multimode averaging by a factor of 3. However, this experimental value bears a large uncertainty ($\times 5^{\pm 1}$) mainly due to the birefringence of the

sapphire windows and the polarization anisotropy of the monochromator, as well as the multimode structure factor μ. Thus, we believe that there is very satisfactory agreement between theory and experiment.

Table 5

SUMMARY OF THIRD-HARMONIC COEFFICIENTS

	$\langle\chi\rangle$(esu/atom)	Remarks
He	4.0×10^{-39} [a]	Quantum mechanical calculation is thought to be good to 1%
Cs	8.8×10^{-27} [b]	Quantum mechanical calculation for an isolated atom at rest
Cs	5.9×10^{-30}	After Doppler averaging for single mode case
Cs	2.8×10^{-30}	After Doppler averaging for longitudinal multimode case
Cs	$(1.0 \times 5^{\pm 1}) \times 10^{-30}$	Experimental value

References for Table 5

a) Ref. 19.

b) See Appendix 1.

CHAPTER 5

FOUR-PHOTON PARAMETRIC AMPLIFICATION IN CESIUM VAPOR

In this chapter, we report another resonant process closely related to the two-photon absorption which was observed in cesium vapor. This process could be described as doubly resonant, four-photon, parametric amplification or a stimulated analog of the two-photon fluorescence. In general, this effect occurs when two identical strong pump waves at frequency $2\omega_p = \omega_s + \omega_I$, where ω_s is the signal frequency and ω_I is the idler frequency. It is doubly resonant because not only is the energy difference between the ground state and the $9D_{3/2}$ state coincident with the energy of two fundamental pump photons ($2\hbar\omega_p$), but, in addition, the energy difference between the ground state and one of the excited P states is close to the energy of a signal photon ($\hbar\omega_s$). In the subsequent sections, only a preliminary study of this process will be given, although two interesting features were seen in this process experimentally. The experimental results indicated that about 10^{-8} conversion efficiency and 20 mW of blue light were estimated. Furthermore, there was no sign of limit to this signal output power experimentally. In Section 5.1, we shall set up the basic equations describing the parametric interactions and find an expression to describe the growth of the signal and idler waves. In Section 5.2, the experimental result of observing this effect

will be presented and a value for the gain coefficient for this process will be determined experimentally using the result of the analysis. Then, in Section 5.3, we make an estimate of this gain coefficient using quantum mechanical expression and results of the Doppler averaging for the single mode case obtained in the last chapter, to compare with the experimental value.

5.1 Exponential Gain of the Signal Wave

Standard derivation of the basic equations to describe the parametric amplification can be found in literature[21]. Here, we assume that the cesium vapor is transparent at ω_s, ω_I, and ω_p. The frequencies of the signal, idler, and pump are related by $2\omega_p-\omega_s = \omega_I$ or $2\omega_p-\omega_I = \omega_s$. We shall further assume that the four waves are phased matched, i.e.,

$$k_s + k_I - 2k_p \equiv \Delta k = 0 \qquad (5.1)$$

The corresponding electric fields are taken to be plane waves, i.e., taking $\partial/\partial x = \partial/\partial y = 0$ and propagating along z direction:

$$E^{\omega_s}(z,t) = \frac{1}{2}\left[E_s(z)e^{i(\omega_s t-k_s z)} + c.c.\right]$$

$$E^{\omega_I}(z,t) = \frac{1}{2}\left[E_I(z)e^{i(\omega_I t-k_I z)} + c.c.\right] \qquad (5.2)$$

$$E^{\omega_p}(z,t) = \frac{1}{2}\left[E_p(z)e^{i(\omega_p t-k_p z)} + c.c.\right]$$

Each field is determined by the inhomogeneous wave equation

$$\underline{\nabla} \times \underline{\nabla} \times \underline{E}^{\omega_i} - (k_i)^2 \underline{E}^{\omega_i} = 4\pi k_o^2 \underline{P}^{\omega_i} \qquad (5.3)$$

For example, the wave equation for $E^{\omega_s}(z,t)$ can be written as

$$[\frac{k_s^2}{2} E^{\omega_s} + ik_s \frac{dE^{\omega_s}}{dz}] e^{i(\omega_s t - k_s z)} + c.c. =$$

$$4\pi k_o^2 P^{\omega_s} + \frac{1}{2} k_s^2 [E^{\omega_s} + c.c.] \qquad (5.4)$$

where

$$P^{\omega_s}(z,t) = \frac{1}{2} [P^{\omega_s}(z) e^{i(\omega_s t - k_s z)} + c.c.] \qquad (5.5)$$

or in terms of electric fields,

$$P^{\omega_s}(z,t) = \frac{1}{2} K_s(-\omega_s;\omega_p,\omega_p,-\omega_I)\ X_s(-\omega_s;\omega_p,\omega_p,-\omega_I)$$

$$E_p E_p E_I^* e^{i(\omega_p+\omega_p-\omega_I)t} + c.c. \qquad (5.6)$$

We have assumed that the variation of the complex field amplitudes with respect to z is small enough so that

$$k_s \frac{dE_s}{dz} >> \frac{d^2E_s}{dz^2} \tag{5.7}$$

After substituting equation 5.7 into the wave equation 5.4, and some manipulation of algebra, we obtain a equation for E_s:

$$\frac{dE_s}{dz} = -2\pi i \frac{\omega_s}{n_s c} K_s(-\omega_s;\omega_p,\omega_p,-\omega_I)$$

$$X_s(-\omega_s;\omega_p,\omega_p,-\omega_I)E_p\ E_p\ E_I^* \tag{5.8}$$

and similarly equations for E_I and E_p:

$$\frac{dE_I}{dz} = -2\pi i \frac{\omega_I}{n_I c} K_I(-\omega_I;\omega_p,\omega_p,-\omega_s)$$

$$X_I(-\omega_I;\omega_p,\omega_p,-\omega_s)E_p\ E_p\ E_s^* \tag{5.9}$$

$$\frac{dE_p}{dz} = 0 \tag{5.10}$$

Equations 5.8 and 5.9 can be re-written in convenient forms:

$$\frac{dE_s}{dz} = -i\frac{G_s}{2} E_I^* \tag{5.11}$$

$$\frac{dE_I^*}{dz} = +i\frac{G_I^*}{2}E_s \tag{5.12}$$

where we have introduced two similar factors referred to as gain factors,

$$G_s = 4\pi\frac{\omega_s}{n_s c}K_s(-\omega_s;\omega_p,\omega_p,-\omega_I)E_p E_p N_{Cs}\chi_s(-\omega_s;\omega_p,\omega_p,-\omega_I)$$

$$G_I^* = 4\pi\frac{\omega_I}{n_I c}K_I(-\omega_I;\omega_p,\omega_p,-\omega_s)E_p^* E_p^* N_{Cs}\chi_I^*(-\omega_I;\omega_p,\omega_p,-\omega_s) \tag{5.13}$$

The solutions of the coupled wave equations subject to the initial conditions of $E_s(z=0) = E_{so}$ and $E_I(z=0) = 0$ are

$$E_s(z) = E_{so}\cosh(\frac{\sqrt{G_s G_I^*}}{2}z)$$

$$E_I(z) = -iE_{so}\sinh(\frac{\sqrt{G_s G_I^*}}{2}z) \tag{5.14}$$

We make a note at this point that since our experimental observation of the signal wave indicates an exponential growth, we then assume the gain factor is real and positive. Hence, the power for the signal wave is

$$P^{\omega_S} \propto |E_S(z)|^2 = \frac{1}{4} |E_{SO}|^2 e^{gz} \qquad (5.15)$$

where we have introduced a gain coefficient g defined as

$$g \equiv \sqrt{G_S G_I^*} = \frac{4\pi}{c} \sqrt{\omega_S \omega_I}\, K\, E_p^2 \mathrm{Re}(\chi_S \chi_I^*)^{\frac{1}{2}} \qquad (5.16)$$

where we have taken the real component of $\sqrt{G_S G_I^*}$, and set refractive indices $n_S=n_I=1$ and the constant factor $K_S=K_I=K$ which is equal to 3/4. Equations 5.15 and 5.16 describe the growth of the signal wave under phase-matched condition in a lossless medium.

5.2 Experimental

The experimental setup for observing the four-photon parametric amplification was the same as described in Chapters 2 and 4. However, the cesium vapor pressure was set at a higher value than in the case of the resonant third-harmonic generation. Table 6 lists 10 P sublevels, lower in energy than the $9D_{3/2}$ state and the corresponding frequencies of transitions to ground state which correspond to possible signal frequencies (cf Figure 2.b). We have observed two strong signals at 3500 Å and 4500 Å respectively.

In order to recognize these signals as being genuine four-photon parametric amplification, we carried out

Table 6

EXPECTED SIGNAL WAVES

Transition ($nP \rightarrow 6S_{\frac{1}{2}}$)	ω_s [a] (cm^{-1})	λ_s (Å)	Relative Gain [b] (Arbitrary unit)
$10P_{1/2}$	28727.09	3481	0.26
$10P_{3/2}$	28753.93	3477	1.80
$9P_{1/2}$	27637.29	3618	0.26
$9P_{3/2}$	27681.96	3612	1.76
$8P_{1/2}$	25709.14	3890	0.31
$8P_{3/2}$	25791.78	3877	0.52
$7P_{1/2}$	21765.65	4594	0.63
$7P_{3/2}$	21946.66	4556	0.75
$6P_{1/2}$	11178.24	8943	5.74
$6P_{3/2}$	11732.35	8521	3.64

References for Table 6

a) C. E. Moore, Atomic Energy Levels, National Bureau of Standards Circular No.467 (U. S. Government Printing Office, Washington D. C., 1958).

b) Relative gain of signal waves are listed for comparison and they were calculated using an expression derived from equations 5.16, 5.20 and 5.21:

$$\text{Relative Gain} = \sqrt{\omega_s \omega_I}\ \langle g|z|nPj\rangle\langle nPj|z|9D_{\frac{3}{2}}\rangle$$

where g is the ground state of cesium atom and n is the principal quantum number (6 to 10).

the following procedure. First, the cesium vapor was set at a side arm temperature of 250°C (corresponding to $\Omega = 2.0$ at third-harmonic generation, see Figure 13) such that no third-harmonic signal was detected (two coherence lengths, see Figure 14), but other signals were observed at near 3500 Å and 4500 Å using the head-on detector. In addition, blue (and near uv) light was observed with the naked eye on a piece of fluorescent material while the signals and the blue light disappeared if the cell was cooled down to room temperature . The power output of this signal was estimated to be about 20 mW at 3500 Å. We further set up the simultaneous measurements of the head-on detector signal and the sideways detector signal. Only one particular component of the possible spectrum was chosen to study in this case, namely, at 3500 Å. An interference filter centered at 3470 ± 35 Å was inserted in the sideways detector. The laser beam was focused into the center of the cesium cell and data was obtained while varying the cesium side arm temperature. Figure 29 depicts the results in which the ordinate is the ratio of the two pulse heights V_s and V_f corresponding to the head-on detector signal and the sideways detector signal respectively, and the abscissa is the product of the maximum cesium density at a particular cesium side arm temperature and the fundamental (pump) pulse height from the monitor, i.e., $N_{Cs}V_p$. A qualitative feature was seen that the head-on detector signal had increasing output as the cesium density was increasing. Also, at a particular cesium density,

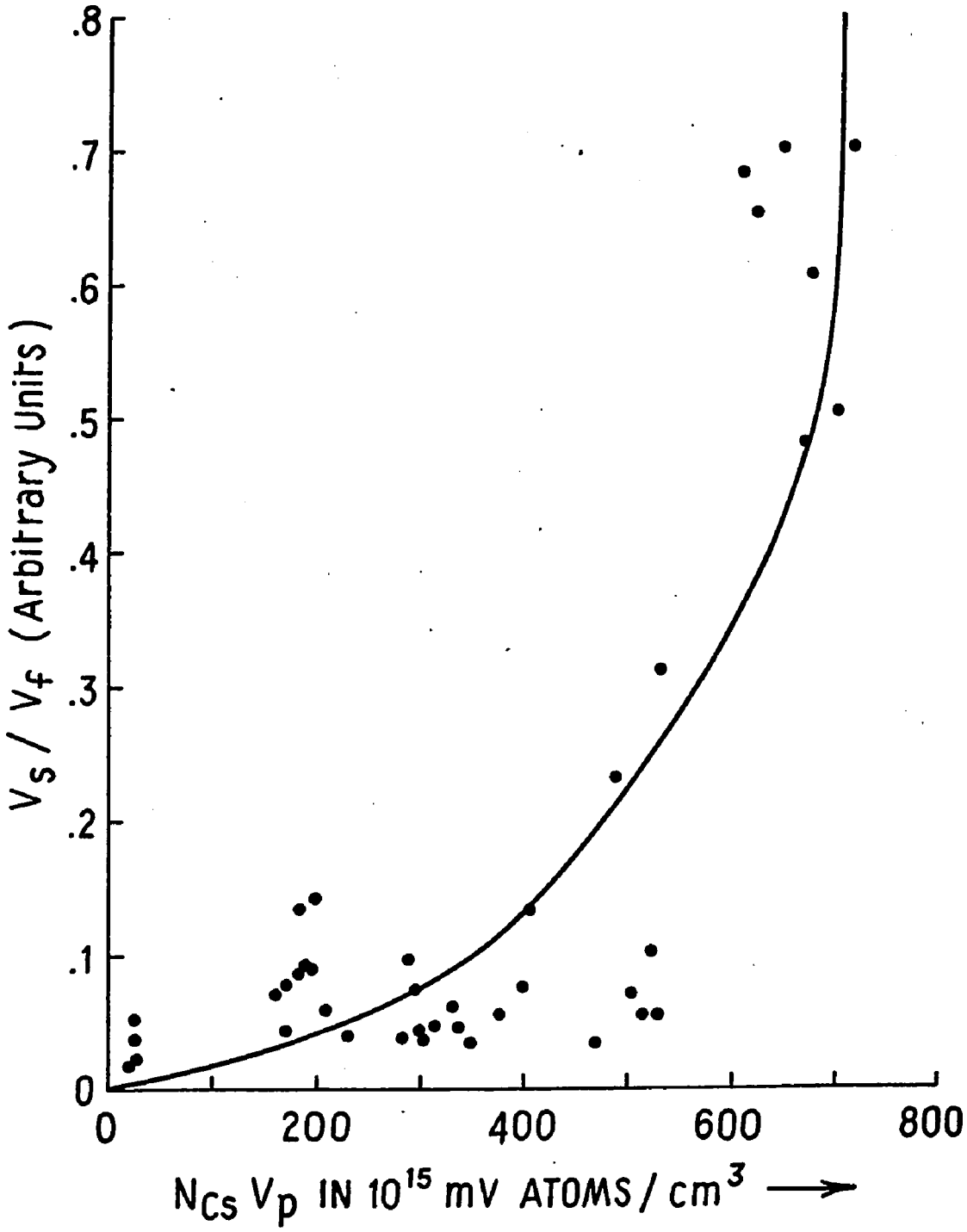


Figure 29. Simultaneous Measurement of Head-On Detector Signal and Sideways Detector Signal as a Function of Cesium Density and Fundamental Power.

we have measured the sideways detector signal which followed a square law similar to those displayed in Figure 20.b of Chapter 4.

In view of equations 5.15 and 5.16, as well as the experimental results of Figure 30 (a graph of ℓnV_s versus $N_{Cs}V_p$), the gain coefficient g for the four-photon parametric amplification in cesium vapor can be estimated. Equation 5.15 may be re-written in the form:

$$\ell nV_s = \ell n(\frac{P_{so}}{4\tau_s}) + (\frac{64\pi^3}{c}\sqrt{\omega_s\omega_I}\ \tau_p\frac{z}{a}\ K\ Re\sqrt{\chi_s\chi_I^*})N_{Cs}V_p \qquad (5.17)$$

where ω is in unit of cm^{-1}, τ_s and τ_p are conversion factors from powers to pulse heights in signal and fundamental respectively; z is the effective length of the nonlinear medium and a is the beam area near the focal position of the focused beam but using a plane wave approximation, i.e., $a = \pi w_o^2$.

From the slope of Figure 30, the value for the gain coefficient g is estimated to be

$$g = 0.77\ cm^{-1} \qquad (5.18)$$

and the value for the relevant nonlinear coefficients is

$$Re\sqrt{\chi_s\chi_I^*} = 3 \times 10^{-29}\ esu/atom \qquad (5.19)$$

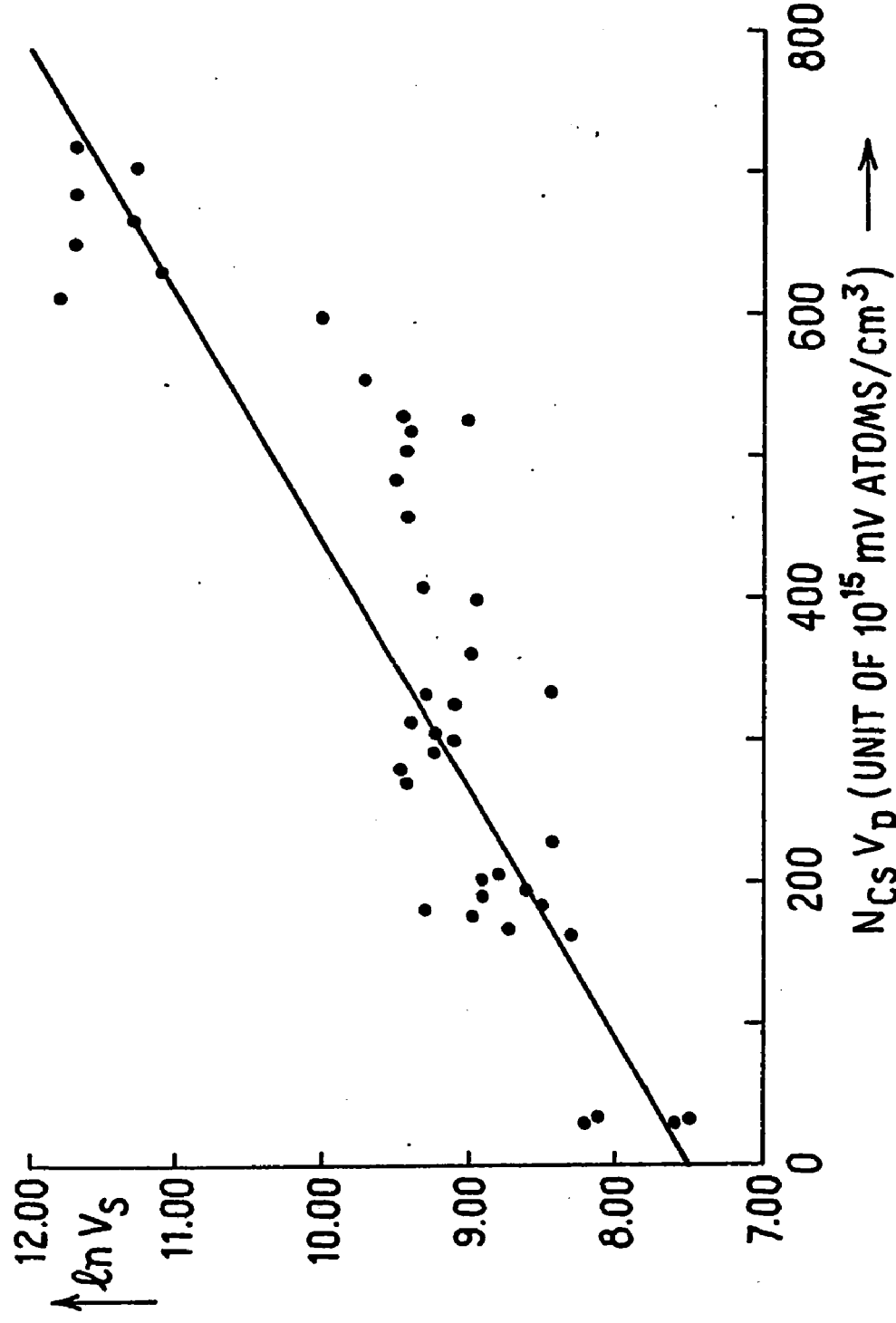


Figure 30. $\ell n\ V_s$ vs Cesium Density and Pump Intensity

The above results are evaluated assuming a plane wave fundamental beam propagating in a lossless medium under phase-matched conditions.

5.3 Theoretical Value of Gain Coefficient

Our primary objective in making a theoretical calculation for the gain coefficient of four-photon parametric amplification in cesium vapor is to compare values of the exponential gain from experiment and theory rather than to determine a nonlinear coefficient. We would like to first make an estimate of the coefficients, $\mathrm{Re}(\chi_s \chi_I^*)^{\frac{1}{2}}$.

Unlike the case of the resonant third-harmonic generation in cesium, these nonlinear coefficients have two resonant factors. For example, a coefficient related to the signal wave at 28754 cm^{-1} (corresponding to $10P_{3/2} \rightarrow 6S_{1/2}$ transition) can be expressed in the form using equation A1.1,

$$\chi_s(-\omega_s;\omega_p,\omega_p,-\omega_I) =$$

$$\frac{e^4}{3(-hc)^3}[\langle g|z|10P_{3/2}\rangle\langle 10P_{3/2}|z|9D_{3/2}\rangle]$$

$$\{\sum_n{}' \frac{\langle 9D_{3/2}|z|n^2P\rangle\langle n^2P|z|g\rangle}{\omega_{n^2P} - \omega_p}\}$$

$$\{\frac{1}{\Omega_{9D_{3/2}} - 2\omega_p}\}\{\frac{1}{\Omega_{10P_{3/2}} - \omega_s}\} \qquad (5.20)$$

and similarly for the idler wave at 75 cm^{-1} (corresponding to $9D_{3/2} \rightarrow 10P_{3/2}$ transition), the complex conjugate of the nonlinear coefficient $\chi_I(-\omega_I;\omega_p,\omega_p,-\omega_s)$ is

$$\chi_I^*(-\omega_I;\omega_p,\omega_p,-\omega_s) =$$

$$\frac{e^4}{3(-hc)^3}[\langle g|z|10P_{3/2}\rangle\langle 10P_{3/2}|z|9D_{3/2}\rangle]$$

$$\{\sum_n{}' \frac{\langle 9D_{3/2}|z|n^2P\rangle\langle n^2P|z|g\rangle}{\omega_{n^2P} - \omega_p}\}$$

$$\{\frac{1}{\Omega^*_{9D_{3/2}} - 2\omega_p}\}\{\frac{1}{\Omega_{10P_{3/2}} - \omega_s}\} \qquad (5.21)$$

where we have noted that the resonant contribution of $9D_{3/2} \leftarrow 6S_{1/2}$ in the two coefficients are complex conjugate of each other, such that the square root of the product of these two coefficients takes the form of

$$\hat{\chi} \equiv \sqrt{\chi_s \chi_I^*} = \hat{\chi}_o\{\frac{(\Gamma_{9D_{3/2}}/2)^2}{(\omega_{9D_{3/2}} - 2\omega_p)^2 + (\Gamma_{9D_{3/2}}/2)^2}\}^{\frac{1}{2}}$$

$$\times \{\frac{(\Gamma_{10P_{3/2}}/2)}{(\omega_{10P_{3/2}} - \omega_s) - i\Gamma_{10P_{3/2}}/2}\} \qquad (5.22)$$

with

$$\hat{\chi}_o = -\frac{e^4}{3(hc)^3}[\langle g|z|10P_{3/2}\rangle\langle 10P_{3/2}|z|9D_{3/2}\rangle]$$

$$\{\sum_n{}' \frac{\langle 9D_{3/2}|z|n^2P\rangle\langle n^2P|z|g\rangle}{\omega_{n^2P} - \omega_p}\}\left(\frac{2}{\Gamma_{9D_{3/2}}}\right)\left(\frac{2}{\Gamma_{10P_{3/2}}}\right) \tag{5.23}$$

which can be estimated by means of oscillator strength or f values given by Stone[22](we have not included contributions from the continuum). The result is -3×10^{-17} esu/atom.

To evaluate $\hat{\chi}$ or g, one can perform the same averaging process described in Chapter 4 with some modifications in the procedure (for example, in this case, the integral of Doppler average cannot be written in terms of the Plasma Dispersion Function). Rigorous evaluation of Doppler and multimode averaging for $\hat{\chi}$ can be carried out, but it will be tedious and a less rigorous procedure seems appropriate. In the following, we only make an estimate of these coefficients using the results of Doppler averaging for a single mode laser beam and ignore the effect of longitudinal multimode structure of the laser beam.

Figure 31 displays such an averaging process in terms of the calculated number $\hat{\chi}_o$. We have assumed that the $9D_{3/2}$ level is exactly on resonance and indicated only the $10P_{3/2}$ broadening. It is noted that there are two peaks

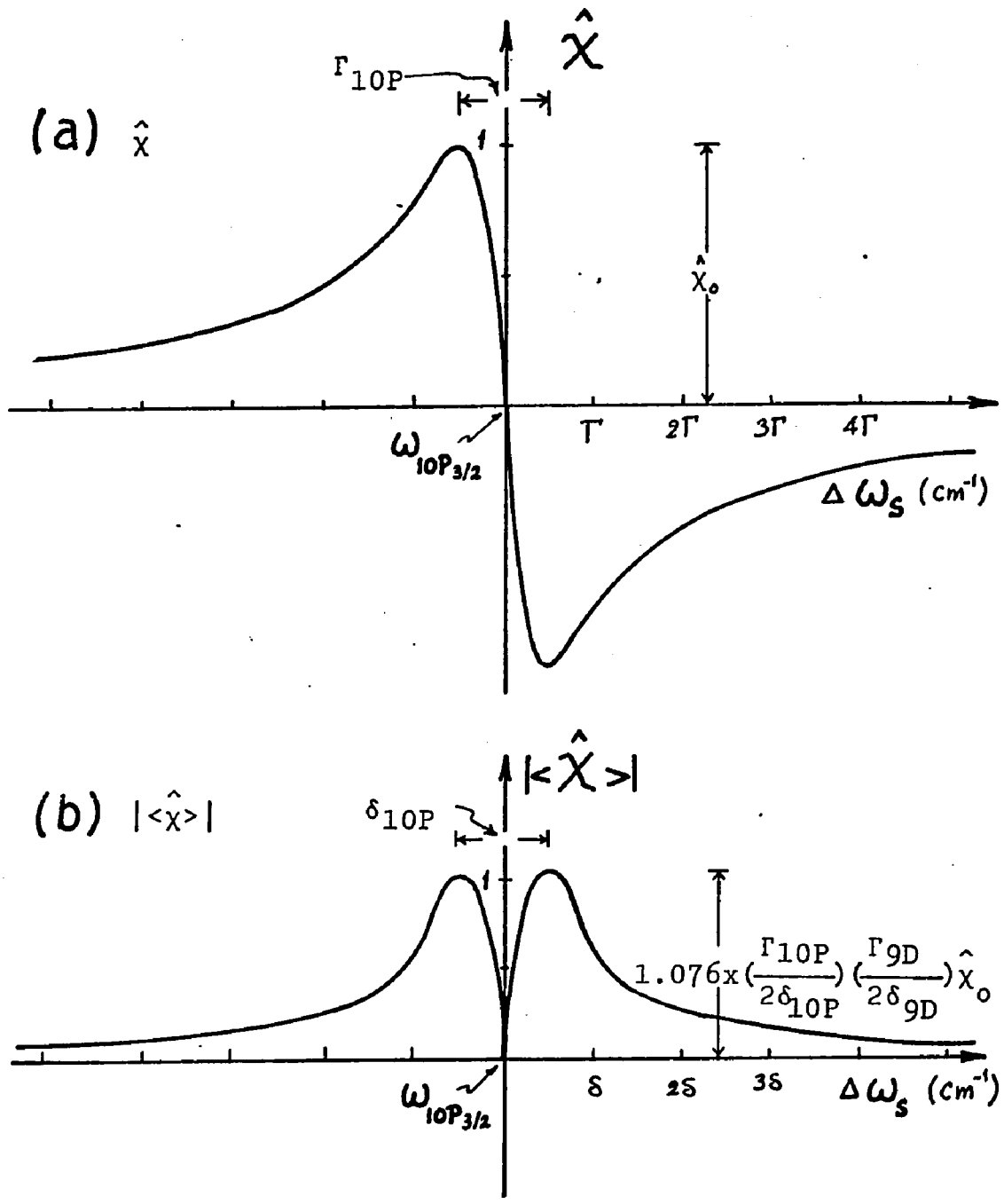


Figure 31. Simulated Doppler Averaging of $\hat{\chi}$ for Four-Photon Parametric Amplification

with same height due to a Doppler broadening of the $10P_{3/2}$ level. For each resonant contribution of equation 5.22, one would expect its magnitude to be reduced by a factor of natural width divided by its Doppler width of a respective level, i.e.,

$$\hat{\chi} = \hat{\chi}_o\left(1.77 \frac{\Gamma_{9D_{3/2}}}{2\delta_{9D_{3/2}}}\right)\left(1.076 \frac{\Gamma_{10P_{3/2}}}{2\delta_{10P_{3/2}}}\right) \qquad (5.24)$$

Using values of respective natural widths and effective Doppler widths, namely,

$$\Gamma_{9D_{3/2}} = 1.9 \times 10^{-5} \text{ cm}^{-1}$$

$$\Gamma_{10P_{3/2}} = 2.6 \times 10^{-5} \text{ cm}^{-1}$$

$$\delta_{9D_{3/2}} = 0.025 \text{ cm}^{-1}$$

$$\delta_{10P_{3/2}} = 0.025 \text{ cm}^{-1}$$

the absolute value of $\hat{\chi}$ for four-photon parametric amplification in cesium vapor, when the signal and twice the pump frequencies lie close to two different transition frequencies of the cesium atom (in this case, $10P_{3/2} \rightarrow 6S_{1/2}$ and $9D_{3/2} \leftarrow 6S_{1/2}$) is estimated to be

$$|\langle\hat{\chi}\rangle| = |\langle \text{Re}\sqrt{\chi_s \chi_I^*}\rangle| = 1.0 \times 10^{-23} \text{ esu/atom} \qquad (5.25)$$

with Doppler averaging over the velocity distribution of cesium atom and an assumption of single mode laser beam.

According to this estimate, the predicted gain of the four-photon parametric amplification in cesium at signal frequency of 28754 cm^{-1} is about 10^5 times greater than the measured gain.

The above estimate has involved several simplifying assumptions. Our laser pump source is multimode and focused into the center of the medium while the theory of deriving the gain coefficient is for plane wave and a single mode pump wave. We further approximate that our pump source is non-depleted and all wave vectors are under phase-matched conditions in a lossless medium. But, in fact, if the signal wave is subject to a linear absorption of the non-linear medium and if it is not phase-matched, the gain coefficient would be modified in the form,

$$g \rightarrow g = \tfrac{1}{2}\{(-\alpha_s + i\Delta k) \pm \sqrt{(-\alpha_s + i\Delta k)^2 + G_s G_I^*}\} \qquad (5.26)$$

where α_s is the linear absorption coefficient in cm^{-1}. Both α_s and Δk will reduce the gain.

In conclusion, we have observed another interesting resonant process in cesium vapor in addition to the resonant third-harmonic generation and the two-photon absorption. It was shown that such effect is a stimulated analog of the two-photon fluorescence with an exponential gain, or can be referred to as doubly resonant, four-photon parametric

amplification. In a preliminary experimental study, high conversion of the fundamental light source was indicated by a powerful output of about 20 mW blue light at 3500 Å. And the gain coefficient was measured to be 0.77 cm^{-1} with no saturation evident. A theoretical calculation using a set of simplifying assumptions also gave an upper limit estimate of the gain for this particular signal wave which is much larger than observed. This implies that such a resonant effect with huge coefficients may offer a useful engineering application (for example, it can be used as a potential uv source). To further this preliminary study, one would carry out more experiments to resolve the possible spectrum and pin down the dependence of signal wave on relevant parameters. Moreover, the multimode nature of our laser beam should be taken into account in the averaging process.

CHAPTER 6

SUMMARY AND CONCLUSIONS

Using a flexible experimental apparatus consisting of a tunable, pulsed, Q-switched ruby laser, three distinct resonant processes have been studied in atomic cesium vapor. They are resonant third-harmonic generation, two-photon absorption, and four-photon parametric amplification. Among them, the resonant third-harmonic generation was studied in greatest detail. The two-photon absorption was demonstrated to correlate to the other two processes.

About one μW of third-harmonic radiation near 2312 Å has been generated in cesium with 0.1 Torr vapor pressure and 1 Torr neon buffer gas in the cell. In order to interpret the experimental result, the propagation of third-harmonic radiation in inhomogeneous media for the plane wave case as well as focused beam case was analyzed and compared with their counterparts in homogeneous media. Expressions of third-harmonic signal were derived using the solution of this propagation problem relevant to our experimental configuration. These expressions yielded a relation between the third-harmonic signal and the nonlinear coefficient. A set of experiments on cesium were performed to demonstrate the predicted signal dependence on cesium vapor density (corresponding to the total number of coherence lengths Ω) the focal position ξ_0 (or z_0) with respect to the density distribution, and the half width

d (or ℓ) of the density distribution (with $d = \frac{1}{2}b\ell$, where b is the confocal parameter of the Gaussian beam). It was predicted that the optimum harmonic signal S^{THG} could be obtained by focusing the beam ($b = 2.5\ d$) into the dense medium ($z_o = 0$) at a fixed cesium side arm temperature ($\Omega = 0.8$). A good fit over a wide range of beam optics and the signal was obtained with a single mode theory modified qualitatively to take the multimode nature of the beam into account.

The third-harmonic generation in cesium vapor has been successfully demonstrated to exhibit a resonance effect. The peak resonance frequency corresponds closely to half the energy difference between the ground state of cesium and its $9D_{3/2}$ state (14414.45 cm^{-1}). In addition, a simultaneous measurement of two-photon fluorescent signal using the sideways detector and third-harmonic signal using the head-on detector gives a strong correlation of the two resonant processes. An experimental value of the peak resonant third-harmonic nonlinear coefficient for cesium has been determined to be 1.0×10^{-30} esu/atom with an uncertainty factor of 5. A theoretical value of the coefficient in terms of a quantum mechanically calculated number given by Orr (see Appendix 1) has also been obtained to be 2.8×10^{-30} esu/atom by performing an averaging process over the longitudinal multimode structure of our laser spectrum and taking into account the velocity distribution of cesium atoms. This value is about 10^9 times greater than that of helium given by Sitz and

Yaris[19], and is in satisfactory agreement with the experimental value within experimental uncertainty.

Another resonant process closely related to the two-photon absorption was observed in cesium vapor. With cesium vapor pressure near 0.5 Torr, about 20 mW of uv light at 3500 Å originating from the test cell was detected and could be seen with the naked eye and a fluorescent screen. This interesting effect was demonstrated to be the stimulated analog of twc-photon absorption and could be referred to as doubly resonant, four-photon parametric amplification. In a preliminary experimental study, a gain coefficient was measured to be 0.77 cm^{-1}. This may be compared with the result of a simplified calculation which gave an upper limit to the coefficient much larger than that observed. We conclude that this four-photon parametric amplification is capable of explaining the observation. However, further and more detailed work is necessary.

As an overall view of this work, different aspects can be accentuated in our conclusions. First, from our result, atomic cesium vapor as a simple system does provide a good correlation of theory and experiment in gaining a fundamental understanding of nonlinear optical processes. Secondly, values of the peak resonant third-harmonic nonlinear coefficient and the gain coefficient of four-photon parametric amplication for cesium were found to be large so that one can speculate on their practical engineering importance. For example, as a nonlinear material, cesium vapor is cheap,

undamageable, and with unlimited dimension as compared to other solid state materials for optical frequency conversion. Thirdly, it is seen from our results that such conversion efficiency can be improved by optimizing the propagation problem and resonant enhancement of the nonlinear coefficients. If the process could be index-matched as has been demonstrated by Harris and coworkers[23] using a suitable mixture of alkali-metal vapor and inert buffer gas (for example, a mixture of rubidium and xenon atoms in the ratio of 1 : 412), then higher conversion efficiency could be achieved. Finally, it would also be interesting to extend these studies to other nonlinear materials and wavelength regions.

APPENDIX 1

QUANTUM MECHANICAL CALCULATION OF χ_{Cs}

The summary of the calculation is kindly furnished by B. Orr. In the following, only the information and results which are relevant to our determination of $\langle\chi\rangle$ will be presented in order to supplement Chapter 4.

The general time-dependent perturbation expression for the third-order polarization ($\omega_\sigma = \omega_1+\omega_2+\omega_3$) is[14]:

$$
\begin{aligned}
\mathbf{P}^{\omega_\sigma} = K(-\omega_\sigma;\, \omega_1,\, \omega_2,\, \omega_3)(-\hbar)^{-3} I_{1,\,2,\,3}
\times \Bigg[\sum_{lmn}{}' \Bigg\{ & \frac{\langle P\rangle_{gl}\langle \bar{\Pi}'^{\omega_3}\rangle_{lm}\langle \bar{\Pi}'^{\omega_2}\rangle_{mn}\langle H'^{\omega_1}\rangle_{ng}}{(\Omega_{lg}-\omega_\sigma)(\Omega_{mg}-\omega_1-\omega_2)(\Omega_{ng}-\omega_1)} \\
& + \frac{\langle H'^{\omega_3}\rangle_{gl}\langle \bar{P}\rangle_{lm}\langle \bar{\Pi}'^{\omega_2}\rangle_{mn}\langle H'^{\omega_1}\rangle_{ng}}{(\Omega^*_{lg}+\omega_3)(\Omega_{mg}-\omega_1-\omega_2)(\Omega_{ng}-\omega_1)} \\
& + \frac{\langle H'^{\omega_1}\rangle_{gl}\langle \bar{\Pi}'^{\omega_2}\rangle_{lm}\langle \bar{P}\rangle_{mn}\langle H'^{\omega_3}\rangle_{ng}}{(\Omega^*_{lg}+\omega_1)(\Omega^*_{mg}+\omega_1+\omega_2)(\Omega_{ng}-\omega_3)} \\
& + \frac{\langle H'^{\omega_1}\rangle_{gl}\langle \bar{\Pi}'^{\omega_2}\rangle_{lm}\langle \bar{\Pi}'^{\omega_3}\rangle_{mn}\langle P\rangle_{ng}}{(\Omega^*_{lg}+\omega_1)(\Omega^*_{mg}+\omega_1+\omega_2)(\Omega^*_{ng}+\omega_\sigma)} \Bigg\} \\
- \sum_{mn}{}' \Bigg\{ & \frac{\langle P\rangle_{gm}\langle H'^{\omega_3}\rangle_{mg}\langle H'^{\omega_2}\rangle_{gn}\langle H'^{\omega_1}\rangle_{ng}}{(\Omega_{mg}-\omega_\sigma)(\Omega_{mg}-\omega_3)(\Omega_{ng}-\omega_1)} \\
& + \frac{\langle P\rangle_{gm}\langle H'^{\omega_3}\rangle_{mg}\langle H'^{\omega_2}\rangle_{gn}\langle H'^{\omega_1}\rangle_{ng}}{(\Omega_{mg}-\omega_3)(\Omega^*_{ng}+\omega_2)(\Omega_{ng}-\omega_1)} \\
& + \frac{\langle H'^{\omega_3}\rangle_{gm}\langle P\rangle_{mg}\langle H'^{\omega_1}\rangle_{gn}\langle H'^{\omega_2}\rangle_{ng}}{(\Omega^*_{mg}+\omega_\sigma)(\Omega^*_{mg}+\omega_3)(\Omega^*_{ng}+\omega_1)} \\
& + \frac{\langle H'^{\omega_2}\rangle_{gm}\langle P\rangle_{mg}\langle H'^{\omega_1}\rangle_{gn}\langle H'^{\omega_2}\rangle_{ng}}{(\Omega^*_{mg}+\omega_3)(\Omega_{ng}-\omega_2)(\Omega^*_{ng}+\omega_1)} \Bigg\} \Bigg]. \qquad \text{(A1.1)}
\end{aligned}
$$

where the notation $< A >_{ij}$ denotes the matrix element $< i|A|j >$ and a barred operator is defined by

$$\bar{A} = A - < A >_{gg} \tag{A1.2}$$

The $\sum'$ indicates a summation over all states except the ground state. If we factor the electric fields out of the matrix elements, the remaining expression inside the bracket [...] yields a microscopic nonlinear susceptibility $\chi_{ijkl}(-\omega_\sigma;\omega_1,\omega_2,\omega_3)$ for any third-order process.

The nonlinear third-harmonic coefficient for a system, which has a resonance frequency ω_{mg} close to 2ω, where ω is the fundamental frequency of the applied optical field, is then written in a form of

$$\chi_{zzzz}(-3\omega;\omega,\omega,\omega) = I_{1,2,3}\ \{\frac{e^4}{(-hc)^3}\}$$

$$\{\sum_n{}' \frac{<m|z|n><n|z|g>}{\omega_{ng} - \omega}\}\ \{\sum_l{}'\ <g|z|l><l|z|m>$$

$$(\frac{1}{\omega_{lg}-3\omega} + \frac{1}{\omega_{lg}+\omega})\}\ \{\frac{1}{(\omega_{lg}-2\omega) - i\Gamma_m/2}\}$$

(A1.3)

where the unit for frequencies is cm^{-1}.

In the case of cesium atom for ω_{mg} near the $9D_{3/2} \leftarrow 6S_{1/2}$, the nonlinear coefficient is

$$\chi_{Cs} = \frac{e^4}{(-hc)^3} I_{1,2,3} \left\{\frac{1}{\Omega_{9D_{3/2}} - 2\omega}\right\}$$

$$\left\{\sum_n{}' A_n\left(\tfrac{1}{2};\tfrac{3}{2}\right) + \tfrac{1}{5}\sum_n{}' A_n\left(\tfrac{3}{2};\tfrac{3}{2}\right) + \tfrac{6}{5}\int_0^\infty d\varepsilon' A(\varepsilon')\right\}$$

$$\left\{\sum_\ell{}' B_\ell\left(\tfrac{1}{2};\tfrac{3}{2}\right) + \tfrac{1}{5}\sum_\ell{}' B_\ell\left(\tfrac{3}{2};\tfrac{3}{2}\right) + \tfrac{6}{5}\int_0^\infty d\varepsilon' B(\varepsilon')\right\}$$

where

$$A_n\left(j_1;\tfrac{3}{2}\right) = \{\omega(n^2P_{j_1} - 6S_{\frac{1}{2}}) - \omega\}^{-1} \sigma(6s;np_{j_1}) \sigma(np_{j_1};9d\tfrac{3}{2})$$

$$B_\ell\left(j_1;\tfrac{3}{2}\right) = [\{\omega(\ell^2P_{j_1} - 6S_{\frac{1}{2}}) - 3\omega\}^{-1} + \{\omega(\ell^2P_{j_1} - 6S_{\frac{1}{2}}) + \omega\}^{-1}]$$

$$\sigma(6s\tfrac{1}{2};\ell pj_1) \sigma(\ell pj_1;9d\tfrac{3}{2})$$

$$A(\varepsilon') = \{I(6^2S_{\frac{1}{2}}) + \varepsilon' - \omega\}^{-1} \sigma(6s;\varepsilon' p) \sigma(\varepsilon' p;9d)$$

$$B(\varepsilon') = \{[I(6^2S_{\frac{1}{2}}) + \varepsilon' - 3\omega]^{-1} + [I(6^2S_{\frac{1}{2}}) + \varepsilon' + \omega]^{-1}\}$$

$$\sigma(6s;\varepsilon' p) \sigma(\varepsilon' p;9d)$$

with $I(6^2S_{\frac{1}{2}})$ as the ionization potential of the $6^2S_{\frac{1}{2}}$ state, ε' as the energy of the ionized electron in a continuum p state.

The reduced matrix element is defined by

$$\sigma(n'\ \ell-1\ j';n\ell j) = (4\ell^2-1)^{-\frac{1}{2}} \int_0^\infty rdrR_{n'\ \ell-1\ j'}\ R_{n\ell j}$$

where $R_{n\ell j}/r$ is the radial part of a one electron state $|n\ell j>$. Values of σ have been computed from the following sources:

for n = 6, ..., 12

(1) The Bates-Damgaard Coulomb approximation[24].

(2) Oscillator strengths computed by Stone[22].

for the continuum

(3) Extrapolated quantum defects and the tables of Peach[25].

for the integrals

(4) Graphical evaluation.

It was noted that σ is dependent on j and j' because of the strong spin-orbit coupling in cesium. Source (2), however, has such corrections for spin-orbit coupling. The sums over A_n converge nicely and the continuum is about 10%. But the sums over B_ℓ cancel so severely that the continuum contribution is dominant. The numerical result of the calculation in terms of the resonant factor is

$$\chi_{Cs} = (8.8 \times 10^{-27})\ I_{1,2,3}\left\{\frac{\Gamma_{9D}/2}{\Omega_{9D_{3/2}} - \omega_1 - \omega_2}\right\} \qquad (A1.4)$$

or if we set the constant number to be χ_o, equation 4.13 is obtained to be

$$\chi_{Cs} = \chi_o I_{1,2,3} \frac{\Gamma_{9D}/2}{\Omega_{9D}-\omega_1-\omega_2} \qquad \text{(A1.5)}$$

with Γ_{9D} equal to 1.9×10^{-5} cm^{-1}.

REFERENCES

1. P. A. Franken, A. E. Hill, C. W. Peters, and G. Weinreich, Phys. Rev. Letters 7, 118 (1961).

2. Some recommended reviews of nonlinear optics
   P. A. Franken and J. F. Ward, Rev. Mod. Phys. 35, 23 (1963).
   J. A. Giordmaine, Scientific American 4, 38 (1964).
   N. Bloembergen, Nonlinear Optics (Benjamin Book Co. Inc., 1965).
   R. W. Minck, R. W. Terhune, and C. C. Wang, Proc. IEEE 54, 1357 (1966).
   J. A. Giordmaine, Physics Todays 22, 39 (1969).

3. N. Bloembergen, Am. J. Phys. 35, 989 (1967).

4. I. D. Abella, Phys. Rev. Letters 9, 453 (1962).

5. P. D. Maker and R. W. Terhune, Phys. Rev. 137, A801 (1965).

6. K. S. Gibson, Phys. Rev. 8, 38 (1916).

7. J. R. Izatt, R. C. Mitchell, and H. A. Daw, J. Appl. Phys. 37, 1558 (1966).

8. D. A. Kleinman, Phys. Rev. 128, 1761 (1962).

9. D. A. Kleinman, A. Ashkin, and G. D. Boyd, Phys. Rev. 145, 338 (1966).

10. G. D. Boyd, A. Ashkin, J. M. Dziedzic, and D. A. Kleinman, Phys. Rev. 137, A1305 (1965).

11. J. A. Armstrong, N. Bloembergen, J. Ducuing, D. S. Pershan, Phys. Rev. 127, 1918 (1962).

12. J. F. Ward and G. H. C. New, Phys. Rev. 185, 57 (1969).

13. J. E. Bjorkholm, Phys. Rev. 142, 126 (1966).

14. B. J. Orr and J. F. Ward, Molecular Physics 20, 513 (1971).

15. B. J. Orr (private communication).

16. G. D. Boyd and J. P. Gordon, Bell Sys. Tech. J. 40, 489 (1961).

17. R. S. Finn and J. F. Ward, Phys. Rev. Letters 26, 285 (1971).

18. Conversion Tables for Thermocouples, (Leeds & Northrup Company, Philadelphia, Pa.) pp 18 and 19; R. E. Honig and D. A. Kramer, RCA Review 30, 285 (1969).

19. P. Sitz and R. Yaris, J. Chem. Phys. 49, 3546 (1968).

20. B. D. Fried and S. D. Conte, The Plasma Dispersion Function (Academic Press Ltd. 1961).

21. A. Yaris, Quantum Electronics (John Wiley & Sons, Inc., 1967).

22. P. M. Stone, Phys. Rev. 127, 1151 (1962).

23. S. E. Harris and R. B. Miles, Appl. Phys. Letters 19, 385 (1971); J. F. Young, G. C. Bjorklund, A. H. Kung, R. B. Miles, and S. E. Harris, Phys. Rev. Letters 27, 1551 (1971); S. E. Harris et al., Generation of uv Radiation in Phase-Matched Metal Vapors (invited), VII International Quantum Electronics Conference, Montreal, Canada, May 8-11, 1972.

24. D. R. Bates and A. Damgaard, Phil. Trans. Roy. Soc. London A242, 101 (1949).

25. G. Peach, Mem. Roy. Astr. Soc. 71, 13 (1967).